Modeling and Simulation of Arsenic Activation and Diffusion in Silicon

Pavel Fastenko

A dissertation submitted in partial fulfillment of
the requirements for the degree of

Doctor of Philosophy

University of Washington

2002

Program Authorized to Offer Degree: Electrical Engineering

University of Washington

Graduate School

This is to certify that I have examined this copy of a doctoral dissertation by

Pavel Fastenko

and have found that it is complete and satisfactory in all respects,

and that any and all revisions required by the final

examining committee have been made.

Chair of Supervisory Committee:

____

Scott T. Dunham

Reading Committee:

____

Lucien N. Brush

____

Robert B. Darling

____

Scott T. Dunham

Date: ______________________

University of Washington

Abstract

Modeling and Simulation of Arsenic Activation and Diffusion in Silicon

by Pavel Fastenko

Chair of Supervisory Committee:

Professor Scott T. Dunham
Department of Electrical Engineering

One of the critical problems that exist in Very Large Scale Integrated (VLSI) circuit process modeling is prediction and simulation of the behavior of dopants in silicon during fabrication. This work is focused on understanding and modeling of the physical processes which control diffusion and deactivation of arsenic, the primary n-type dopant in silicon.

Arsenic deactivation is a complicated process due to fast kinetics and strong interstitial ejection which accompanies deactivation. We have used ab-initio calculations in order to gain insight into the fundamental processes involved in arsenic activation/deactivation. It has been proposed that several second nearest neighbor As atoms (two or more) may kick-out an adjacent Si atom forming an electrically inactive arsenic-vacancy cluster and a self-interstitial. A physical model based on this mechanism was derived and used successfully to match a variety of electrical data as well as interstitial supersaturation data measured during deactivation. This model was applied to understanding and predicting ultra shallow junction formation. Several effects such as rapid As diffusion at high concentrations and the existence of grown-in vacancies after amorphous/crystalline regrowth must be included to account for the discrepancies between what seems to be the mobile fraction of the profile and the electrically active fraction.

An integral part of this work involves the simulation of self-interstitial cluster formation. Total energy calculations based on empirical Molecular Dynamics (MD) simulations were

performed in order to study the energetics of interstitial aggregates as a function of size and configuration. These results provide insight into ion implant annealing processes. A Kinetic Precipitation Model (KPM) was used to analyze the evolution of {311} defects. We discuss small interstitial clusters and their role in the initial stages of annealing after ion implantation and during As deactivation.

TABLE OF CONTENTS

LIST OF FIGURES

LIST OF TABLES

ACKNOWLEDGMENTS

The most of all, I would like to acknowledge my advisor Scott T. Dunham for his his guidance and support. His deep and detailed knowledge in the field combined with the very broad perspective made learning and research interesting and rewarding.

I would like to thank the committee members Professors Robert B. Darling, Lucien N. Brush, and Karl Bohringer for their time, helpful comments and interesting questions. I am also thankful to Dr. Norman J. McCormick for serving as a Graduate School Representative.

I would like to acknowledge the Semiconductor Research Corporation whose financial support made this project possible.

I also would like to thank collaborators and a lot of people whose contribution greatly enhanced this project. Special thanks to Peter Griffin, Reza Kaznavi, Ant Ural, Amitabh Jain, Sandro Solmi, Dan Downey, Kevin Jones for sharing their experimental data with me. I would like to thank Maria Caturla for the help with molecular dynamics simulator MDCASK. I was really happy to meet Cheruvu Murthy and have him as a mentor during my internship at IBM in 1999.

I would like to thank all colleagues and friends from the lab. Many thanks to Srini Chakravarthi for helpful discussions and a lot of good time spent together. I would also like to thank Brendon Murphy for spending a lot of time teaching me how to use DOPDEES/PMM. Thanks to Alp Gencer, Marius Bunea, Mitra Navi, Chen-Luen Shih, and Heidi Meyer and Milan Diebel. I would also like to express thanks to Ryangzu Kim for sharing his experimental results and beneficial exchange of ideas.

Finally, I would like to thank my wife Anna for love, understanding and encouragement during my long quest for knowledge and the degree.

Chapter 1

INTRODUCTION

1.1 Industrial and scientific necessities

Achievements made in the computer industry over the past 25 years have been driven by the ability to increase both the speed and the density of silicon transistors. Decreasing device size is the main driving force for these advancements in semiconductor technology. Most directly, down-scaling of the dimensions results in larger numbers of devices per wafer. Thus, for similar processing costs, manufacturers can produce larger numbers of dies from the wafer or improve the functionality of the chips by placing more transistors in the same die area. The downward scaling of the device size also leads to the higher performance, as smaller channel lengths result in faster transistors.

Device scaling requires that all dimensions of the device be scaled. However, simple scaling of the source/drain region depths without altering doping of the junctions can result in an unacceptable increase in device resistance. To maintain low resistance as the device is scaled down, the carrier concentrations must simultaneously be increased. Therefore, as the metal oxide semiconductor (MOS) transistor is scaled down, extremely shallow, very highly doped junctions must be formed. This poses substantial challenges both in controlling diffusion at such small scales and achieving high activation at or above equilibrium solubility.

Today's devices are so small that characterization of their material parameters is very difficult and expensive. Thus, simulation is often the only effective and affordable tool for exploring vertical and lateral profiles of a modern transistor. Additionally, the cost of fabrication for test lots (needed for new technology development) increases with each new technology generation making usual trial and error method extremely expensive. These factors make simulation of front-end processing a critical component of today's integrated-circuit

(IC) technology development. The goal is to replace physical optimization experiments with virtual ones, only placing the new process in manufacturing after the virtual device meets all specifications. However, computer-aided technology is cost-effective only if it is accurate and truly predictive. Current process simulators often contain empirical models which lack the physical basis needed for accurate simulation of new generation processes. Thus, continued advancement of physically-based models are required for efficient, accurate, and predictive process simulation tools. This work is focused on arsenic, the primary n-type dopant used in modern semiconductor devices. Modeling its behavior, especially diffusion and electrical properties, is essential to include in the process simulator software.

Ion implantation is a powerful tool used to introduce dopants in silicon. However, this process also creates a large amount of crystal damage in the form of interstitials and vacancies, as well as non-substitutional dopants. Thus a high temperature anneal is necessary to activate the dopant atoms and repair the damaged Si crystal to maintain good electrical properties. Since dopant diffusion in silicon is mediated by point-defects, and ion implantation significantly increases the number of point-defects, post implant annealing is characterized by anomalous dopant diffusion. During high temperature annealing, dopant atoms interact with point-defects, forming mobile dopant-defect pairs, immobile complexes, and (at high concentrations) precipitates. At the same time, point-defects may also cluster, recombine, diffuse, etc. Therefore, the final dopant distribution is a complex combination of a wide range of atomic-scale interactions.

Dopants such as arsenic may form electrically inactive clusters with point defects, deactivating below the solid solubility. Laser melting is proposed as an alternative to rapid thermal processing for the formation of highly doped layers in silicon. Using laser melting, dopants can be activated to metastable levels above solid solubility. However, it has been reported that during subsequent annealing, arsenic rapidly deactivates generating large concentrations of point-defects. Exploration and modeling of underlying physical mechanisms may lead to understanding of the fundamental limitations of this new technique.

Post ion implantation annealing and arsenic deactivation lead to the formation of self-interstitial clusters ({311} defects and dislocation loops). As annealing continues, these

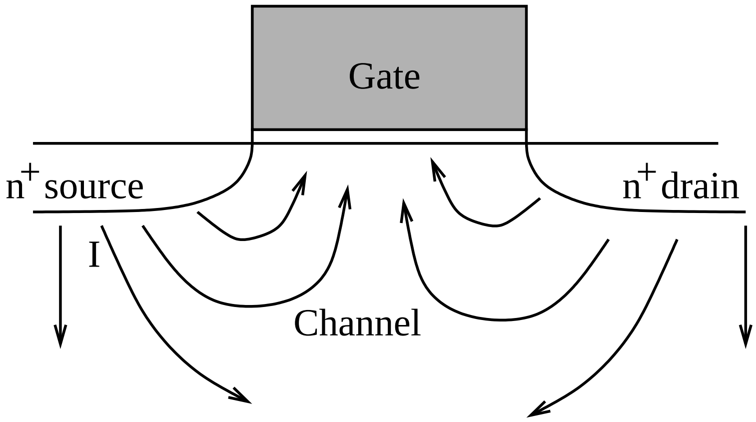

Figure 1.1: Illustration of how enhanced diffusion impacts MOS transistor characteristics. Interstitials are injected from heavily arsenic-doped source/drain during deactivation. They can diffuse and enhanced boron diffusion under the gate. This leads to dopant redistribution in the channel and has been reported to increase the reverse short channel effect [89].

defects grow and eventually dissolve. Dissolution of these defects releases interstitials, which enhance dopant diffusion. Thus, modeling of {311} defect behavior is important for accurate prediction of dopant diffusion and electrical activation.

Fig. 1.1 is a schematic describing how interstitials created during arsenic deactivation in a source/drain of a MOS transistor lead to dopant redistribution in the channel region. Enhanced diffusion of boron in the channel region towards the gate causes an increased threshold voltage and a severe reverse short channel effect.

In order to predict final electrical characteristics of the device (transistor), it is necessary to model all these complex interactions simultaneously. The simulation of such a system involves a large number of parameters describing each mechanism. Specifically designed experiments have been used to identify key mechanisms and to calibrate parameters. Atomistic techniques like *ab-initio* and molecular dynamics (MD) generate insight into the physics of individual particle reactions in the silicon lattice. Continuum simulations are used to implement the models, coupled with other processes steps, and finally, compared with experiments to validate models.

1.2 Dissertation objectives

In this dissertation, we present a self-consistent set of models applicable to a broad range of data. We study and model arsenic diffusion and electrical activation in silicon, based on the understanding of underlying physical phenomena, including:

- Electrical deactivation of arsenic layers fully activated by a laser anneal. This deactivation is accompanied by a strong interstitial injection.

- Modeling of ultra-shallow junction formation by ion implantation and rapid thermal processing.

- Interstitial cluster and extended defect formation after ion implantation and during arsenic deactivation, including the role of small self-interstitial clusters.

To model these phenomena, continuum modeling are utilized, with parameters obtained by:

- inverse modeling of experimental data,

- atomistic calculations from other studies and published in the literature,

- our own molecular dynamics calculations.

1.3 Dissertation Overview

We begin Chapter 2 by discussing both arsenic diffusion in silicon and its interaction with point defects, demonstrating the method used for dopant diffusion modeling. A short overview of ion implantation damage and post implant anneal modeling is presented next. In Chapter 3, we implement total energy calculations based on empirical MD simulations to study energetics of interstitial aggregates as a function of their size and configuration. Minimum energy configurations were used to obtain a functional dependence of defect energy on size. This was applied via the Kinetic Precipitation Model [32] to analyze the evolution of {311} defects. The results are compared to {311} dissolution experimental data. These initial results show the role of assumptions made regarding small interstitial clusters. Chapter 4 is dedicated to the analysis of small self-interstitial clusters. We also present a computationally efficient two-moment model to simulate small cluster behavior. This was used for the analysis of ion implant damage cascade annealing. In Chapter 5, we discuss an up-to-date literature review of arsenic electrical activation/deactivation, including a description of experiments and overview of modeling efforts. We begin Chapter 6 by introducing the mechanism of arsenic deactivation from the theoretical standpoint. Next, we present our deactivation modeling approach, and compare simulation results to experimental results. In Chapter 7, we present modeling of ultra-low energy high concentration implants activated by spike annealing. We also review arsenic's high concentration diffusion effect and discuss point defect distribution after amorphous/crystalline region regrowth. In Chapter 8, we summarize the results of this work and discuss directions for future research.

Chapter 2

DOPANT DIFFUSION IN SILICON

Dopant diffusion in silicon takes place through pairing reactions with point-defects and diffusion of dopant-defect pairs. In this chapter, we review diffusion mechanisms. We briefly describe damage produced by ion implantation and the phenomenon of Transient Enhanced Diffusion (TED).

2.1 Arsenic diffusion in silicon

2.1.1 Diffusion mechanisms

Diffusion of substitutional dopants like arsenic can be mediated on the atomic scale by either point-defects, namely interstitials or vacancies, or by a direct exchange mechanism. The relative contribution of each of these mechanisms for a given dopant is a fundamental property. The manner in which perturbations in point-defect concentration affect dopant diffusion depends on the fraction of its diffusion mediated by that point defect. It is well established that thermal oxidation injects self-interstitials, whereas nitridation results in vacancy injection into the bulk [39]. It was shown [103] that As diffuses via dual vacancy-interstitial mechanism, with the possibility of a concerted exchange component. In our work we assume that the exchange component is zero, and arsenic diffuses by dual interstitial and vacancy mechanisms, an assumption which is consistent with experimental and theoretical results published to date.

In the vacancy mechanism, a dopant atom moves into an adjacent vacant site (see Fig. 2.1 for illustration). Diffusion does not occur by a simple vacancy/dopant exchange, since then the dopant and vacancy will continue to occupy alternating lattice sites and no long-range migration of dopant will take place. In silicon (diamond) structure, the vacancy must diffuse away to at least a third-nearest neighbor site and return via a new direction to complete

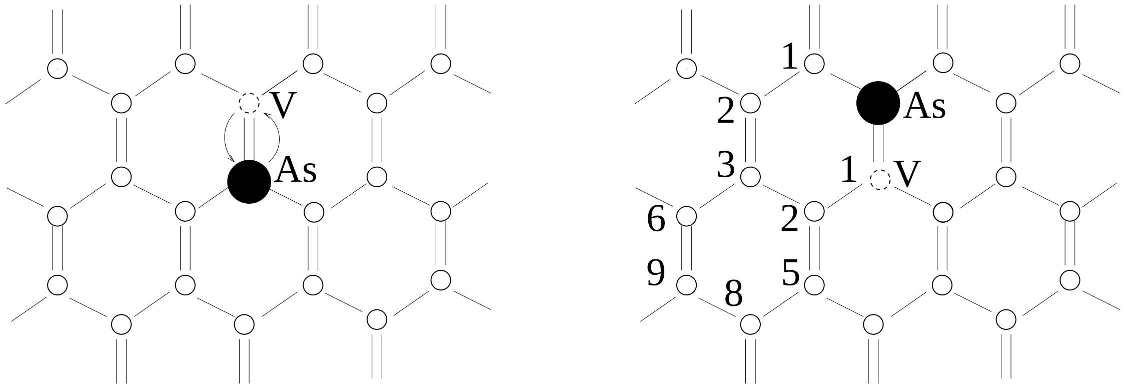

Figure 2.1: The illustration of the vacancy diffusion mechanism for arsenic in the silicon lattice. In the initial diffusion step the arsenic and the vacancy (V) are positioned in the adjacent sites. The simple exchange of As and vacancy does not lead to any diffusion since no long range migration takes place. To complete one diffusion step the vacancy must diffuse away to at least a third nearest neighbor site and return via a different direction. The numbers on the plot indicate the type of neighbor (the fourth and seventh nearest neighbors are out of the plane).

one diffusion step. The rate limiting step for As diffusion via vacancy mechanism is thus the barrier for vacancy to migrate from the 2nd to the 3rd nearest neighbor site.

On the macroscopic scale, this mechanism can be described by the reaction:

$$\mathrm{As}_s + \mathrm{V} \Leftrightarrow \mathrm{AsV}, \tag{2.1}$$

where As_s stands for substitutional arsenic, and AsV for arsenic vacancy pair.

In the interstitial mechanism, a self-interstitial (Si) may displace a dopant atom into an interstitial site creating a dopant interstitial (As_i). Now, the dopant interstitial can diffuse through the lattice, since the migration barrier is much lower than for substitutional dopant, until it moves into another substitutional site by kicking a silicon atom out into an interstitial position. This process is schematically shown in Fig. 2.3. The process can be described by the following reaction:

$$\mathrm{As}_s + \mathrm{I} \Leftrightarrow \mathrm{As}_i. \tag{2.2}$$

The interstitialcy mechanism is very similar. The mobile complex is formed by an impurity and a silicon atom sharing the same lattice site (denote by AsI). The reaction for

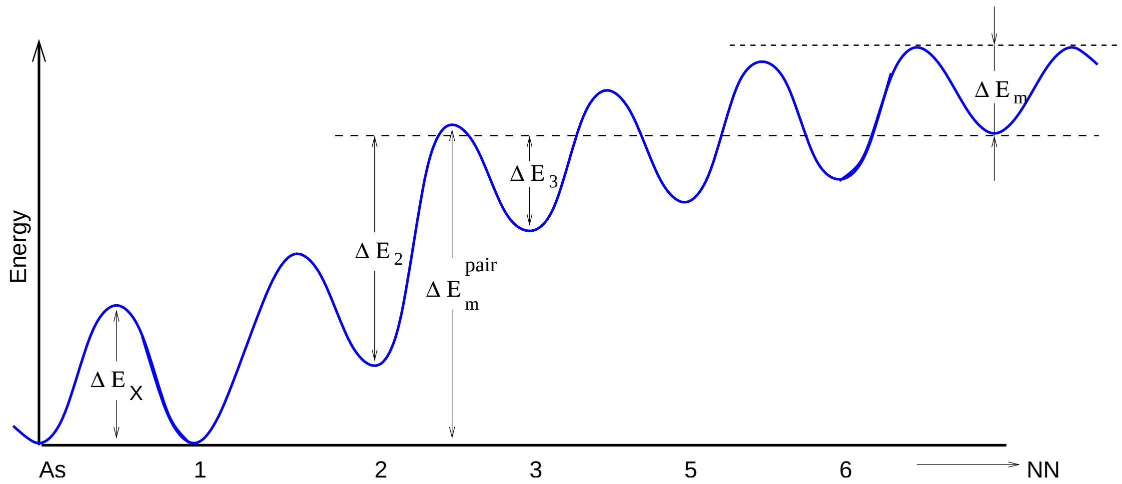

Figure 2.2: Schematic illustration of As-V interaction potential. The dopant atom (As) is placed in the origin of horizontal axis, the numbers on the horizontal axis represent the neighbor lattice sites with respect to the arsenic atom. ΔE_X represent the energy barrier for As-V exchange (i.e., energy barrier for As to hop into the adjacent empty site). ΔE_2 and ΔE_3 are the binding energies at the second and the third nearest sites respectively. ΔE_m denotes the migration barrier for a vacancy far away from the arsenic atom. The rate limiting step for As diffusion via vacancy mechanism is the barrier for vacancy to overcome for 2nd to 3rd nearest neighbor site migration ($\Delta E_m^{\mathrm{pair}}$).

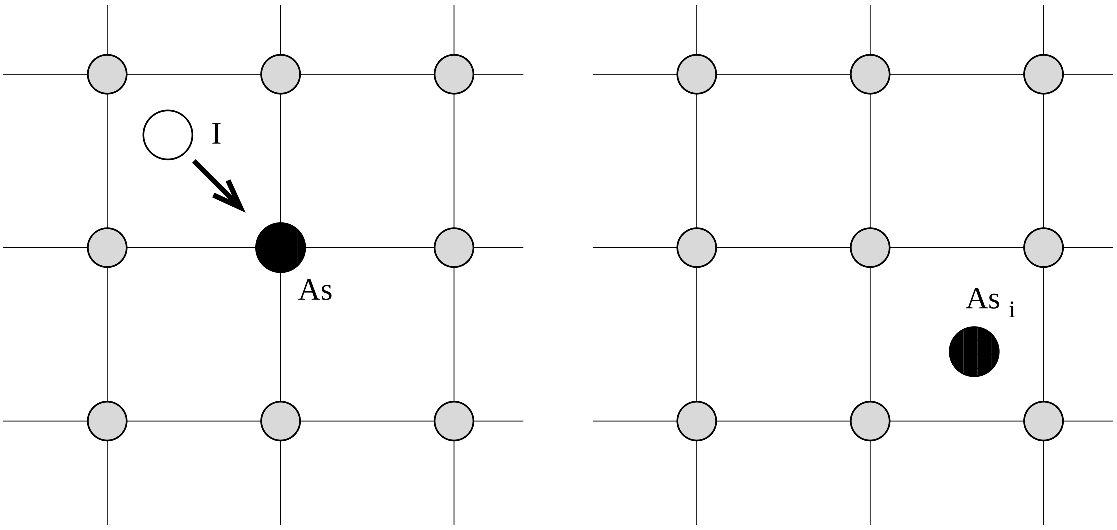

Figure 2.3: Schematic illustration of interstitial assisted diffusion mechanism. In the left figure, a dark circle represents a substitutional arsenic atom, being kicked-out by a silicon self-interstitial (open circle). In the right figure, arsenic is now located in an interstitial site and can diffuse through the lattice with much lower diffusion barrier.

this mechanism is given by:

$$\mathrm{As} + \mathrm{I} \Leftrightarrow \mathrm{AsI}. \tag{2.3}$$

Experiments targeted at the determination of the dominant diffusion mechanism for dopants in silicon (fractional interstitialcy component, f_I) have been carried out via oxidation/nitridation assisted point defect injection in the presence of a dopant marker layer [39, 47, 103]. It has been found that arsenic in silicon diffuses by a dual vacancy ($\sim 60\%$) and interstitial ($\sim 40\%$) mechanism, while boron diffusion is primarily dominated by interstitials ($> 97\%$). The purely interstitial diffusion mechanism of boron allows the use of a boron profile as an indicator (marker) for the presence of the interstitial supersaturation in a sample. Antimony diffusion is dominated by the vacancy mechanism making it a clear choice for the vacancy "marker layer."

Since it is hard to distinguish between interstitialcy diffusion mechanism and interstitial mechanism in experiment, and also since both mechanisms lead to the same macroscopic diffusion equations, in this work we consider interstitial-assisted diffusion (which includes both effects) and use the symbol AsI for both arsenic interstitial pair as well as for arsenic interstitialcy (if not noted otherwise).

2.1.2 Coupled Diffusion

As we discussed in the previous section, dopants in silicon diffuse via interactions with point defects: interstitials and vacancies. The standard model for dopant diffusion in silicon [74, 75, 34] assumes that dopants form pairs with defects and diffusion takes place only through dopant-defect pair migration. In this section, we derive coupled diffusion equation for arsenic in silicon. Our derivation is analogous to the one presented by Gencer [44] for boron in silicon, but includes both vacancy and interstitial diffusion mechanisms, since both are important for As.

For our analysis, we assume that only one dopant (As) is present in a system. It is straight forward to extend the analysis to multiple dopants. We shall use (X) to denote a point defect (interstitial (I) or vacancy (V)) and use it for the reactions which look the same for both I and V to avoid retyping the reaction twice. We can write down the pairing reactions with point defects for all possible charge states as:

$$\mathrm{As}^i + \mathrm{I}^j \quad \Leftrightarrow \quad (\mathrm{AsI})^{i+j}, \tag{2.4}$$

$$\mathrm{As}^i + \mathrm{V}^j \quad \Leftrightarrow \quad (\mathrm{AsV})^{i+j}. \tag{2.5}$$

The indexes i and j represent the charge states of the defect or pair. The recombination and generation of Frenkel pairs (interstitial plus vacancy) can be described as:

$$\mathrm{I}^i + \mathrm{V}^j \Leftrightarrow (-i-j)e^-. \tag{2.6}$$

In addition, the pairs can interact directly with the opposite type defect to produce a reaction which is equivalent to a pair dissociation followed by defect recombination.

$$(\mathrm{AsI})^i + \mathrm{V}^j \quad \Leftrightarrow \quad \mathrm{As}^+ + (1-i-j)e^-, \tag{2.7}$$

$$(\mathrm{AsV})^i + \mathrm{I}^j \quad \Leftrightarrow \quad \mathrm{As}^+ + (1-i-j)e^-. \tag{2.8}$$

The dissociative mechanism of AsI formation from As, the reverse of reaction of Eq. 2.8 is also called the Frank-Turnbull mechanism.

In this work, we consider charge exchange reactions for each of the charged species. Because the electronic reactions are much faster than the atomic diffusion processes, we assume that ionization reactions are near local equilibrium.

Fig. 2.4 shows the reported location of interstitial charge states in the silicon band gap at 1000°C [45]. For the charged point defects, the following equations are valid in a dilute concentration approximation [39]:

$$\begin{aligned}
\frac{C_{\mathrm{X}^-}}{C_{\mathrm{X}^0}} &= \frac{\theta_{\mathrm{X}^-}}{\theta_{\mathrm{X}^0}}\exp\left(-\frac{E_{\mathrm{X}^-}-E_f}{kT}\right) = \frac{\theta_{\mathrm{X}^-}}{\theta_{\mathrm{X}^0}}\exp\left(\frac{E_f^i-E_{\mathrm{X}^-}}{kT}\right)\left(\frac{n}{n_i}\right), && (2.9)\\
\frac{C_{\mathrm{X}^+}}{C_{\mathrm{X}^0}} &= \frac{\theta_{\mathrm{X}^+}}{\theta_{\mathrm{X}^0}}\exp\left(-\frac{E_f-E_{\mathrm{X}^+}}{kT}\right) = \frac{\theta_{\mathrm{X}^+}}{\theta_{\mathrm{X}^0}}\exp\left(\frac{E_{\mathrm{X}^+}-E_f^i}{kT}\right)\left(\frac{p}{n_i}\right), && (2.10)\\
\frac{C_{\mathrm{X}^=}}{C_{\mathrm{X}^0}} &= \frac{\theta_{\mathrm{X}^=}}{\theta_{\mathrm{X}^0}}\exp\left(-\frac{E_{\mathrm{X}^=}+E_{\mathrm{X}^-}-2E_f}{kT}\right) = \\
&= \frac{\theta_{\mathrm{X}^=}}{\theta_{\mathrm{X}^0}}\exp\left(\frac{2E_f^i-E_{\mathrm{X}^-}-E_{\mathrm{X}^=}}{kT}\right)\left(\frac{n}{n_i}\right)^2, && (2.11)\\
\frac{C_{\mathrm{X}^{++}}}{C_{\mathrm{X}^0}} &= \frac{\theta_{\mathrm{X}^+}}{\theta_{\mathrm{X}^0}}\exp\left(-\frac{2E_f-E_{\mathrm{X}^+}-E_{\mathrm{X}^{++}}}{kT}\right) = \\
&= \frac{\theta_{\mathrm{X}^{++}}}{\theta_{\mathrm{X}^0}}\exp\left(\frac{E_{\mathrm{X}^{++}}+E_{\mathrm{X}^+}-2E_f^i}{kT}\right)\left(\frac{p}{n_i}\right)^2, && (2.12)
\end{aligned}$$

where, E_f is the Fermi level, E_f^i is the intrinsic Fermi level and E_{X^i} is the energy level of the charged state in the silicon band gap. The terms n, p and n_i are the local and intrinsic carrier concentrations. The term θ_{X^i} is the number of degrees of internal freedom of the defect on a lattice site (e.g. spin or orientation degeneracy).

We can rewrite these reactions in a general form as:

$$C_{\mathrm{X}^i} = K_{\mathrm{X}^i} C_{\mathrm{X}^0}(n_i/n)^i, \qquad (2.13)$$

where the K_{X^i} represent the equilibrium coefficients.

Similarly the concentrations of arsenic-interstitial (AsI) and arsenic-vacancy (AsV) pairs are given by:

$$\begin{aligned}
C_{(\mathrm{AsI})^i} &= K_{(\mathrm{AsI})^i} C_{(\mathrm{AsI})^0}(n_i/n)^i, && (2.14)\\
C_{(\mathrm{AsV})^i} &= K_{(\mathrm{AsV})^i} C_{(\mathrm{AsV})^+}(n_i/n)^{i-1} && (2.15)
\end{aligned}$$

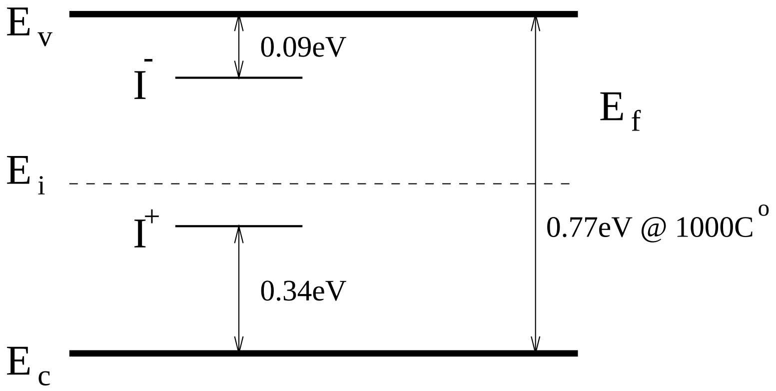

Figure 2.4: Interstitial energy levels in silicon at 1000°C after Giles [45].

where the K_{X} represents equilibrium coefficient.

It is necessary to determine the Fermi level in order to consider the behavior of charged species. Even though it is possible to solve Poisson's equation in conjunction with continuity equations, the common assumptions for Fermi level calculation are the local charge neutrality and mass action law for charges [39], so the Fermi level can be determined by simply considering the net concentration of ionized dopants. Charged pairs and defects are affected by the electric field, but do not significantly influence it themselves since their concentration is usually much smaller than that of ionized dopants.

Since both defects and pairs can exist in multiple charge states (e.g., $\mathrm{V}^{=}$, I^{+}), C_{I}, C_{V}, C_{AsI} and C_{AsV} have to be summed over all charge states to obtain total concentrations. Thus, for example, the total point-defect concentrations can be determined by:

$$C_{\mathrm{I}} = \sum_i C_{\mathrm{I}^i} = \sum_i \left[K_{\mathrm{I}^i} \left(\frac{n_i}{n} \right)^i C_{\mathrm{I}^0} \right] = \chi_{\mathrm{I}} C_{\mathrm{I}^0}, \tag{2.16}$$

$$C_{\mathrm{V}} = \sum_i C_{\mathrm{V}^i} = \sum_i \left[K_{\mathrm{V}^i} \left(\frac{n_i}{n} \right)^i C_{\mathrm{V}^0} \right] = \chi_{\mathrm{V}} C_{\mathrm{V}^0}, \tag{2.17}$$

where C_{I^0} and C_{V^0} are the concentration of neutral interstitials and vacancies respectively.

Similarly, at equilibrium we can introduce another parameter, π_{X},

$$\begin{aligned} C_{\mathrm{AsX}} &= \sum_i C_{(\mathrm{AsX})^i} = \pi_{\mathrm{X}} C_{\mathrm{As}} C_{\mathrm{X}^0}, && (2.18)\\ C_{(\mathrm{AsX})^+} &= K_{\mathrm{As}^+/\mathrm{X}^0} C_{\mathrm{As}} C_{\mathrm{X}^0} = K_{\mathrm{As}^+/\mathrm{X}^0} \frac{C_{\mathrm{AsX}}}{\pi_{\mathrm{X}}}, && (2.19) \end{aligned}$$

where $K_{\mathrm{As}^+/\mathrm{X}^0}$ is the equilibrium constant for the pairing of a neutral point defect with an As substitutional atom. In this work we consider a neutral point-defect (V^0 and I^0) as a reference for point-defects since charged defect concentration (as well as the total point defect concentration) depend on the Fermi level position. The majority of arsenic in the system is present as substitutional donors and therefore is positively charged (As^+). Since the electronic exchange can occur before or after dopant-defect pairing and the equilibrium concentrations are independent of reaction path, we can write,

$$K_{\mathrm{As}^+/\mathrm{X}^0} K_{(\mathrm{AsX})^{i+1}} = K_{\mathrm{X}^i} K_{\mathrm{As}^+/\mathrm{X}^i}. \tag{2.20}$$

Thus,

$$\begin{aligned} \pi_{\mathrm{V}} &= K_{\mathrm{As}^+/\mathrm{V}^0} \left[K_{(\mathrm{AsV})^0} \left(\frac{n}{n_i}\right) + 1 + K_{(\mathrm{AsV})^-} \left(\frac{n}{n_i}\right)^2 + K_{(\mathrm{AsV})^{++}} \left(\frac{p}{n_i}\right) \right] && (2.21)\\ &= K_{\mathrm{As}^+/\mathrm{V}^0} + K_{\mathrm{As}^+/\mathrm{V}^-} K_{\mathrm{V}^-} \left(\frac{n}{n_i}\right) + K_{\mathrm{As}^+/\mathrm{V}^=} K_{\mathrm{V}^=} \left(\frac{n}{n_i}\right)^2 + K_{\mathrm{As}^+/\mathrm{V}^+} K_{\mathrm{V}^+} \left(\frac{p}{n_i}\right) \end{aligned}$$

$$\begin{aligned} \pi_{\mathrm{I}} &= K_{\mathrm{As}^+/\mathrm{I}^0} \left[K_{(\mathrm{AsI})^0} \left(\frac{n}{n_i}\right) + 1 + K_{(\mathrm{AsI})^{++}} \left(\frac{p}{n_i}\right) \right] && (2.22)\\ &= K_{\mathrm{As}^+/\mathrm{I}^0} + K_{\mathrm{As}^+/\mathrm{I}^-} K_{\mathrm{I}^-} \left(\frac{n}{n_i}\right) + K_{\mathrm{As}^+/\mathrm{I}^+} K_{\mathrm{I}^+} \left(\frac{p}{n_i}\right) \end{aligned}$$

Note that we have left off interaction with doubly charged interstitials in these equations since their effect is expected to be insignificant. Also arsenic is a donor, so $K_{\mathrm{As}^+/\mathrm{V}^+}$ and $K_{\mathrm{As}^+/\mathrm{I}^+}$ are expected to be small due to Colombic repulsion.

Now we can write continuity equations for dopant (As), interstitials, vacancies, and dopant-defect pairs, resulting in the following system (also commonly referred to as a "five stream model" based on the number of equations) [44]:

$$\frac{\partial C_{\mathrm{As}}}{\partial t} = -R_{\mathrm{As+I}} - R_{\mathrm{As+V}} + R_{\mathrm{AsI+V}} + R_{\mathrm{AsV+I}} + 2R_{\mathrm{AsI+AsV}}$$

$$\begin{aligned}
\frac{\partial C_{\mathrm{AsI}}}{\partial t} &= -\vec{\nabla}\vec{J}_{\mathrm{AsI}} + R_{\mathrm{As+I}} - R_{\mathrm{AsI+V}} - R_{\mathrm{AsI+AsV}} \\
\frac{\partial C_{\mathrm{AsV}}}{\partial t} &= -\vec{\nabla}\vec{J}_{\mathrm{AsV}} + R_{\mathrm{As+V}} - R_{\mathrm{AsV+I}} - R_{\mathrm{AsI+AsV}} \qquad (2.23) \\
\frac{\partial C_{\mathrm{I}}}{\partial t} &= -\vec{\nabla}\vec{J}_{\mathrm{I}} - R_{\mathrm{As+I}} - R_{\mathrm{I+V}} \\
\frac{\partial C_{\mathrm{V}}}{\partial t} &= -\vec{\nabla}\vec{J}_{\mathrm{V}} - R_{\mathrm{As+I}} - R_{\mathrm{I+V}}
\end{aligned}$$

J_{X} represents the flux of species X and $R_{\mathrm{X+Y}}$ represents the net rate per unit volume of the reaction of species X and Y (e.g., $R_{\mathrm{As+I}}$ represents the net forward rate of the kick-out reaction given by Eq. 2.2). The four flux terms are written for point defects and dopant-defects pairs which are considered mobile, the first equation for dopant does not have a flux term, since the substitutional dopant is considered immobile. The flux and the reaction terms also include sums over all charge states. Each additional dopant adds three additional equations (dopant and dopant-defect pairs) with corresponding reaction terms added to the point defect equations.

Note that due to the charge of the ions, the continuity equation will not only have a diffusion component ($\vec{J}^{\mathrm{diff}}$), but also a drift component ($\vec{J}^{\mathrm{drift}}$). The drift terms arise because the charged species also move because of the electric field, associated with the gradient in the electron concentration. The total flux of point defects and pairs will be equal to the sum of fluxes of each charge state i:

$$\vec{J}_{(\mathrm{AsX})^i} = \vec{J}^{\mathrm{diff}}_{(\mathrm{AsX})^i} + \vec{J}^{\mathrm{drift}}_{(\mathrm{AsX})^i} \qquad (2.24)$$

Since arsenic is a donor (As^+), we will write the equations in terms of the single positively charged donor-defect pair, $(\mathrm{AsX})^+$ which is the pair of a donor plus neutral defect. Thus the diffusion term is:

$$\begin{aligned}
\vec{J}^{\mathrm{diff}}_{(\mathrm{AsX})^i} &= -D_{(\mathrm{AsX})^i}\vec{\nabla}C_{(\mathrm{AsX})^i} \qquad (2.25) \\
&= -D_{(\mathrm{AsX})^i}\vec{\nabla}\left[K_{(\mathrm{AsX})^i}C_{(\mathrm{AsX})^+}(n_i/n)^{i-1}\right] \\
&= -D_{(\mathrm{AsX})^i}K_{(\mathrm{AsX})^i}\vec{\nabla}\left[C_{(\mathrm{AsX})^+}(n_i/n)^{i-1}\right] \\
&= -D_{(\mathrm{AsX})^i}K_{(\mathrm{AsX})^i}\left[(n_i/n)^{i-1}\vec{\nabla}C_{(\mathrm{AsX})^+} + (i-1)C_{(\mathrm{AsX})^+}(n_i/n)^{i-2}\vec{\nabla}(n_i/n)\right].
\end{aligned}$$

The drift term becomes:

$$\begin{aligned} \vec{J}^{\text{drift}}_{(\text{AsX})^i} &= \mu_{(\text{AsX})^i} iq\vec{\mathcal{E}} C_{(\text{AsX})^i} \\ &= D_{(\text{AsX})^i}(q/kT) i\vec{\mathcal{E}} C_{(\text{AsX})^i}, \end{aligned} \tag{2.26}$$

where $\mu = D/kT$ is the mobility according to the Einstein relationship and $\vec{\mathcal{E}}$ is the electric field vector. The electric field can be calculated from the gradient of the electrostatic potential, which in turn can be found from the local carrier concentration, given by a Boltzman distribution:

$$n = n_i \exp\left(\frac{q\phi}{kT}\right), \tag{2.27}$$

where ϕ is the electric potential, so

$$\begin{aligned} \vec{\mathcal{E}} &= -\vec{\nabla}\phi \\ &= -\vec{\nabla}\left[kT/q \ln(n/n_i)\right]. \end{aligned} \tag{2.28}$$

Thus drift term is given by:

$$\begin{aligned} \vec{J}^{\text{drift}}_{(\text{AsX})^i} &= iD_{(\text{AsX})^i} C_{(\text{AsX})^i} \vec{\nabla} \ln(n_i/n) \\ &= iD_{(\text{AsX})^i} \left[K_{(\text{AsX})^i} C_{(\text{AsX})^+} (n_i/n)^{i-1}\right] (n/n_i) \vec{\nabla}(n_i/n) \\ &= iD_{(\text{AsX})^i} K_{(\text{AsX})^i} C_{(\text{AsX})^+} (n_i/n)^{i-2} \vec{\nabla}(n_i/n). \end{aligned} \tag{2.29}$$

Adding the diffusion and drift terms we get:

$$\begin{aligned} \vec{J}_{(\text{AsX})^i} &= -D_{(\text{AsX})^i} K_{(\text{AsX})^i} (n_i/n)^{i-1} \left[\vec{\nabla} C_{(\text{AsX})^+} - C_{(\text{AsX})^+} (n/n_i) \vec{\nabla}(n_i/n)\right] \qquad (2.30) \\ &= -D_{(\text{AsX})^i} K_{(\text{AsX})^i} (n_i/n)^{i-1} \left[\vec{\nabla} C_{(\text{AsX})^+} - C_{(\text{AsX})^+} \vec{\nabla} \ln(n_i/n)\right] \\ &= -D_{(\text{AsX})^i} K_{(\text{AsX})^i} K_{\text{As}^+/\text{X}^0} (n_i/n)^{i-1} \left[\vec{\nabla}\left(\frac{C_{\text{AsX}}}{\pi_{\text{X}}}\right) + \frac{C_{\text{AsX}}}{\pi_{\text{X}}} \vec{\nabla} \ln\left(\frac{n}{n_i}\right)\right]. \end{aligned}$$

We consider diffusion only via single-charged point defects, X^-, X^0 and X^+, giving $i = 0, +1, +2$ respectively. Summing over all the charge states, we get:

$$\vec{J}_{\text{AsX}} = \sum_{i=0}^{+2} \vec{J}_{(\text{AsX})^i}. \tag{2.31}$$

The macroscopic diffusivities are defined as

$$D^{\text{X}^i}_{\text{As}} = D_{(\text{AsX})^{(i-1)}} \frac{C^*_{(\text{AsX})^{(i-1)}}}{C_{\text{As}}}. \tag{2.32}$$

The separate components of diffusivities such as $D_{\mathrm{As}}^{\mathrm{V}^-}$ stand for diffusivity of arsenic via pairing with vacancies in a given charge state (V^- or $(\mathrm{AsV})^0$ in this case). Multiplying the numerator and denominator of Eq. 2.30 by $C_{\mathrm{As}}C_{\mathrm{V}^0}^*$ and taking into consideration Eqs. 2.15, 2.19, and 2.32, we can represent the fluxes in terms of macroscopic diffusivities:

$$\vec{J}_{\mathrm{AsV}} = -\frac{(D_{\mathrm{As}}^{\mathrm{V}^0} + D_{\mathrm{As}}^{\mathrm{V}^+}(p/n_i) + D_{\mathrm{As}}^{\mathrm{V}^-}(n/n_i))}{C_{\mathrm{V}^0}^*}\left[\vec{\nabla}\left(\frac{C_{\mathrm{AsV}}}{\pi_{\mathrm{V}}}\right) + \frac{C_{\mathrm{AsV}}}{\pi_{\mathrm{V}}}\vec{\nabla}\ln\left(\frac{n}{n_i}\right)\right], \tag{2.33}$$

$$\vec{J}_{\mathrm{AsI}} = -\frac{(D_{\mathrm{As}}^{\mathrm{I}^0} + D_{\mathrm{As}}^{\mathrm{I}^+}(p/n_i) + D_{\mathrm{As}}^{\mathrm{I}^-}(n/n_i))}{C_{\mathrm{I}^0}^*}\left[\vec{\nabla}\left(\frac{C_{\mathrm{AsI}}}{\pi_{\mathrm{I}}}\right) + \frac{C_{\mathrm{AsI}}}{\pi_{\mathrm{I}}}\vec{\nabla}\ln\left(\frac{n}{n_i}\right)\right]. \tag{2.34}$$

Note that for arsenic, a donor, we expect $D_{\mathrm{As}}^{\mathrm{I}^+}$ and $D_{\mathrm{As}}^{\mathrm{V}^+}$ to be negligible, consistent with experimental results [9, 39].

Now we would like to formally introduce the fractional interstitial component of dopant under an equilibrium conditions, which may be determined experimentally from oxidation/nitridation experiments, as:

$$f_I^0 = \frac{D_{\mathrm{As}}^{\mathrm{I}^0}}{D_{\mathrm{As}}^{\mathrm{I}^0} + D_{\mathrm{As}}^{\mathrm{V}^0}} = \frac{D_{\mathrm{As}}^{\mathrm{I}^0}}{D_{\mathrm{As}}^0}, \tag{2.35}$$

and

$$f_I^- = \frac{D_{\mathrm{As}}^{\mathrm{I}^-}}{D_{\mathrm{As}}^{\mathrm{I}^-} + D_{\mathrm{As}}^{\mathrm{V}^-}} = \frac{D_{\mathrm{As}}^{\mathrm{I}^-}}{D_{\mathrm{As}}^-}. \tag{2.36}$$

We also assume that the diffusivities of dopant-defect pairs are independent of the charge state. Now we would like to connect the ratio of $D_{\mathrm{As}}^-/D_{\mathrm{As}}^0$ which can be obtained from experiments to the parameters of our model. Since

$$\frac{C_{(\mathrm{AsV})^0}}{C_{(\mathrm{AsV})^+}} = \frac{D_{\mathrm{As}}^-}{D_{\mathrm{As}}^0}\left(\frac{n}{n_i}\right)\left(\frac{1-f_{\mathrm{I}}^-}{1-f_{\mathrm{I}}^0}\right), \tag{2.37}$$

then

$$\frac{D_{\mathrm{As}}^-}{D_{\mathrm{As}}^0} = \left(\frac{1-f_{\mathrm{I}}^0}{1-f_{\mathrm{I}}^-}\right)\frac{D_{\mathrm{As}}^{\mathrm{V}^-}}{D_{\mathrm{As}}^{\mathrm{V}^0}}\frac{K_{\mathrm{V}^-}K_{\mathrm{As}^+/\mathrm{V}^-}}{K_{\mathrm{V}^0}K_{\mathrm{As}^+/\mathrm{V}^0}}. \tag{2.38}$$

Hence, π_{V} and π_{I} can be determined.

The total flux of interstitials in each of the charge states can be written in terms of the gradient in the neutral concentration and the electron concentration:

$$\vec{J}_{\mathrm{I}^i} = -D_{\mathrm{I}^i}\left(\vec{\nabla}C_{\mathrm{I}^i} - \frac{iq\vec{\mathcal{E}}}{kT}C_{\mathrm{I}^i}\right) = -D_{\mathrm{I}^i}K_{\mathrm{I}^i}\left(\frac{n_i}{n}\right)^i\vec{\nabla}C_{\mathrm{I}^0}, \tag{2.39}$$

where D_{I^i} represents the diffusivity of interstitials of charge state i. Thus the total interstitial flux is:

$$\vec{J}_{\mathrm{I}} = \sum_i \vec{J}_{\mathrm{I}^i} = -D_{\mathrm{I}^0}\chi_{\mathrm{I}}\vec{\nabla}C_{\mathrm{I}^0} \tag{2.40}$$

where

$$\chi_{\mathrm{I}} = 1 + K_{\mathrm{I}^+}\left(\frac{p}{n_i}\right) + K_{\mathrm{I}^-}\left(\frac{n}{n_i}\right). \tag{2.41}$$

We assume that interstitial diffusivity is independent of the charge state, $D_{\mathrm{I}^i} = D_{\mathrm{I}^0}$, since no experimental evidence exists on this matter.

Similarly we can write for vacancies,

$$\begin{aligned} \vec{J}_{\mathrm{V}} &= -D_{\mathrm{V}^0}\chi_{\mathrm{V}}\vec{\nabla}C_{\mathrm{V}^0} \\ \chi_{\mathrm{V}} &= 1 + K_{\mathrm{V}^+}\left(\frac{p}{n_i}\right) + K_{\mathrm{V}^-}\left(\frac{n}{n_i}\right) \end{aligned} \tag{2.42}$$

The expressions for the net rate of pairing and recombination reactions are also summed over all the charge states. Noting the definitions of $\chi_{\mathrm{I}}, \chi_{\mathrm{V}}$ and $\pi_{\mathrm{I}}, \pi_{\mathrm{V}}$ from Eq. 2.16 and 2.18, we can write down the net reaction rates of the pairing and recombination reactions as:

$$\begin{aligned} R_{\mathrm{As+I}} &= k_{\mathrm{As/I}}[C_{\mathrm{As}}C_{\mathrm{I}} - \frac{\chi_{\mathrm{I}}}{\pi_{\mathrm{I}}}C_{\mathrm{AsI}}] \\ R_{\mathrm{As+V}} &= k_{\mathrm{As/V}}[C_{\mathrm{As}}C_{\mathrm{V}} - \frac{\chi_{\mathrm{I}}}{\pi_{\mathrm{I}}}C_{\mathrm{AsV}}] \\ R_{\mathrm{AsI+V}} &= k_{\mathrm{AsI/V}}(C_{\mathrm{AsI}}C_{\mathrm{V}} - C^*_{\mathrm{I}^0}C^*_{\mathrm{V}^0}\pi_I\chi_V C_{\mathrm{As}}) \\ R_{\mathrm{AsV+I}} &= k_{\mathrm{AsV/I}}(C_{\mathrm{AsV}}C_{\mathrm{I}} - C^*_{\mathrm{I}^0}C^*_{\mathrm{V}^0}\pi_V\chi_I C_{\mathrm{As}}) \\ R_{\mathrm{AsV+AsI}} &= k_{\mathrm{AsV/AsI}}(C_{\mathrm{AsV}}C_{\mathrm{AsI}} - C^*_{\mathrm{I}^0}C^*_{\mathrm{V}^0}\pi_I\pi_V C^2_{\mathrm{As}}) \end{aligned} \tag{2.43}$$

Note that the kinetic forward reaction rate $k_{\mathrm{X/Y}}$ for the reactants with diffusivities D_{X} and D_{Y} is assumed to be diffusion limited:

$$k_{\mathrm{X/Y}} = 4\pi\sigma\left(D_{\mathrm{X}} + D_{\mathrm{Y}}\right), \tag{2.44}$$

where σ is the effective reaction radius.

When other species such as clusters or extended defects are also present, additional continuity equations must be added and additional terms representing the formation/dissolution of these species must be included on the right hand sides of Eqs. 2.23.

Under intrinsic conditions near equilibrium with no spatial variation in point defect concentrations, the effective diffusivity of a dopant can be shown to be [39]:

$$\frac{D_{\mathrm{As}}}{D^*_{\mathrm{As}}} = f_{\mathrm{I}}^{\mathrm{intr}} \frac{C_{\mathrm{I}}}{C^*_{\mathrm{I}}} + (1 - f_{\mathrm{I}}^{\mathrm{intr}}) \frac{C_{\mathrm{V}}}{C^*_{\mathrm{V}}} \tag{2.45}$$

where, the * denotes equilibrium values.

From Eq. 2.45 it is clear that dopant diffusivities can be altered by changes in point defect concentrations. Therefore, to understand dopant diffusion in silicon, it is necessary to understand and model how different processes interact and thus govern point defect supersaturations.

2.2 Ion implantation damage

In this section, we briefly review the phenomenon known as transient enhanced diffusion (TED). We discuss initial conditions and assumptions which are commonly used in simulations of ion implant damage evolution and describe how damage evolves during subsequent annealing.

2.2.1 Initial damage and non-amorphizing implants

First, we briefly describe the process of ion implantation and damage production. During implantation, dopant ions enter the silicon substrate with high velocity. They undergo a series of collisions with atoms of the silicon lattice. If during the collision event the energy transfered to a lattice atom is greater than the energy of silicon bonding, the Si atom is knocked off its lattice site creating a vacancy and self-interstitial. This displaced silicon atom is referred to as a recoil or secondary ion. Recoils also collide with other silicon atoms creating other interstitials and vacancies, i.e. a collision cascade. One ion implantation may result in the formation of a large number of interstitials and vacancies (100-10,000). If the density of created damage is high enough, the substrate is amorphized.

During a post implant anneal, most of the Frenkel pairs (interstitial-vacancy pairs) recombine. This leaves us with "+1" damage, i.e. each implanted ion produces one net interstitial (I−V). Thus the net (I−V) dose is equal to implanted dose. But depending on dopant ion and implant conditions (i.e. energy, dose, substrate temperature) there are deviations from this simple model. At low temperature for example, vacancy diffusivity is higher than interstitial diffusivity. Thus vacancies can diffuse away and recombine at the surface before finding an interstitial. This leads to larger values of net (I−V) dose than predicted by "+1" also referred as "+N" factor. Therefore more careful calculations are usually necessary for the accurate estimation of net(I−V) concentration profile and "+N" number.

Fig. 2.5 shows the damage distribution after As ion implantation from Monte Carlo ion implant simulator (TRIM) [105, 14].

2.2.2 Amorphizing implants

In the case of amorphizing implants, the substrate is amorphized up to a certain depth (amorphous/crystalline interface). Everything above the amorphous/crystalline (a/c) interface is assumed to regrow into perfect silicon crystal, so only damage below the interface is left (Fig. 2.6). This interstitial rich region is also called the end of range (EOR) region. The value of amorphization threshold is a defect concentration above which the substrate is assumed to be amorphized. It is usually defined as a percentage of concentration of silicon atoms. While the threshold value is not well characterized and depends on implant conditions (temperature, dose rate), the net(I−V) dose is very sensitive to the location of a/c interface. This is one of the known difficulties in the modeling of amorphizing implants. To obtain a device junction with low sheet resistance, high doses must be implanted, and the damage produced by heavy ions such as As leads to the formation of an amorphous layer. Thus, in most cases, simulation of arsenic diffusion after ion implantation includes modeling of amorphizing implants.

2.2.3 Transient Enhanced Diffusion

It has been observed that during anneal of damage caused by ion implantation the diffusivity of dopants (such as B, P, As) is greatly enhanced. This enhancement is present for a short time and after that dopant diffusivity returns to an equilibrium levels [5, 83]. TED

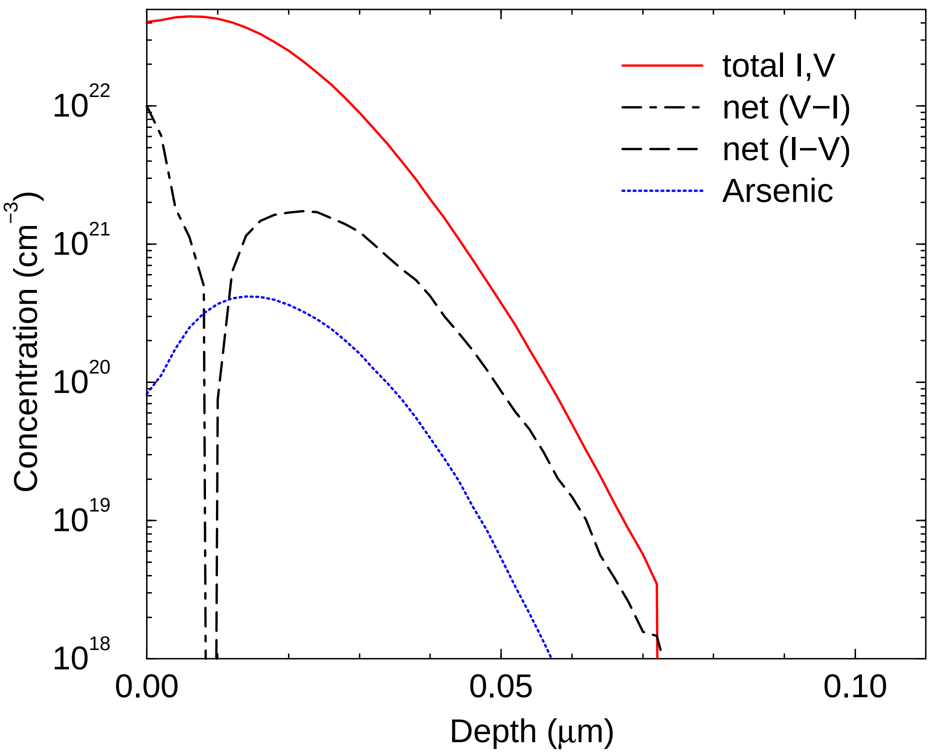

Figure 2.5: Damage after 32 keV arsenic implant from Monte Carlo ion implant simulator (TRIM) [105, 14]. Total interstitial and vacancy concentrations are almost equal and significantly larger than As concentration. During the ion implantation the fast-moving ion knocks out the silicon matrix atom leaving the vacancy and creating the interstitial. Hence the newly created interstitial has a non-zero velocity so there is a separation between the vacancy and the interstitial. Thus the V-rich region is formed near the surface while the region enriched with interstitials is deeper in the substrate. Heavier ions, like As, create larger separation between the V-rich region and I-rich region. In the case of amorphizing implant V-rich region is usually confined within the amorphous layer, thus after amorphous region regrowth only I-rich region remains in the system.

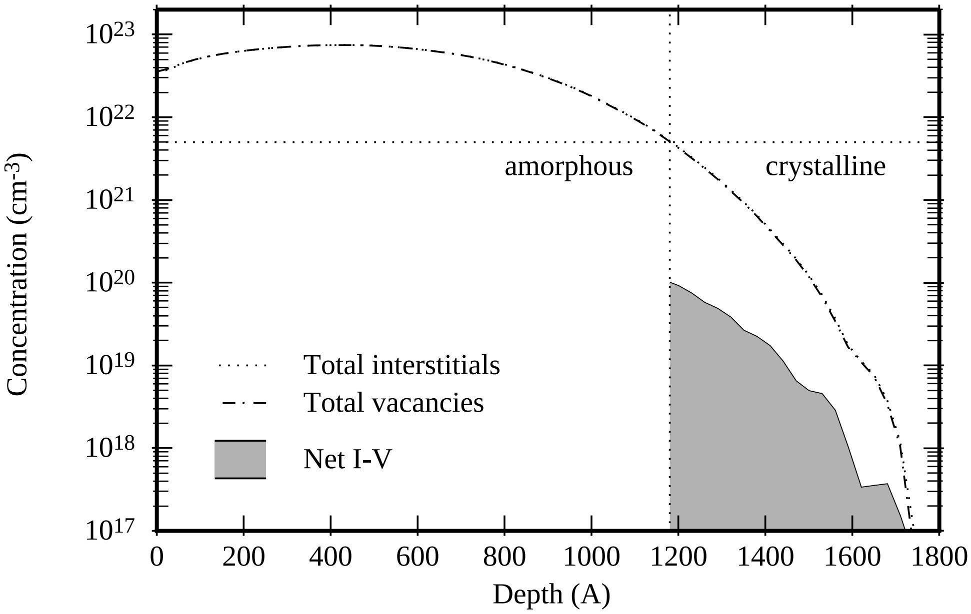

Figure 2.6: Damage after amorphizing implant from Monte Carlo ion implant simulator (TRIM) [105, 14, 44]. Total interstitial and vacancy profiles are almost equal. The horizontal dotted line represents the value of amorphization threshold, the damage concentration above which the substrate is amorphized. The vertical doted line represents the location of the amorphous/crystalline interface. After annealing the amorphous layer (everything above the a/c interface depth) regrow into the perfect crystal leaving only the damage below the interface, End of Range (EOR) damage as shown by solid filled curve. The EOR damage consists mainly of interstitial-type defects.

is believed to be related to interstitial assisted diffusion. Interstitials produced after ion implantation form self-interstitial clusters ($\{311\}$ defects or "rod-like" defects) [26, 37] during initial stages of anneal. As annealing continues, these defects undergo Ostwald ripening and then they dissolve and disappear. It was reported that the time scale of evolution of $\{311\}$ defects is approximately the same as the time scale of TED [26]. $\{311\}$ defects maintain high interstitial super-saturation through the entire time of their existence and thus enhance dopant diffusivity. More detailed modeling of $\{311\}$ defect evolution are discussed in Chapters 3 and 4.

2.3 Summary

In this section, the diffusion of dopants in silicon was reviewed. The vacancy mediated diffusion and interstitial mechanisms were described, followed by the review of ion implantation damage production and damage evolution during a subsequent thermal anneal for amorphizing and non-amorphizing implants.

Chapter 3

ENERGETICS AND KINETICS OF {311} DEFECTS IN SILICON

Molecular dynamics (MD) calculations were used to study the energy of {311} defects in silicon as a function of size and configuration. The results of these calculations were applied via the Kinetic Precipitation Model to the analysis of {311} defect growth and dissolution, which were compared to experimental observations.

3.1 Introduction

{311} defects (also called rod-like defects) are generated during annealing of ion implanted silicon. They are formed by the agglomeration of self-interstitials into planar defects which are elongated primarily in $\langle 011 \rangle$ directions and lay in {311} planes. During the annealing of ion implanted samples, extended defects form, grow, and eventually dissolve, or are converted into other defects (e.g., dislocation loops). It has been reported that the time scale of their dissolution is roughly the same as the time period over which TED [28, 37] occurs. This leads to the conclusion that {311} defects store and then release the interstitials which cause TED. Thus, understanding the structure and kinetics of growth and dissolution can help us to predict TED behavior.

The atomic structure of {311} extended defects was proposed by Takeda [100], based on high-resolution transmission electron microscopy (HRTEM) images. The defect structure consists of parallel reconstructed chains of interstitials oriented along $\langle 011 \rangle$ directions. The structure contains 5, 7, and 8-membered rings, but no dangling bonds.

We start by discussing the calculation method used (the general theory of molecular dynamics and interatomic potentials for Si will not be reviewed here, but can be found elsewhere [3, 88]). We then describe considered defect configurations and associated calculation results. Next, we parameterize our results to obtain the minimum defect energy as a function of size. This functional dependence is applied in continuum simulations via the Kinetic Precipitation Model (KPM) [32, 43] and compared to TEM observations of Eaglesham *et al.* [37].

3.2 Method of calculation

For calculation of the energy of a range of defect configuration we use constant-temperature MD with empirical interatomic potentials. Stillinger-Weber (SW) [98] and Environment Dependent Interatomic Potential (EDIP) [10, 11, 58] are the specific potentials which have been used. The choice of the SW potential is due to its wide availability and use, so its major advantages and failures have been reported. EDIP is a more recent advancement which has been specifically fitted to a set of *ab-initio* data of various defect structures. It has a more complicated functional form with 13 fitted parameters, but with a shorter cut-off radius of 3.12Å vs. 3.77Å for the SW potential, it is actually more computationally efficient for large systems.

To simulate {311} extended defects, we use computational super-cells with primary axes along $[2\bar{3}\bar{3}]$, [311], and $[0\bar{1}1]$ directions. The orthogonal unit cell consist of 88 atoms with unit length of $L_{0\mathrm{x}} = a\sqrt{11}$, $L_{0\mathrm{y}} = a\sqrt{22}$, $L_{0\mathrm{z}} = a/\sqrt{2}$, where a =5.43Å is a silicon lattice constant. The computational super-cells were formed by duplication of the unit cell along primary axes. The super-cell size has been chosen to be large enough in each simulation to eliminate any significant displacement of peripheral atoms with respect to ideal lattice sites. Periodic boundary conditions are applied in all three directions. For calculations, we use the parallel MD simulator MDCASK [20].

For each given defect structure, MD simulations were run to calculate the total energy of the system and to ensure stability of the configuration. First the atomic positions were relaxed at 0.1°K, then calculations were performed at 300–600°K temperature for 20000 time steps (about 1 ps) to check the stability of the configuration. After that, the system was relaxed again at 0.1°K to obtain the total energy. For temperature control, we used Langevin dynamics.

The total formation energy of a given defect configuration is defined as

$$E_f^{\text{tot}} = E(N^{\text{def}} + N^{\text{perf}}) - \frac{N^{\text{def}} + N^{\text{perf}}}{N^{\text{perf}}} E(N^{\text{perf}}) \tag{3.1}$$

where N^{def} is the number of self-interstitials, N^{perf} is the number of atoms in the perfect crystal structure, and $E(N^{\text{perf}})$ and $E(N^{\text{def}} + N^{\text{perf}})$ are the energies of the perfect crystal and the structure with an extended defect, respectively. The formation energy per interstitial is defined as $E_f^{\text{avg}} = E_f^{\text{tot}}/N^{\text{def}}$. Our calculations confirm that, as previously reported, the $\langle 110 \rangle$ split interstitial is the lowest energy configuration for a single self-interstitial for both SW and EDIP potentials [58]. Our calculations give $E_f^{\text{I}} = 4.45$eV for SW potential and 3.4eV for EDIP.

The atomic structure of $\{311\}$ defects has been proposed based on HRTEM images [100], and examined by a number of different computation techniques [61, 63]. It is believed that $\{311\}$ defects are formed by interstitial chains in the $\langle 011 \rangle$ direction, arranged next to each other at distances of 6.37Å or 12.74Å. For the larger spacing, the interstitial chains are separated by a structure containing eight-membered rings, but no extra atoms. We follow the recipe of Kim *et al.* [61] to construct different defect configurations. Interstitial chains of finite length L were placed in $\{311\}$ direction without any separation units to form a rectangular-shape defect($E\underbrace{I \cdots I}_{\text{W}}E$ in the notation of Takeda *et al.* [100, 63]). Fig. 3.1 presents an example of two interstitial chains in $\langle 011 \rangle$ direction, arranged next to each other.

3.3 Results

We find that, as expected, the formation energy per interstitial E_f^{avg} decreases for longer chains. As can be seen from Fig. 3.2, the formation of wider clusters is preferred for larger sized defects, while small defects tends to be narrower. The crossover point in energy for defects with different length to width ratios correspond to two defect configurations with the same number of interstitials and total energy, but having different aspect ratios. Beyond this point, the wider defect is energetically more favorable. However, beyond about three or four chains, the energy reduction in going to wider chains even for very large defects becomes

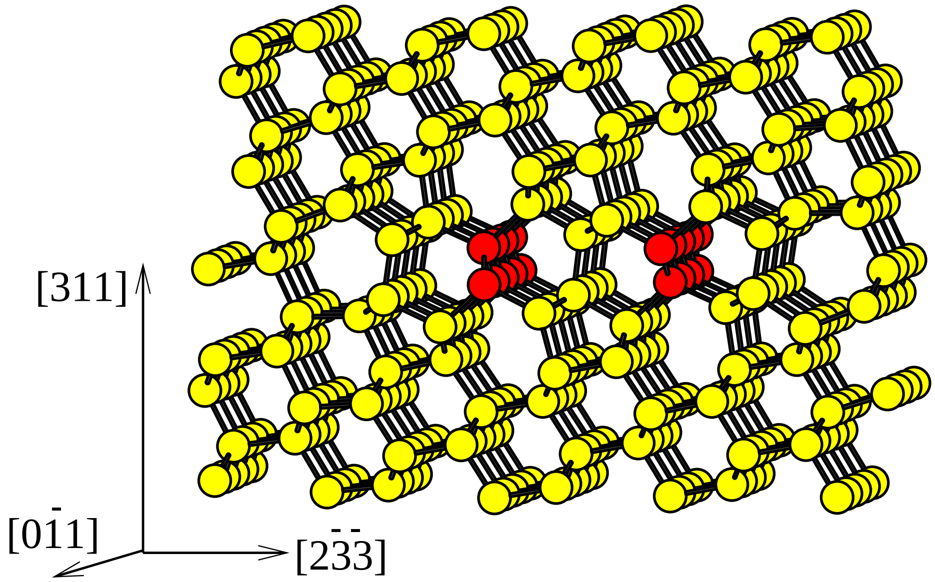

Figure 3.1: Two interstitial chains (dark circles) in $\langle 011 \rangle$ direction, arranged next to each other at distance of 6.37Å. Defect structure contains 5, 7 and 8-membered rings but does not have any dangling bonds.

very small. This is consistent with the experimental observation that for visible defects, the defect width remains approximately constant at about 4nm [37]. This is equivalent to a width of 5 chains as they are spaced at a distance of 6.37Å, with an additional structure of equivalent width on each side.

Fig. 3.3 shows the total formation energy of small rectangular-shaped defects as a function of chain length for different widths. The simple approximation formula

$$E_f^{\text{tot}} = C_1 W + C_2 L + C_3 W L \tag{3.2}$$

interpolates these MD calculations results fairly well, where W and L are the defect width and length respectively measured in number of interstitials, C_1 and C_2 represent the extra energy associated with the edges, while the last coefficient C_3 represents an area (or total number of defects) term. Table 1 summarize results of interpolation constants for SW and EDIP potentials. Also shown is E_f^{∞}, which is the calculated value of energy per interstitial for an infinitely large planar defect. The difference between C_3 and E_f^{∞} shows that Eq. 3.2 cannot be used effectively to extrapolate to larger sizes. We found that the following

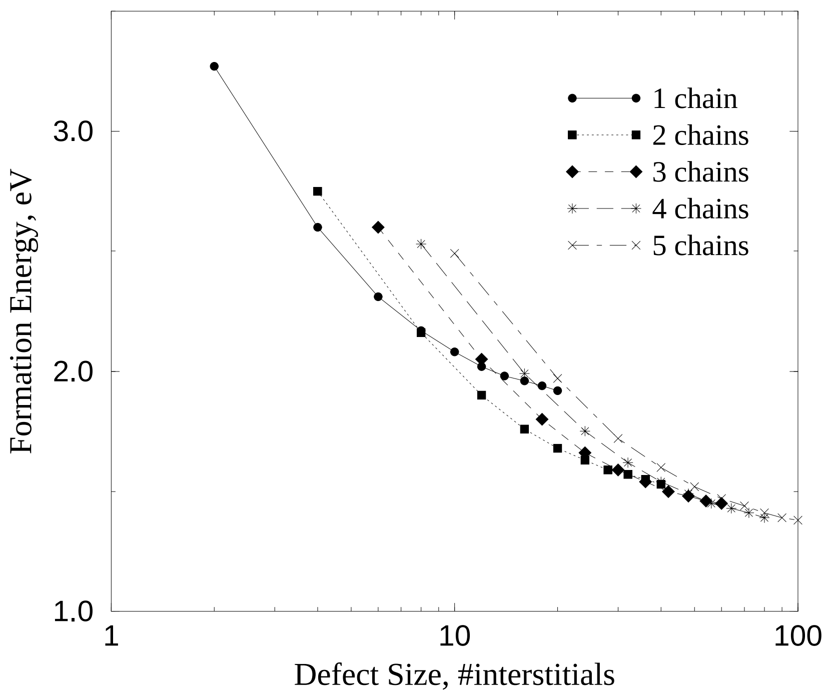

Figure 3.2: SW potential has been used to calculate formation energy of extended defect per interstitial $E_f^{\rm avg}$ with respect to the number of interstitials in defects for different configurations. The crossover points correspond to defects with different aspect ratio but the same formation energy. There is only a small gain in energy for widening more than up to width 3 or 4.

Table 3.1: Coefficients of interpolation functions for SW and EDIP potentials. All parameters are in units of eV.

	C_1	C_2	C_3	E_f^∞	β_1	β_2	α
SW	2.82	0.63	1.10	1.24	0.59	2.72	2.05
EDIP	3.32	0.62	1.25	1.39	0.51	3.38	2.3

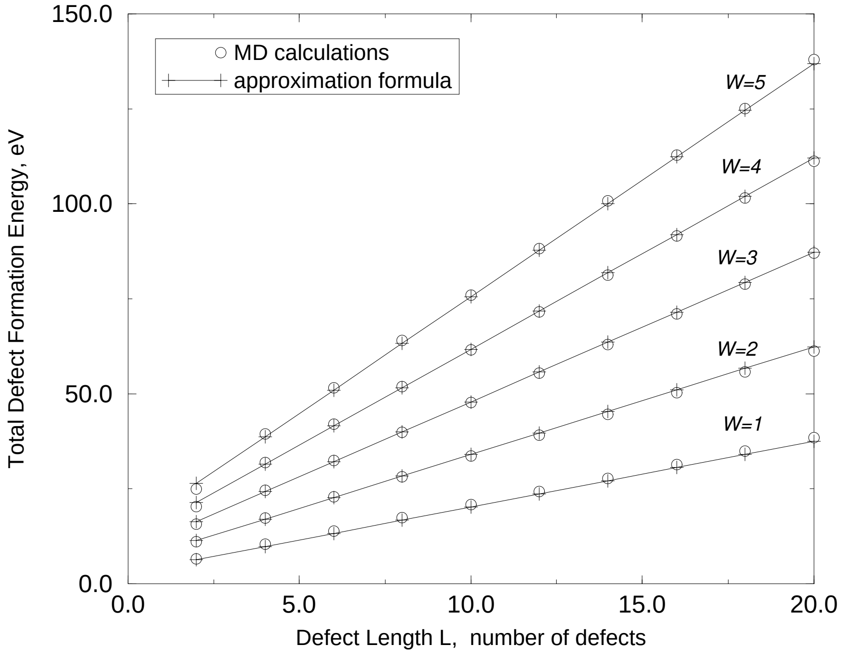

Figure 3.3: Total formation energy of defect with respect to defect length for different defect widths W. The analytical expression Eq. 3.2 (solid line) fit to the MD calculation (open circles) shows a good agreement with data points. Simulation results obtained with SW potential.

expression interpolates result, including large size behavior, much more accurately:

$$E_f^{\text{tot}} = WL\left(E_f^{\infty} + \beta_1 W^{-\alpha}\right) + \beta_2 W \tag{3.3}$$

We also studied non-rectangular defect configurations to obtain the energetics of capture of isolated interstitials by {311} extended defects. In particular, we examined energies associated with partial $\langle 011\rangle$ interstitial chains arranged parallel to existing rectangular defects. For the simulations, we used $3\times2\times14$ computational supercells with 7392 atoms plus the number of atoms in the extended defect. Total energy analysis of these configurations showed that the energy is almost independent of where the partial chains were located along the length of the extended defect. Results for defects of length 12 and various widths are shown in Fig. 3.4, with the energy difference per interstitial plotted for each new pair of interstitials added to the existing defect. Our calculations show that there is a substantial energy penalty for adding the first pair of interstitials starting a new chain, but the energy needed for adding more interstitials to partial chains is lower and approximately constant. Note also that the energy is higher to form the first chain and slightly lower for the second chain, but approximately equal for subsequent chains.

Since the {311} defect structures may not be the lowest energy configurations, a larger range of configurations for small defect clusters needed to be analyzed in order to obtain an accurate dependence of energy on extended defect size. We simulated interstitial cluster energies starting with a range of initial configurations, including the structures proposed by Arai *et al*. [6] and Bongiorno *et al.* [15], as well as interstitial chains in the $\langle 011\rangle$ direction. The initial configurations were annealed via MD simulations at 900°C and then quenched. The resulting formation energies per interstitial for the lowest energy configurations are shown in Table 3.2.

Assuming that transitions between configurations occur readily, what is most important for extended defect growth is the minimum energy for any given defect size (number of incorporated interstitials). We can minimize Eq. 3.3 with respect to width keeping the total number of interstitials in defect constant to find the optimum aspect ratio: $W_{opt} =$

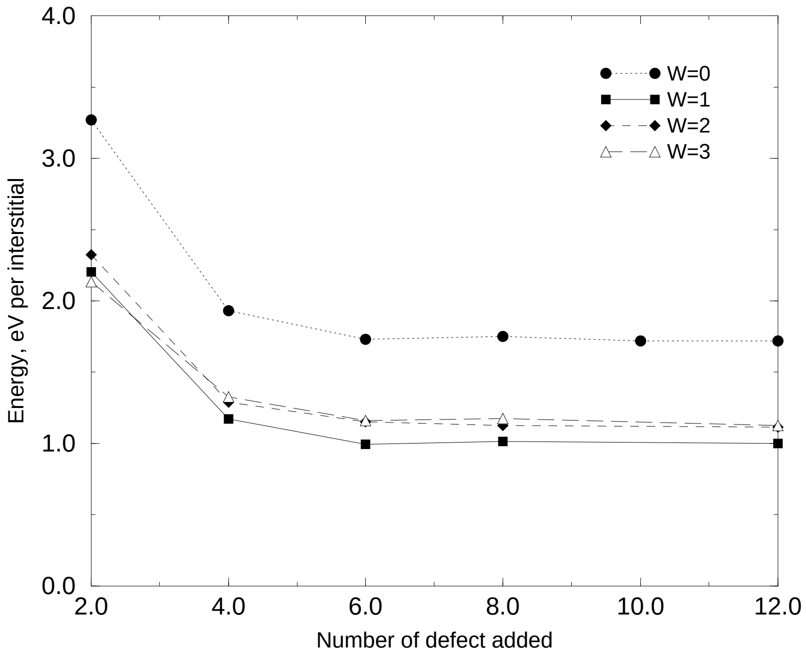

Figure 3.4: Energy per interstitial for adding extra pairs of interstitials to an existing defect of length 12 and varying width. Simulation results obtained with SW potential.

Table 3.2: Formation energies (in eV) per interstitial E_f^{avg} for small interstitial clusters. I_n stands for the compact cluster with n interstitials.

	I_2	I_3	I_4
SW	3.1	2.4	2.15
EDIP	3.04	2.37	2.20

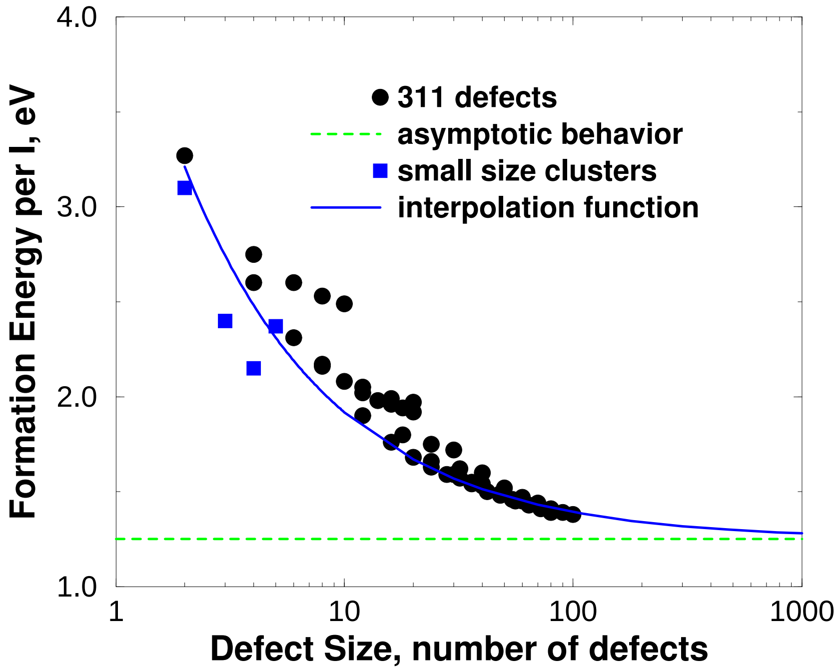

Figure 3.5: Comparison of minimum {311} energy per interstitial from interpolation function versus size (Eq. 3.4) to MD simulations (SW potential). Also shown are the calculated minimum energies of small clusters and associated interpolation function (Eq. 3.4).

$(n\beta_1/\beta_2)^{1/(1+\alpha)}$. For this aspect ratio, the minimum energy as a function of defect size n is

$$E_f^{min} = E_f^{\infty} n + 2\beta_2 \left(\frac{\beta_1 n}{\beta_2}\right)^{1/(1+\alpha)} \tag{3.4}$$

This expression is compared to MD calculations in Fig 3.5. Also shown are the energies of smaller clusters, which are significantly below that of {311} defects for sizes 2, 3, and 4.

3.4 Evolution of {311} *defects*

To model the evolution of {311} defects, we have applied the Full Kinetic Precipitation Model (FKPM) [32] to interstitial aggregation. The driving force for {311} formation is minimization of the free energy of the system. The difference in free energy between n

isolated interstitials and a size n extended defect is given by:

$$\Delta G_n = -nkT \ln \frac{C_I}{C_{ss}} + \Delta G_n^{exc}, \tag{3.5}$$

where C_{ss} is the effective solid solubility of interstitials associated with the formation of $\{311\}$ defects (concentration of interstitials at equilibrium with an infinitely large defect), and ΔG_n^{exc} is the excess energy associated with a defect of finite size n. We consider discrete equations up to size 1000 to avoid any finite size effects.

During TED, the surface is the main sink for interstitials. We use a simple surface recombination velocity. Surface recombination, I/V recombination and $\{311\}$ growth are all assumed to be diffusion limited. Bulk point defects diffusivity/equilibrium concentration (e.g., $D_{\mathrm{I}}C_{\mathrm{I}}^{*}$) are from metal diffusion [16, 17, 22] with diffusivities taken from MD calculations [101, 55]. The initial defect profiles are calculated from Monte-Carlo simulations using UT-MARLOWE [78]. The system has been implemented in DOPDEES [42].

Eaglesham *et al.* [37] implanted 5×10^{13} cm^{-2} Si implants at 40 keV and annealed the samples at 815°C and 670°C. They measured the resulting $\{311\}$ densities using transmission electron microscopy (TEM) and reported the moments of this distribution. We use our expression for energy as a function of defect size Eq. 3.4 for defects of size 8 and larger (Fig. 3.5). We used the calculated energies of the small compact clusters of sizes 2, 3, and 4. Since no information about the energy barrier and/or the pathway for compact cluster to transform into the $\{311\}$-type defect is obtained we assume that the energy per defect is constant for small sizes 5, 6 and 7 and is equal to the energy per interstitial of a size four defect (and $\{311\}$-type defect of size 8). One fitting parameter C_{ss} is used in the simulation to fit the evolution of the number of interstitials in these defects.

It can be seen that we are able to obtain a good agreement with experimental data Fig. 3.6. We also found that the results are quite sensitive to the assumption made about the energies of small-sized defects. We repeated calculations with energies obtained by EDIP potential but are not able to get a good match to experimental data. EDIP gives a lower formation energy of isolated interstitial and higher energy per interstitial of large size defect compared to SW, hence giving less driving force for defect growth. Comparison of the size distribution produced by our model to the average size reported in experiment

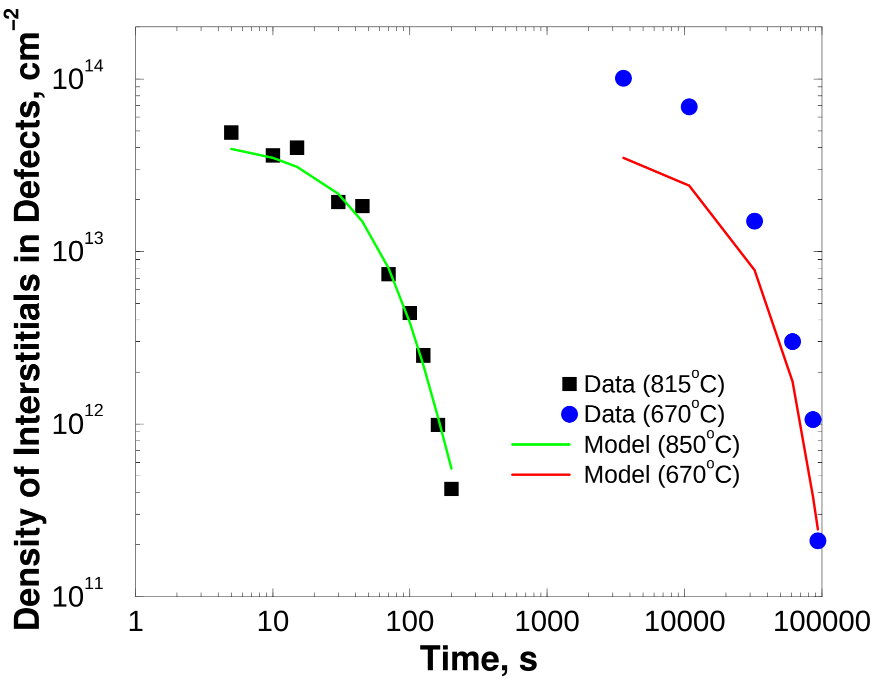

Figure 3.6: Comparison of FKPM predictions to evolution of density of interstitials in {311} defects. Simulations show good match to experimental observations at both temperatures. Data from Eaglesham *et al.* [37] for 5×10^{13} cm^{-2} Si implants at 40 keV annealed at 815°C.

shows that we considerably underestimate average size of the defect. This may be caused by estimation of energies of small clusters, since there is a big energy gain in agglomeration of free interstitials into defects of size 2, 3, 4 but less gain in formation of larger defects. Further examination of small clusters energies and cluster growth kinetics are required for more complete understanding of {311} nucleation and growth/shrinkage.

3.5 Conclusions

In summary, we used MD simulations with empirical potentials (SW and EDIP) to calculate the energy versus size and shape for interstitial aggregates, particularly {311} defects. Using the calculated energy versus size relationship, we compared the predicted {311} kinetics to experimental observations of $\{311\}$ growth/dissolution.

Chapter 4

SELF-INTERSTITIAL CLUSTERS IN SILICON

In Chapter 3, we demonstrated that the simulation of {311} defects is quite sensitive to the assumptions we made regarding the structure and energy of small interstitial clusters. In this chapter, we analyze the initial stages of agglomeration of self-interstitial clusters and present a computationally efficient model. This model takes into account both small interstitial clusters as well as {311} defects.

4.1 Introduction

Atomistic calculations are used by various researchers to study small self-interstitial clusters [60, 61, 6]. Several structures (also referred to as *compact clusters*) are reported to be stable with respect to isolated interstitials and more stable than elongated ({311}-type) defects of the same size. However, compact clusters have very different structures than elongated defects, leaving the question of the pathway from one type of cluster to another open.

One commonly used experimental method to study self-interstitial agglomerates in Si is TEM observation. However, it is virtually impossible to identify small clusters containing less than 10 self-interstitials, even by High Resolution TEM. Another technique used to study small interstitial clusters and {311} defects is based on boron marker layer diffusion. Marker layer diffusion enhancement is measured as a function of time, and conclusions can be made on the energetics and stability of defects, since lower interstitial supersaturation corresponds to more stable defects. At temperatures above 800°C, interstitial clusters grow rapidly, and no useful information can be extracted about small clusters, since the average size increases to dozens or even hundreds of interstitials within the first few seconds of annealing. To effectively slow down growth, experiments should be carried out at low

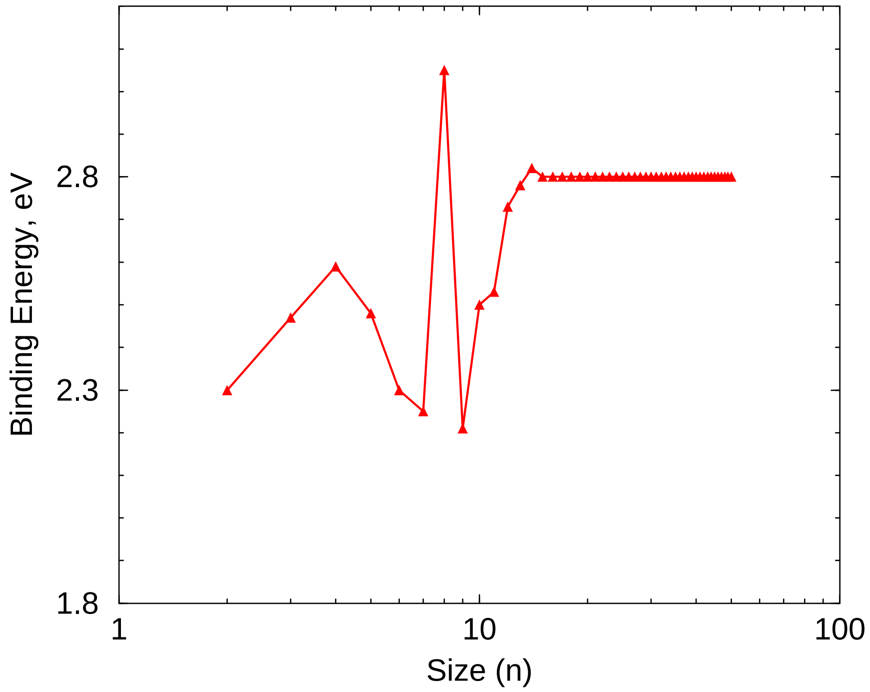

Figure 4.1: Binding energy for interstitial clusters as a function of size reported by Cowern *et al.* [27]. The peaks correspond to the most stable clusters of size 4 and 8.

temperatures. In experiments by Cowern *et al.* [27] described below, anneals were performed at 600°C, 700°C and 800°C at times as short as 1 sec.

4.2 Overview of Experiment

Cowern *et al.* measured TED of B-doped marker layers to determine the transient interstitial supersaturation during cluster formation and growth. $2 \times 10^{13}\,\mathrm{cm}^{-2}$ Si^{+} were implanted at 40keV and annealed at 600°C, 700°C and 800°C for various times [27]. They used inverse modeling to derive the binding energy, $E_{\mathrm{b}}(n)$, versus size relationship for self-interstitial clusters from interstitial supersaturation. The extracted values for $E_{\mathrm{b}}(n)$ are shown in Fig. 4.1. They found two energetically stable small clusters at sizes four and eight with less stable adjacent clusters at sizes seven and nine. Near-constant behavior was assumed for large $(n > 15)$ rod-like defects.

Cowern *et al.* [27] derived their model based on the assumption that small self-interstitial clusters grow and transform into {311}-type defects. More recent theoretical studies [81] have not found any energetically favorable transition pathways between small compact structures and elongated {311} defects. Also, the number of parameters optimized by Cowern *et al.* exceeded the number of data points available from the experiment. Therefore, in this chapter, we present our study of small interstitial clusters based on the experimental data from Cowern *et al.* [27] and on the assumption that no transition between these compact clusters and {311} defects occurs for clusters of size three and larger, and thus they interact only via the concentration of free interstitials and di-interstitials.

4.3 Model

4.3.1 Full Set of Reaction Rate Equations

Our MD calculations (presented in Chapter 3) and *ab-initio* results by Kim *et al.* [60] indicate that the compact cluster of size 4 is energetically more favorable than the elongated defect of size 4, while {311}-type defect of size 5 is more energetically stable than the compact cluster of size 5. Hence, we assume that there exist two populations of interstitial clusters: small compact clusters up to size 4 and {311} defects (size 3 and up). There is no transformation between the two and their behavior is only related through the supersaturation of free interstitials. A size 2 {311}-type defect is assumed to be the same as size a 2 compact cluster.

Growth and dissolution of self-interstitial clusters is generally assumed to proceed by absorption or emission of a single interstitial [43], e.g. cluster I_n can grow or dissolve with addition or release of interstitial I:

$$\mathrm{I}_n + \mathrm{I} \Leftrightarrow \mathrm{I}_{n+1}. \tag{4.1}$$

$$\frac{\partial C_{\mathrm{I}_n}}{\partial t} = R_{\mathrm{I}_n/\mathrm{I}} \tag{4.2}$$

$$\frac{\partial C_{\mathrm{I}}}{\partial t} = \begin{cases} -R_{\mathrm{I}_n/\mathrm{I}}, & n \geq 2 \\ -2R_{\mathrm{I}/\mathrm{I}}, & n = 1 \end{cases} \tag{4.3}$$

The rate of formation of size $n+1$ cluster from size n cluster is given by

$$R_{\mathrm{I}_n/\mathrm{I}} = 4\pi\lambda_n D_{\mathrm{I}} \left(C_{\mathrm{I}_n} C_{\mathrm{I}} - \frac{C_{\mathrm{I}_{n+1}}}{K_{\mathrm{I}_n/\mathrm{I}}} \right), \tag{4.4}$$

where D_{I} is the interstitial diffusivity, λ_n is the reaction capture radius and should be estimated based on cluster geometry. For compact clusters we assume a linear dependence of capture radius on cluster size, $\lambda_n = na_0/2$, where a_0 is silicon lattice constant, while for $\{311\}$ defects we use the analysis of Gencer based on calculation of the steady state diffusion field around a rectangular shaped precipitate [44].

The equilibrium constants, $K_{\mathrm{I}_n/\mathrm{I}}$ are given as,

$$K_{\mathrm{I}_n/\mathrm{I}} = \left(\frac{1}{C_{\mathrm{Si}}} \right) \exp\left[\frac{E_b(n)}{kT} \right], \tag{4.5}$$

where $C_{\mathrm{Si}} = 5 \times 10^{22}\,\mathrm{cm}^{-3}$ is the density of silicon atoms, $E_b(n) = E_f(n) - (E_f(n-1) + E_f(1))$ is the binding energy, and $E_f(n)$ is the formation energy of a cluster of size n. In our simulations the binding energies of small clusters ($E_b(2)$, $E_b(3)$ and $E_b(4)$) are free parameters. From Eq. 3.2 the optimum aspect ratio is given by $W_{opt} = \sqrt{C_2 n/C_1}$, and for this aspect ratio the minimum energy of a defect is given by:

$$E_f^{min}(n) = A_1\sqrt{n} + C_3 n, \tag{4.6}$$

where $A_1 = 2\sqrt{C_1 C_2}$. Since the absolute values calculated via empirical MD are not very accurate, we keep the functional form of Eq. 4.6 while using A_1 and C_3 as the free parameters to be determined during the simulation. Discrete reactions are solved at each size up to size 1000 to avoid any finite size effects. A "+1" model has been assumed, and the problem has been solved on a single grid point to reduce computational time.

The PROFILE [82] non-linear optimization software package has been used to determine the values of the fitting parameters. The 600°C and 800°C supersaturation data from Cowern *et al.* [27] and experimental data from Eaglesham *et al.* [37] on density evolution of $\{311\}$ defects at 815°C have been used for the parameter optimization. Fig. 4.2 shows a comparison of simulation results to interstitial supersaturation from Cowern *et al.* [27]. The comparison of evolution of density of interstitials in $\{311\}$ defects to experimental data from Eaglesham *et al.* [37] is presented in Fig. 4.3.

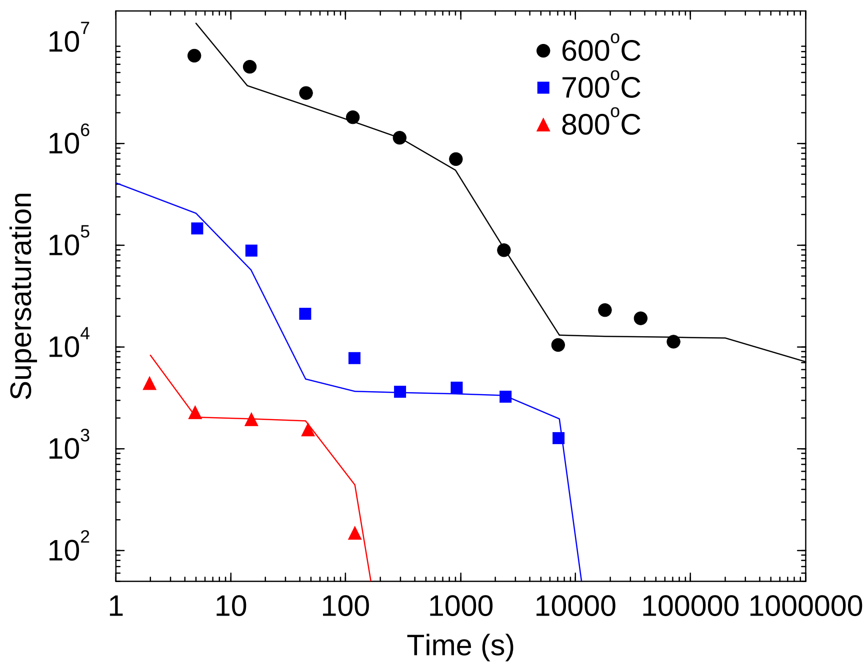

Figure 4.2: Interstitial supersaturation as a function of annealing time and temperature. Symbols represent experimental values from Cowern *et al.* [27]. Solid lines represent simulation results.

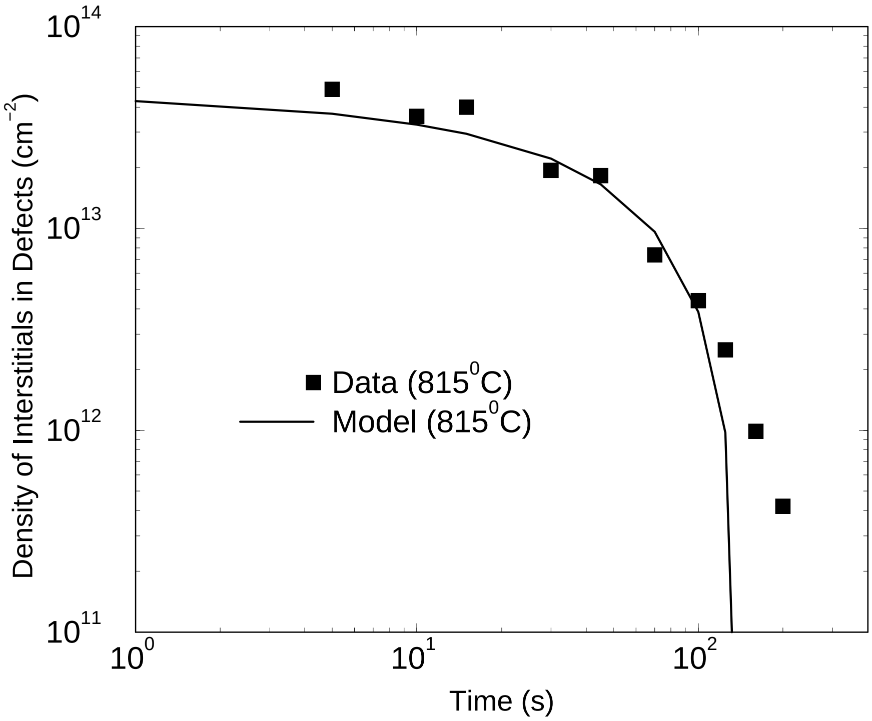

Figure 4.3: Comparison of the full model predictions to evolution of density of interstitials in {311} defects. Simulations show good match to experimental observations. Data from Eaglesham *et al*. [37] for 5×10^{13} cm^{-2} Si implants at 40 keV annealed at 815°C.

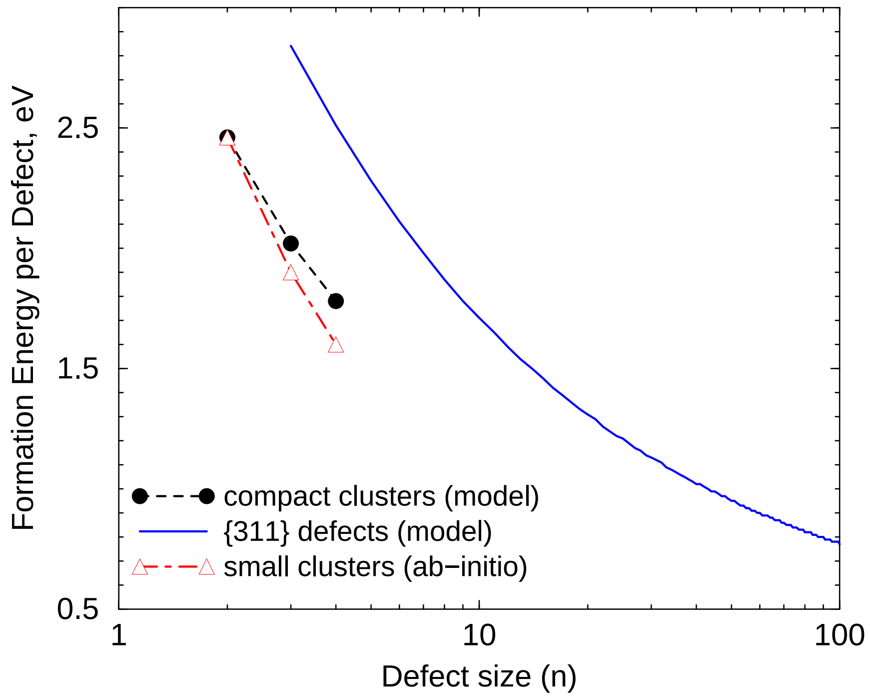

Figure 4.4: Energy as a function of size extracted by our analysis. Solid circles represent the formation energy per defect for compact clusters, solid line is the energy per defect for {311} defects. The open triangles represent the *ab-initio* results from Kim *et al.* [60] for the compact clusters plotted for comparison.

Interstitial cluster formation energies extracted by our analysis are plotted in Fig. 4.4. The open triangles represent formation energies energies of compact clusters calculated by Kim and co-workers [60] plotted for comparison. We would like to note that the formation energy of self-interstitial given by *ab-initio* calculations [60], $E_f(1)$=3.35 eV, is different from the value we use in our simulations, $E_f(1)$=3.78 eV, based on experimental data for silicon self-diffusion ($D_{\mathrm{I}}C_{\mathrm{I}}^*$ by Ural *et al.* [104]) and MD calculations for silicon diffusivity [55], so the difference is expected to be present.

Fig. 4.5 shows a typical size distribution after anneal at 600°C. At short times, the peak corresponds to the most stable small cluster at size four. Because the energy is smooth and a monotonic function of size for {311} defects, the size distribution and evolution for large clusters is also a well behaved function. At longer times the distribution peak shift towards

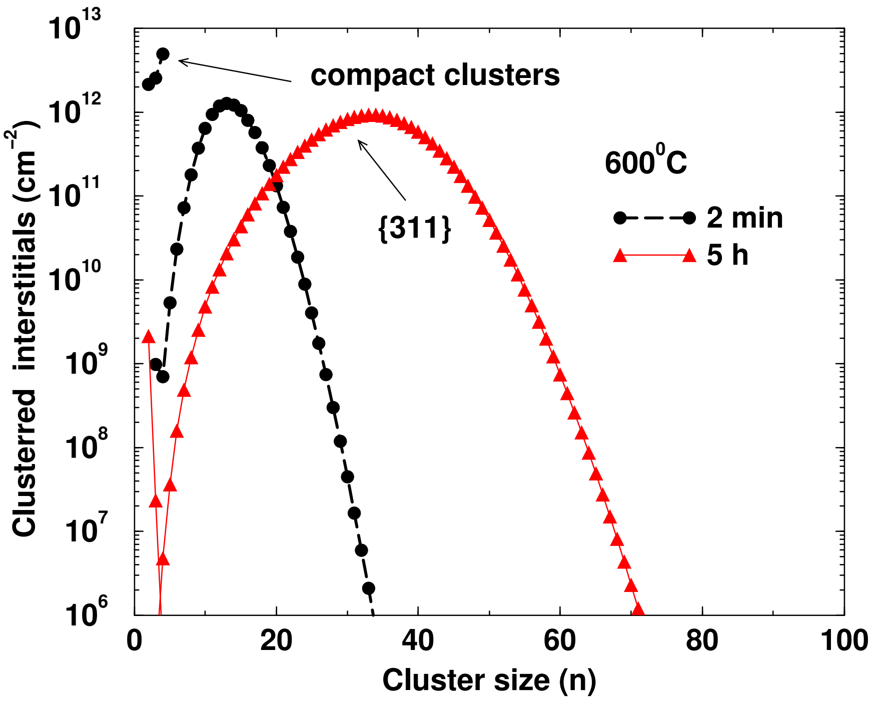

Figure 4.5: Time evolution of the cluster size distribution at 600°C.

the larger clusters. These larger defects are energetically more favorable and maintain lower supersaturation of interstitials as can be see in Fig. 4.2.

4.3.2 Moment-Based Model

The set of discrete rate equations described above is computationally very expensive, since the full size distribution is tracked at each point in space. If the problem is solved in multiple spatial dimensions the number of equations becomes prohibitively large. Clejan *et al.* developed a more efficient approach based on considering the size distribution in terms of a small number of moments [25]. Only the evolution of those moments are considered rather than the full distribution.

We use discrete rate equations for small clusters up to size 4 and a moment based approach for {311} defects ($n \geq k$, $k = 3$). The moments are defined as:

$$m_i = \sum_{n=k}^{\infty} n^i f_n, \tag{4.7}$$

where $i = 0, 1, 2, ...$, and $f_n = C_{\mathrm{I}_n}$ is a size distribution. The zero-th order moment of the distribution is simply the precipitate density, while the first moment corresponds to the density of precipitated solute atoms. Higher order moments further describe the shape of the size distribution. This transforms the system for large size clusters to the following set:

$$\frac{\partial m_i}{\partial t} = k^i R_2 + \sum_{n=k}^{\infty} \left[(n+1)^i - n^i \right] R_n \tag{4.8}$$

Note that the sums over the R_n can be written in terms of sums over f_n, nf_n, etc. Hence, they can be calculated from the moments if moments are used to describe the distribution. This reduces the system of equations to:

$$\begin{aligned}
\frac{\partial m_i}{\partial t} &= D_{\mathrm{I}} \left[k^i \lambda_{k-1} C_{\mathrm{I}} f_{k-1} + m_0 C_{\mathrm{I}} \gamma_i^+ - m_0 C_{\mathrm{ss}} \gamma_i^- \right] \\
\gamma_i^+ &= \sum_{n=k}^{\infty} \left[(n+1)^i - n^i \right] \lambda_n \hat{f}_n \\
\gamma_i^- &= (k-1) \lambda_{k-1} \hat{C}_{k-1}^* \hat{f}_k + \sum_{n=k}^{\infty} \left[n^i - (n-1)^i \right] \lambda_{n-1} \hat{C}_{n-1}^* \hat{f}_n
\end{aligned} \tag{4.9}$$

where $\hat{C}_n^* = C_n^* / C_{\mathrm{ss}}$ and $\hat{f}_n = f_n / m_0$.

Since we want to develop the most computationally efficient model, we consider the possibility of representing the system in terms of its first two moments following the work of Gencer and Dunham [44]. This reduces the system for large size evolution to:

$$\begin{aligned}
\frac{\partial m_0}{\partial t} &= D_{\mathrm{I}} \left(\lambda_{k-1} C_{\mathrm{I}} \hat{f}_{k-1} - m_0 C_{\mathrm{ss}} \gamma_0^- \right) \\
\frac{\partial m_1}{\partial t} &= D_{\mathrm{I}} \left(k \lambda_{k-1} C_{\mathrm{I}} \hat{f}_{k-1} + m_0 C_{\mathrm{I}} \gamma_1^+ - m_0 C_{\mathrm{ss}} \gamma_1^- \right) \\
\frac{\partial C_{\mathrm{I}}}{\partial t} &= -\frac{\partial m_1}{\partial t} + (k-1) \frac{\partial m_0}{\partial t} \\
\frac{\partial \hat{f}_{k-1}}{\partial t} &= -\frac{\partial m_0}{\partial t}
\end{aligned} \tag{4.10}$$

where

$$\gamma_0^- = \lambda_{k-1} \hat{C}_{k-1}^* \hat{f}_k$$

$$\begin{aligned}\gamma_1^+ &= \sum_{n=k}^{\infty} \lambda_n \hat{f}_n \\ \gamma_1^- &= (k-1)\gamma_0^- + \sum_{n=k}^{\infty} \lambda_{n-1} \hat{C}^*_{n-1} \hat{f}_n\end{aligned} \tag{4.11}$$

In order to solve this system of equations we need to assume that it is possible to write gammas in terms of moments for which we are solving, m_0 and m_1. Since γ_i are the functions of normalized size distribution function $\hat{f}_n$, we assume they depend on m_0 and m_1 only through the ratio $\hat{m}_1 = m_1/m_0$, the average size.

Using the full set of rate equations, it is now possible to calculate γ_i numerically. The full rate equation model was simulated at a single grid point. A large maximum size of 1000 was chosen to remove any errors due to pile-up at the largest size. The simulation was run for different times to extract γ_i and $\hat{m}_1$. Fig. 4.6 shows γ_i plotted against $\hat{m}_1$ extracted from the full model. In the reduced model only Eq. 4.11 and Eq. 4.1 for small sizes 2, 3, and 4 need to be solved. Now γ_i can be replaced by piece-wise interpolation function.

4.3.3 Recombination with Vacancies

Since we intend to use our model for the simulation of post-implant damage evolution we need to include the recombination reactions of interstitials and clusters with vacancies. Free interstitials can recombine with free vacancies as:

$$\mathrm{I} + \mathrm{V} \Leftrightarrow \emptyset. \tag{4.12}$$

The reaction rate is given by:

$$R_{\mathrm{I/V}} = 4\pi a_0 (D_{\mathrm{I}} + D_{\mathrm{V}}) \left(C_{\mathrm{I}} C_{\mathrm{V}} - C^*_{\mathrm{I}} C^*_{\mathrm{V}} \right), \tag{4.13}$$

where D_{V} is vacancy diffusivity, * denotes the equilibrium concentrations of point-defects, a_0 is silicon lattice spacing.

Vacancies may also recombine with interstitial clusters:

$$\mathrm{I}_{n+1} + \mathrm{V} \Leftrightarrow \mathrm{I}_n. \tag{4.14}$$

The reaction rate is given by:

$$R_{\mathrm{I}_{n+1}/\mathrm{V}} = 4\pi \lambda_{n+1} D_{\mathrm{V}} \left(f_{n+1} C_{\mathrm{V}} - \frac{f_n}{K_{\mathrm{I}_{n+1}/\mathrm{V}}} \right), \tag{4.15}$$

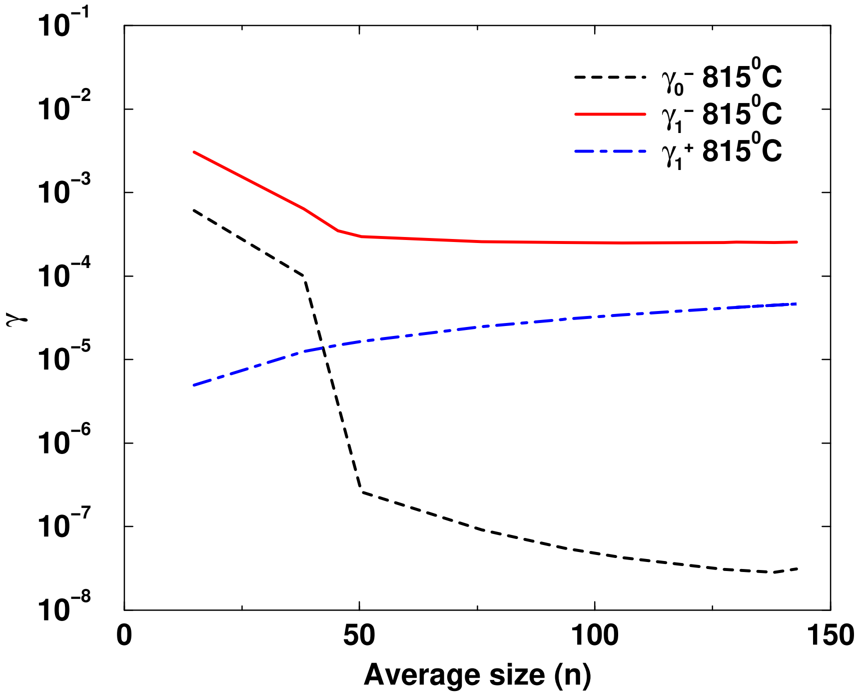

Figure 4.6: γ_0^-, γ_1^-, and γ_1^+ extracted from the full system of rate equations for 815°C. In the reduced model, gammas are replaced by piece-wise approximated functions.

with equilibrium constant given by:

$$K_{\mathrm{I}_{n+1}/\mathrm{V}} = \frac{1}{K_{\mathrm{I}_n/\mathrm{I}} C_{\mathrm{I}}^* C_{\mathrm{V}}^*}. \tag{4.16}$$

During the post-implant anneal the concentration of point-defects is much larger than the equilibrium values. Hence, we can simplify the recombination reactions. Under these conditions the reverse reactions of Eq. 4.14 is negligible and can be ignored, with the reaction rate given by:

$$R_{\mathrm{I}_{n+1}/\mathrm{V}} = 4\pi\lambda_{n+1} D_{\mathrm{V}} f_{n+1} C_{\mathrm{V}}. \tag{4.17}$$

Taking the sum over all recombination rates (Eq. 4.17) and taking into consideration the definitions of the γ_i and moments, we can write the recombination reactions in terms of the first two moments of the size distribution:

$$\begin{aligned}
\frac{\partial m_0}{\partial t} &= -D_{\mathrm{V}} C_{\mathrm{V}} m_0 \beta_0^{I/V} && (4.18)\\
\frac{\partial m_1}{\partial t} &= -D_{\mathrm{V}} C_{\mathrm{V}} m_0 (\Big(k-1)\beta_0^{I/V} + \gamma_1^+ \Big) && (4.19)\\
\frac{\partial C_{\mathrm{V}}}{\partial t} &= -D_{\mathrm{V}} C_{\mathrm{V}} m_0 \gamma_1^+ && (4.20)\\
\frac{\partial f_{k-1}}{\partial t} &= D_{\mathrm{V}} C_{\mathrm{V}} m_0 \beta_0^{I/V}, && (4.21)
\end{aligned}$$

where

$$\beta_0^{I/V} = \gamma_0^- \frac{\lambda_k}{\lambda_{k-1}} \frac{1}{\hat{C}_{k-1}^*}. \tag{4.22}$$

Finally we can write down the full system of equations for the reduced model including recombination with vacancies:

$$\begin{aligned}
\frac{\partial m_0}{\partial t} &= D_{\mathrm{I}} \left(\lambda_{k-1} C_{\mathrm{I}} \hat{f}_{k-1} - m_0 C_{\mathrm{ss}} \gamma_0^- \right) - D_{\mathrm{V}} C_{\mathrm{V}} m_0 \beta_0^{I/V}\\
\frac{\partial m_1}{\partial t} &= D_{\mathrm{I}} \left(k\lambda_{k-1} C_{\mathrm{I}} \hat{f}_{k-1} + m_0 C_{\mathrm{I}} \gamma_1^+ - m_0 C_{\mathrm{ss}} \gamma_1^- \right) - D_{\mathrm{V}} C_{\mathrm{V}} m_0 (\Big(k-1)\beta_0^{I/V} + \gamma_1^+ \Big)\\
\frac{\partial C_{\mathrm{I}}}{\partial t} &= -\frac{\partial m_1}{\partial t} + (k-1)\frac{\partial m_0}{\partial t} - 4\pi a_0 (D_{\mathrm{I}} + D_{\mathrm{V}}) C_{\mathrm{I}} C_{\mathrm{V}}\\
\frac{\partial C_{\mathrm{V}}}{\partial t} &= -D_{\mathrm{V}} C_{\mathrm{V}} m_0 \gamma_1^+ - 4\pi a_0 (D_{\mathrm{I}} + D_{\mathrm{V}}) C_{\mathrm{I}} C_{\mathrm{V}}\\
\frac{\partial \hat{f}_{k-1}}{\partial t} &= -\frac{\partial m_0}{\partial t}
\end{aligned} \tag{4.23}$$

This set of equations along with the Eqs. 4.2 and 4.3 for sizes 2, 3, 4 of compact clusters fully describes our system.

4.4 Application to Post-implant Damage Evolution ("+N" factor calculations)

In this section, we use the model for interstitial cluster evolution described above and a vacancy clustering model from Chakravarthi and Dunham [23] for the calculation of "+N" factor. The +N factor is often defined as

$$+N = \frac{N_I - N_V}{N_{\mathrm{As}}} \tag{4.24}$$

[19], where N_I and N_{As} are the doses of interstitial and arsenic respectively.

Implant simulators (we choose UT-Marlowe [78]) may be used to simulate the damage cascade production in Si. To calculate the +N factor we applied the following recipe. We start with the "+1" model, assuming that interstitial profile is equal to the one of the dopant. Then we calculate the time-integrated interstitial supersaturation predicted by our model:

$$S_{tot} = \int_{t=0}^{t \geq end\ of\ TED} \left(\frac{C_{\mathrm{I}}}{C_{\mathrm{I}}^*} - 1 \right) dt. \tag{4.25}$$

The S_{tot} may be thought of as an enhancement to the diffusivity of boron marker layer $D_{\mathrm{B}}/D_B^* - 1$ excluding the normal diffusivity. Then we repeat calculations of S_{tot} using point defect profiles from ion implant simulator. The ratio of the two gives the +N factor:

$$+N = \frac{S_{tot}^{full\ damage}}{S_{tot}^{+1}}. \tag{4.26}$$

Fig. 4.7 shows the energy dependence of the +N factor for non-amorphizing As implants. $5 \times 10^{13}\,\mathrm{cm}^{-2}$ As^+ implantation was simulated with the UT-Marlowe [78] ion implantation simulator. The +N factor first increases with energy and then decreases. At higher energies, the separation of interstitials and vacancies is larger, leading to more pronounced and separated V-rich and I-rich region. Also the distance vacancies and interstitials need to travel to the surface is larger. This increases the probability for a vacancy to recombine with interstitial before it reaches the surface, thus reducing the number of interstitials that survive the initial recombination and reducing +N factor. We attribute the reduction in

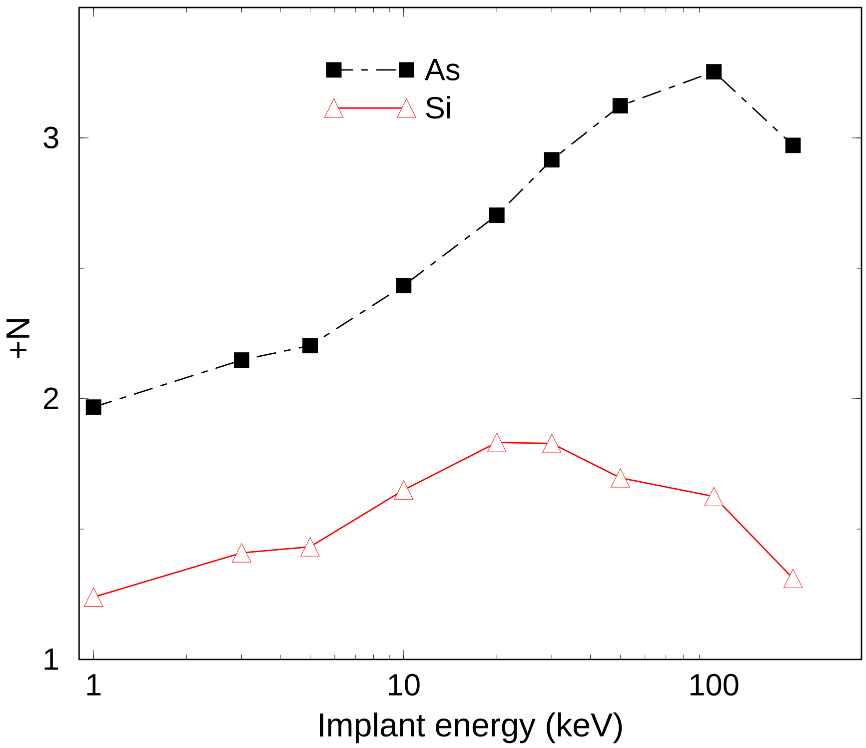

Figure 4.7: +N factor as a function of energy for non-amorphizing implant. $5 \times 10^{13}\,\mathrm{cm}^{-2}$ As and Si implantation was modeled with the UT-Marlowe [78] ion implantation simulator.

+N number at low energies to the damage cascade production simulated by BCA software (UT-Marlowe). At the low implantation energy the secondary recoils have lower energy and travel shorter distances from the vacancies, thus producing more compact damage pockets. The proximity of interstitials cause increased recombination of vacancies and reduce +N factor since fewer of vacancies can escape to the surface.

4.5 Summary

A set of discrete cluster equations was utilized to model interstitial cluster evolution after ion implantation in Si. Two independent populations of self-interstitial clusters have been considered: {311} defects and compact clusters. The system modeled the time and temperature dependence of interstitial supersaturation, as well as the size distribution during the post-implant anneal. A procedure was implemented to reduce this complex model into a simple two-moment model. The parameters for this reduced model were derived from the full rate equation model, and were found to give a good prediction of experimental data. This computationally efficient cluster/two-moment model was applied to the calculation of +N factors for Si and As.

Chapter 5

ELECTRICAL ACTIVATION/DEACTIVATION OF ARSENIC

In this chapter, different aspects of arsenic electrical activation and deactivation are discussed. We start by describing equilibrium levels of activation, then review experiments and models aimed at understanding deactivation mechanisms.

5.1 Arsenic in silicon: equilibrium level and kinetics of deactivation

Understanding and modeling arsenic deactivation requires determination of both equilibrium levels of electrical activation as well as deactivation kinetics. To determine equilibrium level of activation, electrical measurements, for example Hall measurements, may be carried out. The simplest method is to anneal isothermally until the sample reaches equilibrium. Depending on thermal history, a sample may have a transient of activation with anneal time. Equilibrium is reached when further annealing does not change the electrical activation level. This method has been used by several researchers. For instance, Hoyt *et al.* summarized electrical activation levels measured by various researches and found an Arrhenius dependence [53]. Derdour *et al.* [29] have extended measurements to a higher temperature range. They found substantial deviations from Arrhenius behavior in both high and low temperature regimes. For high temperature, it is because the deactivation kinetics is fast enough that during cooling-down the sample deactivates. At low temperatures, kinetics become so slow that practical experiments never reach equilibrium. It is difficult to determine whether actual equilibrium is reached, since the change in activation becomes very small. However it has been reported that arsenic shows strong deactivation for temperatures as low as 400°C [76].

Another aspect of equilibrium arsenic activation is how active concentration depends on total chemical concentration. Experimentally, various authors have shown that active equi-

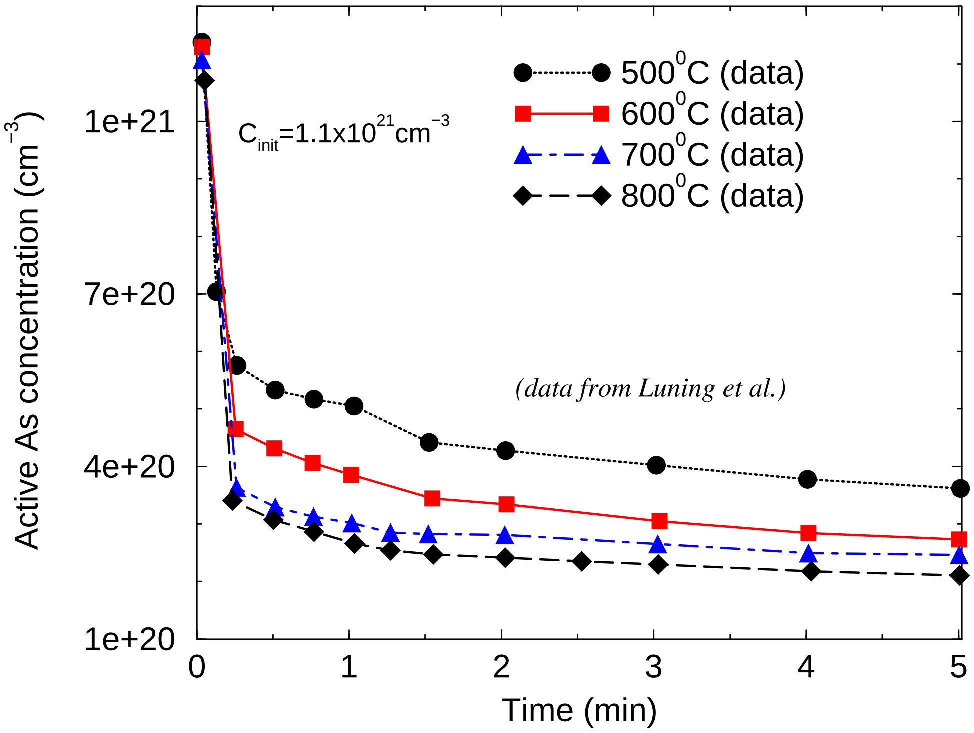

Figure 5.1: Isothermal anneal of laser annealed samples. Data from Luning [72]

librium level gradually saturates as the total chemical concentration of arsenic increases. This behavior is consistent with a clustering rather than precipitation deactivation mechanism. Although knowing the equilibrium activation is important, understanding of deactivation kinetics is necessary for modeling of arsenic deactivation.

We shall briefly review experimental observations to show important features of the kinetics of deactivation. In Fig. 5.1, results of an isothermal anneal study by Luning [72] are presented. Samples were initially fully activated by laser melt and then annealed at constant temperature. 4-point probe measurements were used to measure electrical activation, Hall measurements were used to verify the mobility. There are several key features we want to note. First, there are two clearly distinguishable phases of the process. Initial deactivation is very rapid; it happens within 15 seconds. After the initial phase, deactivation continues but on much slower scale. Although the equilibrium activation level is lower for 500°C than for 800°C, the latter shows lower activation since kinetics are faster for higher temperature.

5.2 *Literature overview*

In this section, published results are reviewed. We start with an overview of experiments aimed at understanding of arsenic deactivation and the physical mechanisms responsible. Then, the most relevant modeling efforts published prior to this work are described.

5.2.1 Experimental overview

The electrical deactivation of arsenic has been a subject of ongoing research. Both clustering [80, 84, 102, 41, 46] and precipitation [4, 76, 7] have been proposed as possible mechanisms of deactivation by various researchers. It is difficult to decide which model describes the actual phenomena since both offer good explanations for some of the experimental observations. No known criteria may hinder one from using both theories separately in different temperature/concentration regimes, or simultaneously as competing processes, or clusters being precursor for larger size precipitates.

We would like to note that in the silicon lattice arsenic atoms, being larger than Si atoms, cause local lattice expansion. Also, As having a valence of 5 needs three electron to complete the outer shell, so only three nearest neighbors are needed. These intuitive considerations help explain why arsenic in silicon deactivates and what possible inactive structures we might expect. One possibility for arsenic deactivation is formation of monoclinic SiAs precipitates. In this structure, arsenic has three nearest neighbors and silicon has four. This structure was extensively studied by Wadsten [107]. The As-Si phase diagram is presented in Fig. 5.2.

Solmi *et al.* have measured maximum concentration of As dissolved in the silicon lattice after equilibration with its conjugate SiAs phase [77]. Based on high resolution TEM measurements, they conclude that the immobile inactive phase is monoclinic SiAs precipitates, which they observe at the Si/SiO_2 interface. Only a small fraction of soluble arsenic (about 10%) is electrically active. Fig. 5.3 shows dopant and carrier profiles measured in samples heavily doped with arsenic. Solmi *et al.* have identified the solid solubility of arsenic in silicon as $C_{ss} = 1.3 \times 10^{23} \exp(-0.42/kT)\,\mathrm{cm}^{-3}$ and the limiting value of electrically active arsenic concentration being $n_e = 2.2 \times 10^{22} \exp(-0.47/kT)\,\mathrm{cm}^{-3}$ (see Fig. 5.4).

Armigliato and Parisini have found by TEM the existence of monoclinic SiAs precipitates

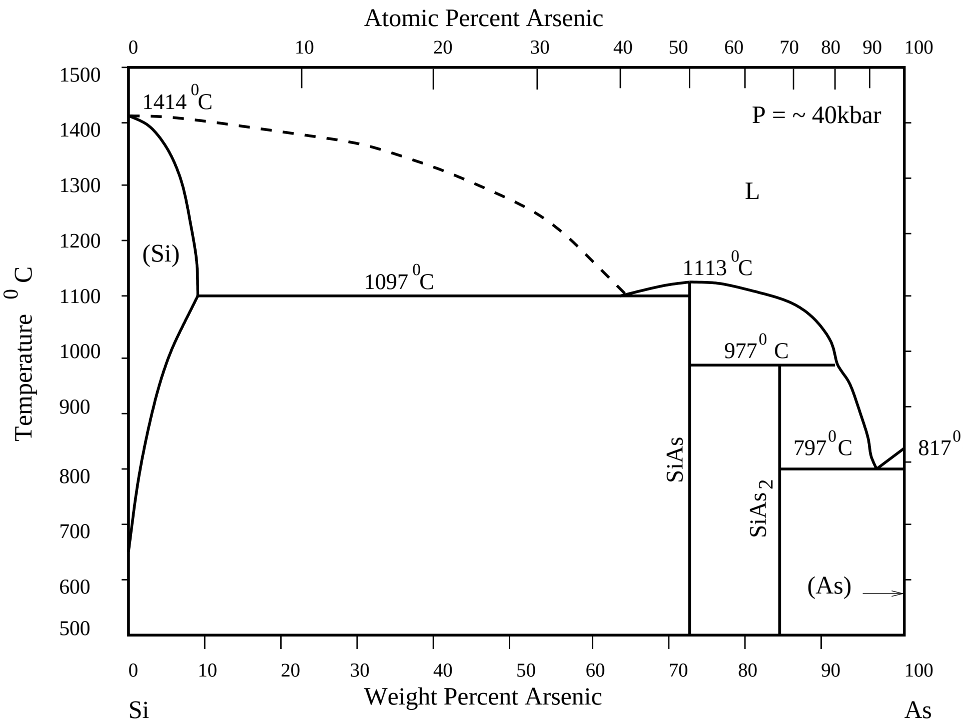

Figure 5.2: Arsenic-Silicon phase diagram [79]. At high concentrations arsenic in silicon forms a monoclinic SiAs phase.

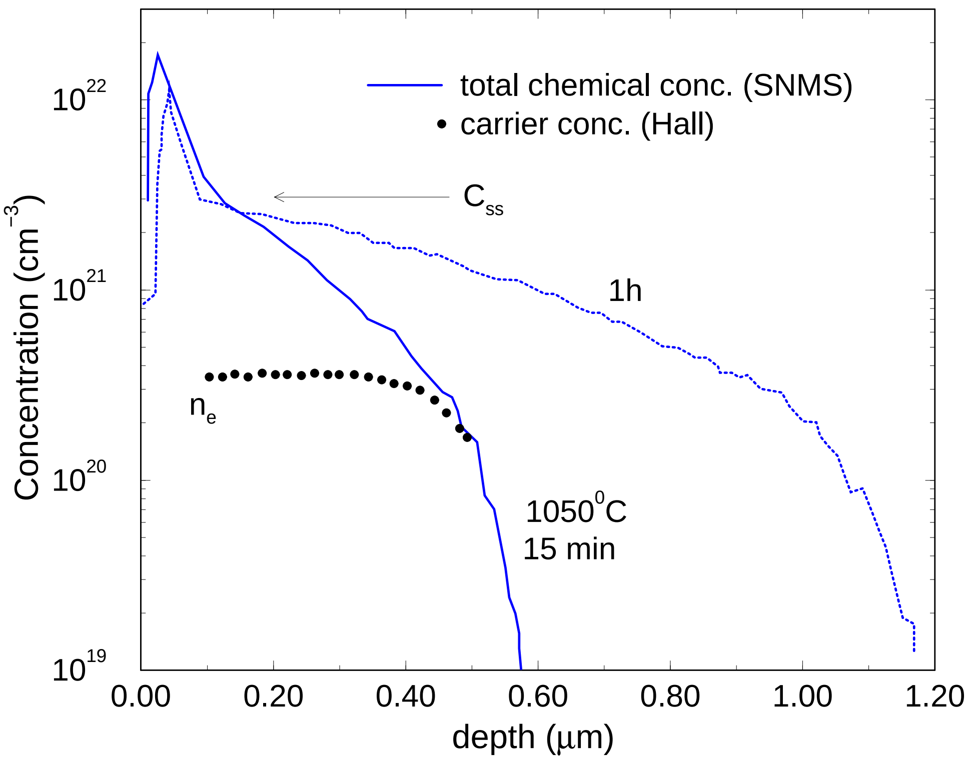

Figure 5.3: Dopant and carrier profiles measured in sample heavily doped with arsenic. The shoulder concentration in dopant profile corresponds to equilibrium between arsenic and its conjugate phase, SiAs precipitates. This value is constant with increasing anneal time and corresponds to the arsenic solid solubility value. The dotted line corresponds to the equilibrium carrier concentration, n_e, and is about 10% of total soluble fraction. Data from Solmi *et al*. [77, 96].

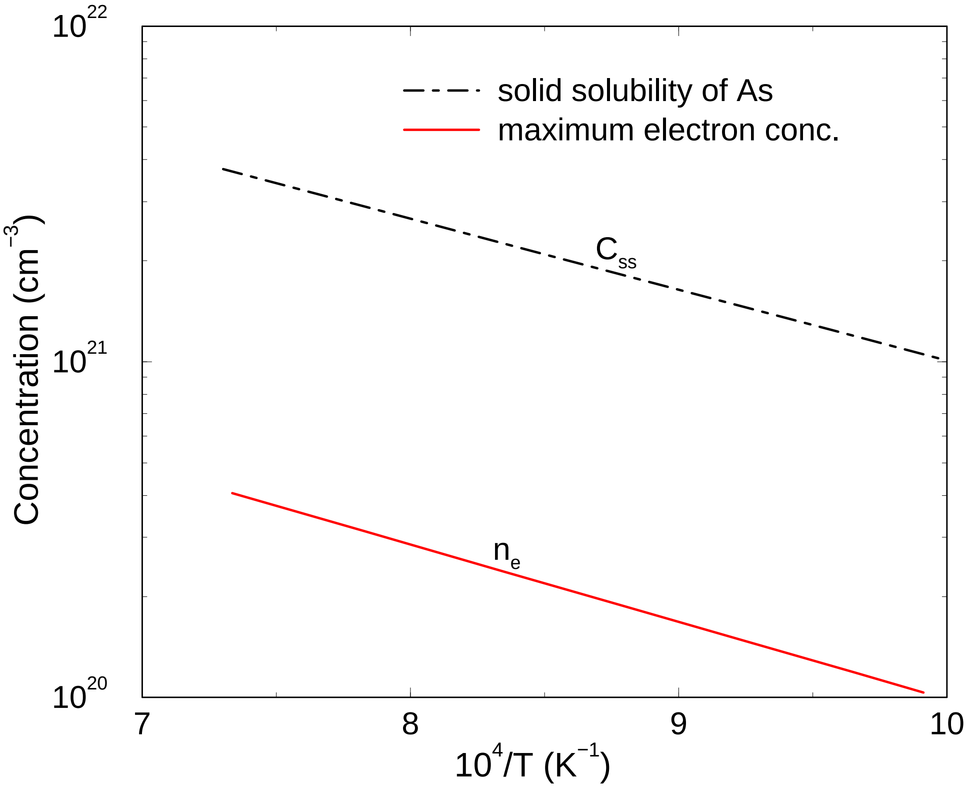

Figure 5.4: Maximum concentration of arsenic soluble in silicon lattice and maximum electron concentration, after Solmi *et al.* [77, 96].

at the Si/SiO_2 interface in heavily As-doped silicon samples and confirmed the stoichiometry by x-ray microanalysis [8]. Armigliato *et al.* showed the presence of SiAs precipitates by TEM but they did not account for all inactive arsenic even if one were to presume pure As precipitates instead of SiAs [7]. Therefore, a significant portion of inactive arsenic is still unaccounted for, even though the existence of precipitates seems probable. It is possible that smaller precipitates may form with sizes undetectable by TEM, or that clustering occurs.

Solmi and co-workers have shown that during deactivation the electron concentration exhibits a reverse annealing phenomenon [97]. This phenomenon consists of a transient increase of the carrier density taking place when a supersaturated sample, previously annealed at some temperature, is further annealed at a higher temperature with respect to which it is still in super-saturation. This behavior suggests that at least two different structures exist with different free energies. Existence of reverse annealing is a well known feature of the initial stages of precipitation [24].

The competing explanation is that clustering is responsible for electrical deactivation of arsenic. Many different types of clusters have been proposed. Tsai *et al.* have shown by simple mass action analysis that $As_3^+ +$ cluster fits equilibrium active concentration [102]. Pandey *et al.* have proposed As_4V cluster as the most energetically favorable based on *ab-initio* calculations and analysis of Extended X-ray Absorption of the Fine Structure (EXAFS) measurements [84]. There is a strong attractive interaction between arsenic and vacancies due to the combination of strain compensation and valence, which seems reasonable given that this configuration allows each valence five As to have 3 nearest neighbors and silicon atoms to have four nearest neighbors. As_2V was proposed as an initial cluster by Parisini *et al.* to explain transition from a lattice contraction of fully activated by laser melt sample to a dilatation in the deactivated sample observed by Double-Crystal X-ray Diffractometry (DCD) and the formation of interstitial loops during deactivation [85]. In their model, deactivation is described by the capture of two electrons from a pair of As atoms in the second neighbor position in the Si lattice (As_2Si), leading to the formation of a positively charged arsenic-vacancy cluster $(As_2V)^+$, and to the emission of a negatively charged silicon self-interstitial I^-:

$$As_2Si^{++} + 2e^- \Leftrightarrow As_2V^+ + I^- \tag{5.1}$$

A number of other papers have been published aimed at understanding the physical mechanisms responsible for arsenic deactivation. It was found that As-As bonding is not favored [2, 38]. Allain *et al.* performed EXAFS measurements on As heavily doped silicon after laser and subsequent thermal annealing in wide range of temperatures [2]. At low temperature (below 750°C), they proposed formation of inactive clusters involving 7 ± 4 As atoms around one vacancy, with the number of arsenic atoms around a vacancy increasing during deactivation. For higher temperatures, sphalerite precipitates and clusters might coexist in thermal equilibrium. Pandey *et al.* show deactivated arsenic with only three nearest neighbors, which seems to confirm an arsenic-vacancy cluster [84]. However, this result may also be explained by formation of monoclinic precipitates, where arsenic has only three neighbors.

Subrahmanyan *et al.* used point-defect injection experiments to provide evidence that deactivated arsenic exists as an arsenic-vacancy complex [99]. Saarinen *et al.* combined positron lifetime and electron momentum distribution measurements to investigate formation of arsenic-vacancy defects in highly As-doped silicon [93]. These complexes were identified as As_3V.

Rousseau *et al.* published a set of experimental results that suggest formation of arsenic-vacancy clusters. Generation of As_nV complexes was verified using positron-beam technique [70]. The average number of As atoms per complex was determined to be, $\bar{n} > 2$ and increasing during deactivation. Based on X-ray Standing Wave spectroscopy (XSW) measurements, they concluded that deactivated arsenic remains in coherent lattice sites even though about 85% of arsenic becomes electrically inactive [89, 51, 52]. This means that either arsenic-vacancy clusters or coherent precipitates form, ruling out arsenic-interstitial clusters, arsenic clusters in which As atoms are not in substitutional sites, or monoclinic AsSi precipitates.

Shibayama *et al.* observed diffusivity enhancement underneath high concentration arsenic layer during thermal anneal [95]. Arsenic was diffused into silicon from arseno-silicate

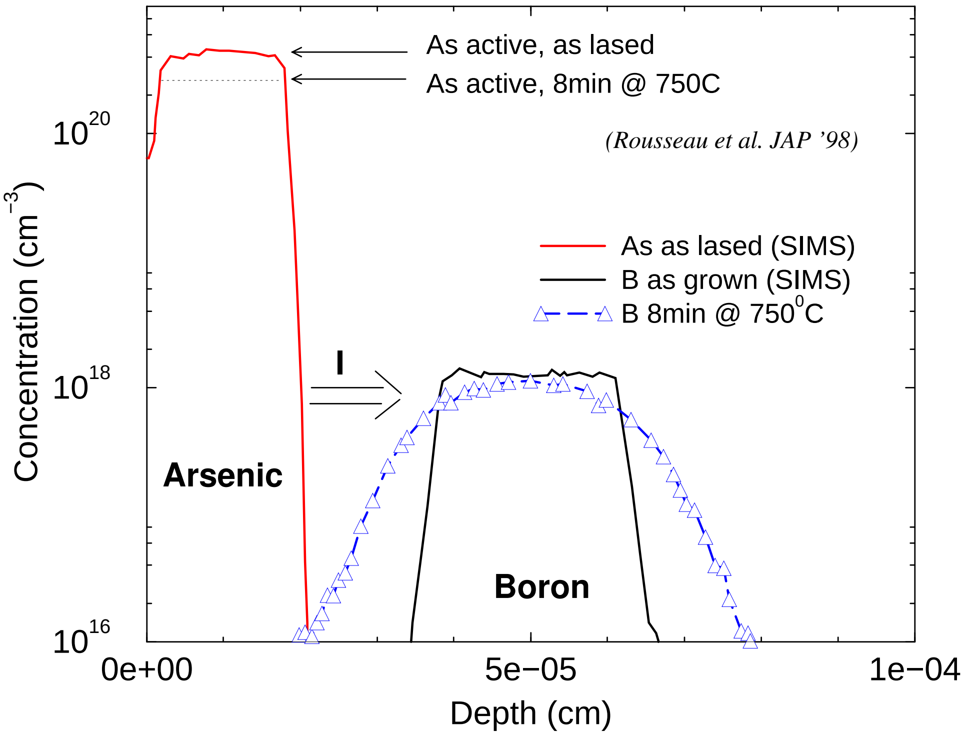

Figure 5.5: Schematic diagram representing the experimental structure used by Rousseau *et al.* [90]. During annealing arsenic layer deactivates kicking out interstitials; which enhance diffusion of buried boron marker layer.

glass at 1000°C. Enhancement of arsenic and buried boron layer was observed after 500-800°C anneal. Normally at these low temperatures dopant diffusivities are low. Boron is purely an interstitial diffuser, suggesting strong interstitial ejection from deactivated layer. It was also observed that during arsenic deactivation interstitial type defects ({311}/loops) form and grow, suggesting very strong interstitial super-saturation during arsenic deactivation [7, 85, 71, 31, 30].

We are going to describe one of the experiments by Rousseau *et al.* [90] in more detail, since we choose it for comparison with simulation results provided by our model. The model and comparison to experimental data are presented in the Chapter 6. A uniform high concentration arsenic layer was initially formed by laser melt (see Fig. 5.5). A buried boron marker layer was used to measure interstitial super-saturation. Subsequent thermal annealing at temperatures between 500°C and 750°C causes arsenic deactivation and strong diffusion enhancement of the boron marker layer for times as short as 15 sec. At this low temperature normally one does not expect to observe any noticeable diffusion. Diffusion enhancements of up to 10^5 have been measured. A study versus time demonstrates that the enhanced diffusion transient and deactivation transient are similar, indicating a strong correlation between the two phenomena. TEM studies show that a large interstitial supersaturation nucleates dislocation loops and {311} defects. Rousseau *et al.* proposed that arsenic deactivation forms small clusters of various sizes around vacancy with the injection of an associated interstitial into the bulk [90].

5.2.2 Overview of modeling efforts

In this section we are going to review the models proposed for arsenic deactivation. Guerrero *et al.* presented a generalized model for arsenic deactivation based on mass action law [49]. From the comparison to experiments they concluded that the following reaction provides the best fit to experimental data:

$$\mathrm{As}_3^{+++} + e^- \Leftrightarrow \mathrm{As}_3^{++}. \tag{5.2}$$

This model was derived based on equilibrium levels of electrical activation and did not attempt to simulate kinetics of deactivation. Dunham developed a general kinetic precipitation model (KPM) which considers the time evolution of the precipitate size density, and is able to account for various experimental observations including reverse annealing behavior [32]. Clejan and Dunham introduced an efficient moment-based model for quantitative modeling of precipitation processes [25]. Dokumaci developed a model which describes kinetics of deactivation based on formation of arsenic precipitates. The model was extended to account for dopant point-defect interaction [30], but is inconsistent with diffusion experiments and reverse annealing behavior.

Various researchers used *ab-initio* calculations to study possible mechanisms of arsenic deactivation [84, 87, 13, 12, 109]. Theoretically, Pandey *et al.* have shown that the $\mathrm{As_4V}$ cluster is the energetically favorable structure [84]. Ramamoorthy and Pantelides [87] examined $\mathrm{As_2V}$, $\mathrm{As_3V}$, $\mathrm{As_4V}$, $\mathrm{As_6V_2}$ and several other structures, but they did not consider the ionized states or the entropy. Entropy might disfavor formation of large complexes like As_4V and As_6V_2, and complete free energy calculations are therefore needed. Berding *et al.* combined *ab-initio* calculations with generalized statistical theory to determine the deactivation mechanism, including the temperature dependent electronic excitations and the entropy [13, 12]. According to these calculations, small clusters, like As_2V and As_3V, are present in significant quantities during deactivation. According to Berding *et al.*, As_2V and As_3V have acceptor states in the band gap, which should be ionized at room temperature. But recent experiment by Solmi *et al.* aimed at analysis of electron mobility change with respect to carrier concentration and total arsenic concentration demonstrated that deactivation centers (clusters or precipitates) are electrically inactive [97]. Xie and Chen have investigated As-assisted Frenkel pair generation in heavily arsenic doped silicon via first-principal total energy calculations [110]. They found that it is much easier to generate a vacancy close to substitutional arsenic atom than in pure silicon. The most energetically favorable process is described as:

$$\mathrm{As_4Si} \Rightarrow \mathrm{As_4V} + \mathrm{I}. \tag{5.3}$$

Ionized states and electron transfer during deactivation were not considered.

5.3 Conclusions

In this chapter, published results were reviewed. It has been shown that to accurately model arsenic deactivation a kinetic model is required. Therefore, the understanding of the physical mechanism of deactivation is necessary. A number of experiments imply that several small clusters are responsible for arsenic deactivation. Theoretical studies of the deactivation mechanism demonstrate that small arsenic-vacancy clusters are energetically favorable structures and might be responsible for arsenic deactivation.

Due to high computational cost of *ab-initio* calculations only structures consisting of up to 6 As atoms have been considered, while experimental techniques such as TEM usually can not detect objects smaller than several nanometers. The question is still open whether other complexes may be responsible for deactivation and what is the exact formation mechanism.

The goal of this work is to show that arsenic diffusion and electrical activation can be modeled based on the assumption that arsenic-vacancy clusters are responsible for deactivation and immobilization of the peak during diffusion. In the next chapters, we present a consistent set of models which have been successfully applied to simulation of a broad range of deactivation data as well as diffusion experiments.

Chapter 6

MODELING OF ARSENIC DEACTIVATION

In this chapter, we present our work on modeling of As deactivation. First, we describe the physical mechanism proposed for deactivation. Modeling details are given next, and simulation results are in turn compared to experimental measurements.

6.1 Introduction

As discussed in Chapter 5, a strong attractive interaction between arsenic and vacancies exists due to the combination of strain compensation and valence. Thus, the deactivation of arsenic occurs primarily via the formation of arsenic vacancy complexes. The strong binding energy between arsenic atoms and vacancies dramatically reduces the energy associated with Frenkel pair formation at sites surrounded by arsenic. *Ab-initio* calculations suggest [110] that the most energetically favorable reaction leading to deactivation is: $\mathrm{As_4Si} \rightarrow \mathrm{As_4V} + \mathrm{I}$.

We have investigated the deactivation process via a combination of *ab-initio* and continuum simulations. By including both interstitial and vacancy-mediated diffusion processes, we find it is possible to account for both the very rapid initial deactivation of arsenic, as well as the strong super-linear dependence of interstitial supersaturation on the doping level. The critical process is the rearrangement of As atoms via diffusion, leading to interstitial ejection from arsenic clusters which are favorable for vacancy incorporation.

6.2 Modeling

6.2.1 Ab-Initio Calculations

Ab-initio calculations presented in this section were performed by G. Henkelman of the University of Washington Department of Chemistry in collaboration with our efforts to understand the deactivation mechanisms. More details can be found in [35].

The energy barriers for ejection of a silicon atom from an As_4Si tetrahedral cluster were calculated via density functional theory (DFT). The minimum energy path for the process was found with the nudged elastic band (NEB) [57, 50] method. The results of the NEB calculation are shown in Fig. 6.1 and the configurations are schematically explained in Fig. 6.2. The As_4Si cluster forms a tetrahedron with a silicon atom at the center of the cluster (configuration (a)). The arsenic atoms are thought to be electronically active in this configuration [12]. During the deactivation process the central silicon atom is ejected from the cluster, becoming an interstitial (I) and leaving behind a vacancy (V). There is a small initial barrier of 0.2 eV in which the silicon atom moves from the center of the As_4 tetrahedron (a) to a stable site at the center of one of the tetrahedron faces (b). In state (b) the mobile silicon atom is still in the vicinity of the As_4 cluster, and we believe that the arsenic atoms may still be active in this configuration. From (b) to (c), the mobile silicon atom continues in the same direction away from the cluster through a tetrahedral site to a hexagonal interstitial site over a barrier of 1.4 eV. At this point the arsenic cluster is thought to be inactive as the interstitial silicon atom is removed from the cluster. The overall process is particularly interesting because the presence of the arsenic atoms allow for the creation of an interstitial vacancy pair with a barrier of 1.4 eV which is much less than the Frankel pair formation DFT barrier of more than 7 eV. Because there does not appear to be any barrier higher than the normal interstitial diffusion barrier, we consider the reverse process to be diffusion limited in the continuum simulations described below.

6.2.2 Continuum

To simulate arsenic deactivation we used discrete arsenic-vacancy clusters, assumed to be neutral [12]: $(As_2V)^0$, $(As_3V)^0$, and $(As_4V)^0$. Since clustering involves reactions of point defects and defect-dopant pairs of different charge, it is necessary to include charge transfer reactions, and simulate all possible pathways of clustering reaction. Clustering proceeds as:

$$(\mathrm{AsV})^+ + \mathrm{As}^+ \Leftrightarrow (\mathrm{As_2V})^0 + 2h^+, \tag{6.1}$$

$$(\mathrm{AsV})^0 + \mathrm{As}^+ \Leftrightarrow (\mathrm{As_2V})^0 + h^+. \tag{6.2}$$

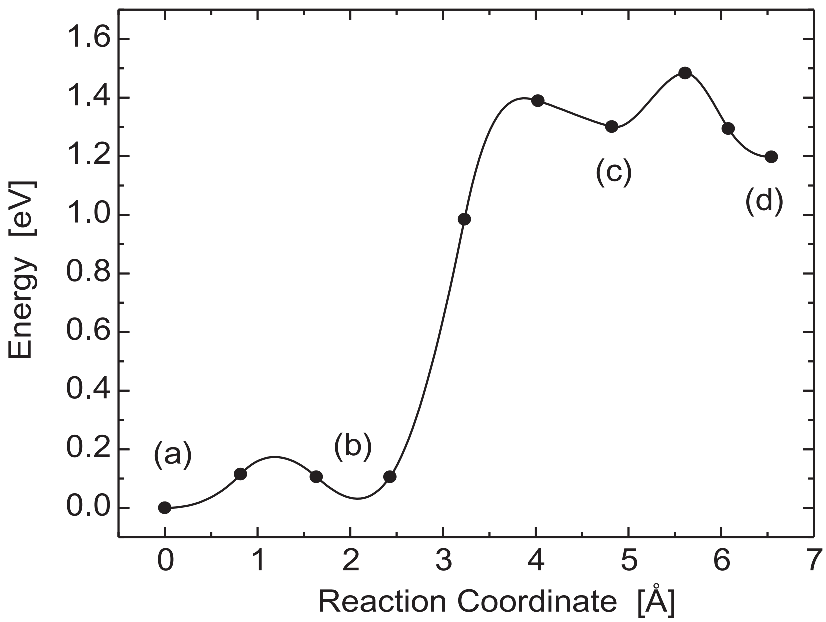

Figure 6.1: NEB calculations of the energy versus distance for kick-out of a silicon atom from between 4 substitutional As atoms [35]. The configurations are schematically explained in Fig. 6.2.

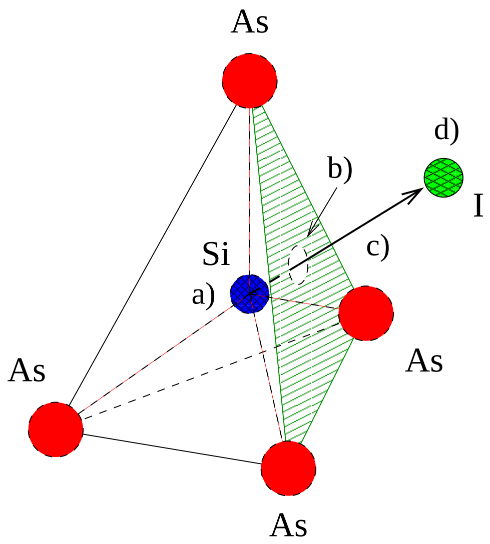

Figure 6.2: Schematic illustration of arsenic deactivation mechanism via silicon self-interstitial ejection. The silicon atom is ejected from the center of the tetrahedra (configuration a)) formed by four arsenic atoms being the second nearest neighbors. Then Si moves through the center of the face formed by the three As atoms (configuration b)) and through the the adjacent tetrahedral site (configuration c)) into the hexagonal interstitial site (configuration d)).

The reaction rates given by Eq. 6.1, and Eq. 6.2 are:

$$R_{(\mathrm{AsV})^+/\mathrm{As_2V}} = k_{(\mathrm{AsV})^+/\mathrm{As_2V}}\left[C_{(\mathrm{AsV})^+}C_{\mathrm{As}^+} - \frac{C_{\mathrm{As_2V}}}{K_{(\mathrm{AsV})^+/\mathrm{As_2V}}}\left(\frac{p}{n_i}\right)^2\right], \tag{6.3}$$

$$R_{(\mathrm{AsV})^0/\mathrm{As_2V}} = k_{(\mathrm{AsV})^0/\mathrm{As_2V}}\left[C_{(\mathrm{AsV})^0}C_{\mathrm{As}^+} - \frac{C_{\mathrm{As_2V}}}{K_{(\mathrm{AsV})^0/\mathrm{As_2V}}}\frac{p}{n_i}\right]. \tag{6.4}$$

Assuming that AsV pair diffusivities are independent of charge state (i.e., $D_{(\mathrm{AsV})^0} = D_{(\mathrm{AsV})^+}$), we can write the equilibrium constants for Eq. 6.3 and Eq. 6.4 in terms of Fermi level dependent arsenic diffusivities (D^0_{As} and D^-_{As})

$$\frac{K_{(\mathrm{AsV})^0/\mathrm{As_2V}}}{K_{(\mathrm{AsV}^+)/\mathrm{As_2V}}} = \frac{C_{(\mathrm{AsV})^+}}{C_{(\mathrm{AsV})^0}}\frac{n}{n_i} = \frac{D^0_{\mathrm{As}}}{D^-_{\mathrm{As}}}\frac{1-f^0_{\mathrm{I}}}{1-f^-_{\mathrm{I}}} \tag{6.5}$$

We assume that in heavily doped n-type material the total concentration of arsenic-vacancy pairs is given by $C_{\mathrm{AsV}} = C_{(\mathrm{AsV})^0} + C_{(\mathrm{AsV})^-}$. The total rate of formation of $\mathrm{As_2V}$ is then given by

$$R_{\mathrm{As_2V}} = k_{\mathrm{As_2V}}\left[C_{\mathrm{AsV}}C_{\mathrm{As}^+} - \frac{C_{\mathrm{As_2V}}}{K_{\mathrm{As_2V}}}\left(\frac{p}{n_i}\right)^2\left(1+\frac{D^-_{\mathrm{As}}}{D^0_{\mathrm{As}}}\left(\frac{n}{n_i}\right)\frac{1-f^-_{\mathrm{I}}}{1-f^0_{\mathrm{I}}}\right)\right]. \tag{6.6}$$

The formation of $\mathrm{As_3V}$ can proceed by these reactions:

$$(\mathrm{AsV})^0 + (\mathrm{As_2V})^0 \;\Leftrightarrow\; (\mathrm{As_3V})^0 + \mathrm{V}^0, \tag{6.7}$$

$$(\mathrm{AsV})^+ + (\mathrm{As_2V})^0 \;\Leftrightarrow\; (\mathrm{As_3V})^0 + \mathrm{V}^0 + h^+. \tag{6.8}$$

The ratio of equilibrium constants is given by

$$\frac{K_{(\mathrm{AsV})^0/\mathrm{As_3V}}}{K_{(\mathrm{AsV}^+)/\mathrm{As_3V}}} = \frac{C_{(\mathrm{AsV})^+}}{C_{(\mathrm{AsV})^0}}\frac{n}{n_i} = \frac{D^0_{\mathrm{As}}}{D^-_{\mathrm{As}}}\frac{(1-f^0_{\mathrm{I}})}{(1-f^-_{\mathrm{I}})}. \tag{6.9}$$

The total rate of formation of $\mathrm{As_3V}$ is:

$$R_{\mathrm{As_3V}} = k_{\mathrm{As_3V}}\left[C_{\mathrm{AsV}}C_{\mathrm{As_2V}} - \frac{C_{\mathrm{As_3V}}C_{\mathrm{V}^0}}{K_{\mathrm{As_3V}}}\left(\frac{p}{n_i}+\frac{D^-_{\mathrm{As}}}{D^0_{\mathrm{As}}}\frac{1-f^-_{\mathrm{I}}}{1-f^0_{\mathrm{I}}}\right)\right]. \tag{6.10}$$

Similarly, $\mathrm{As_4V}$ is formed by following reactions

$$(\mathrm{AsV})^0 + (\mathrm{As_3V})^0 \;\Leftrightarrow\; (\mathrm{As_4V})^0 + \mathrm{V}^0, \tag{6.11}$$

$$(\mathrm{AsV})^+ + (\mathrm{As_3V})^0 \;\Leftrightarrow\; (\mathrm{As_4V})^0 + \mathrm{V}^0 + h^+. \tag{6.12}$$

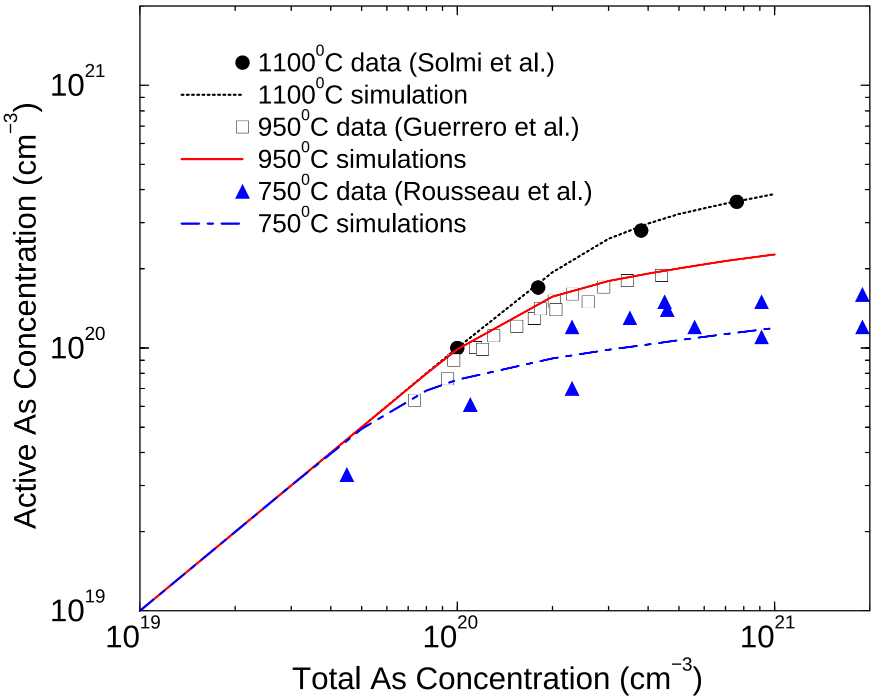

Figure 6.3: Comparison of arsenic-vacancy clustering model to experimental measurements of active versus total arsenic concentration at long times. The model was fitted to data from Solmi *et al.* [97] at 1100°C and Guerrero *et al.* [49] at 950°C and extrapolated to lower temperature. Extrapolation to 750°C temperature is compared to data from Rousseau *et al.* [90]

Total rate of reaction is

$$R_{\mathrm{As_4V}} = k_{\mathrm{As_4V}} \left[C_{\mathrm{AsV}} C_{\mathrm{As_3V}} - \frac{C_{\mathrm{As_4V}} C_{\mathrm{V^0}}}{K_{\mathrm{As_4V}}} \left(\frac{p}{n_i} + \frac{D^{-}_{\mathrm{As}}}{D^{0}_{\mathrm{As}}} \frac{1 - f^{-}_{\mathrm{I}}}{1 - f^{0}_{\mathrm{I}}} \right) \right]. \tag{6.13}$$

The binding energies of reactions were fitted to equilibrium activation levels from experimental data [97, 49]. The comparison of simulation data to experiments is plotted in Fig. 6.3.

To model interstitial ejection during As deactivation, we include arsenic-assisted Frenkel pair generation in addition to bulk generation/recombination. Since *ab-initio* calculations described in the previous section find no additional barrier beyond that required for the I to diffuse away, for I ejection reactions we simply reduce the normal Frenkel pair formation energy by the same binding energies that were found from comparison to equilibrium activation.

Deactivation proceeds as

$$(\mathrm{As_2Si})^{++} + 2\mathrm{e}^- \;\Leftrightarrow\; (\mathrm{As_2V})^0 + \mathrm{I}^0, \tag{6.14}$$

$$(\mathrm{As_3Si})^{3+} + 3\mathrm{e}^- \;\Leftrightarrow\; (\mathrm{As_3V})^0 + \mathrm{I}^0, \tag{6.15}$$

$$(\mathrm{As_4Si})^{4+} + 4\mathrm{e}^- \;\Leftrightarrow\; (\mathrm{As_4V})^0 + \mathrm{I}^0. \tag{6.16}$$

Since all reactions are similar we consider only the most significant (energetically most favorable) one, Eq. 6.16.

The initial number of $\mathrm{As_4Si}$ complexes after ion implantation and regrowth is estimated based on random distribution of dopants and the corresponding occupational probabilities,

$$C_{\mathrm{As_4Si}} = C_{\mathrm{As}}^4 \left(1 - \frac{C_{\mathrm{As}}}{C_{\mathrm{Si}}}\right) K_{\mathrm{As_4Si}}, \tag{6.17}$$

where equilibrium constant is given by

$$K_{\mathrm{As_4Si}} = \frac{1}{C_{\mathrm{Si}}^3} \exp\left(\frac{-E^f_{\mathrm{As^{4+}/Si}}}{\mathrm{kT}}\right). \tag{6.18}$$

$E^f_{\mathrm{As_4Si}}$ is the formation energy of $\mathrm{As_4Si}$ complex relative to four infinitely separated As substitutional atoms and perfect silicon crystal. During deactivation, $\mathrm{As_4Si}$ complexes are assumed to be formed by AsI pair migration, again based on random reconfiguration, and the relationship given by Eq. 6.17 is assumed to remain valid.

The reaction rate of Eq. 6.16 is given by

$$R_{\mathrm{As_4V}} = k_{\mathrm{As_4Si}} \left[\frac{C_{(\mathrm{As_4Si})^{4+}}}{K_{\mathrm{As_4Si/As_4V}}} \left(\frac{n}{n_i}\right)^4 - C_{\mathrm{I}^0} C_{(\mathrm{As_4V})^0}\right], \tag{6.19}$$

where the equilibrium constant $K_{\mathrm{As_4Si/As_4V}}$ is written in terms of the equilibrium constants of arsenic-vacancy clustering reactions (Eqs. 6.1, 6.8, and 6.12),

$$K_{\mathrm{As_4Si/As_4V}} = \frac{K_{\mathrm{As_4Si}}}{(K_{\mathrm{As^+/V^0}})^3 K_{\mathrm{As_2V}} K_{\mathrm{As_3V}} K_{\mathrm{As_4V}} C^*_{\mathrm{I}^0} C^*_{\mathrm{V}^0}}. \tag{6.20}$$

Here $K_{\mathrm{As^+/V^0}}$ is an equilibrium constant for the pairing reaction between the neutral vacancy and the substitutional arsenic atom.

The strong super-linear dependence of deactivation reaction on As concentration gives a sharp onset of deactivation as a function of As concentration. Since a large number of interstitials are released during As deactivation, a corresponding large interstitial supersaturation is present during the process. We used a moment-based {311}/loop model to account for extended defect formation [44, 33]. The parameters used in the simulations are presented in Appendix A.

6.3 Comparison to experiments

It has been observed in isothermal anneal experiments [72] that for high arsenic active concentrations initial deactivation is very rapid (within 15 seconds). After this initial deactivation, activation level is similar for all doses, and deactivation continues but on much slower time scale. At lower temperatures, the deactivation kinetics are substantially slower but show the same basic behavior. Figs. 6.4 and 6.5 shows comparison of the experimental data to our model, which shows this same behavior. We would also like to comment that the sample with the medium initial concentration ($C_{init} = 6 \times 10^{20}\,\mathrm{cm}^{-3}$) shows the highest electrical activation during the annealing process, and the model is unable to predict this behavior. We believe that the direct nucleation of small loops for the sample with the highest initial active arsenic concentration leads to lower interstitial supersaturation which reduces the reverse rate of deactivation reaction Eq. 6.19 and cause the process of deactivation via interstitial ejection to proceed faster.

It has also been observed via buried B marker layers that deactivation of high concentration arsenic layers injects interstitials into the substrate [89]. Initial rapid deactivation is due to interstitial ejection from As clusters which form due to random dopant motions. Figure 6.6 shows comparison of simulation results to experimental data of Rousseau for arsenic layers which were initially fully-activated via laser anneal.

A simple analysis was carried out to test the sensitivity of the model to parameter changes. To do this, we have changed the equilibrium constant of the reaction in Eq. 6.16 by 10%. Aas can be seen from Fig. 6.7, the change in electrical activation is significant (about 40%). In contrast, asimilar 10% change in the equilibrium constants of Eq. 6.14 and

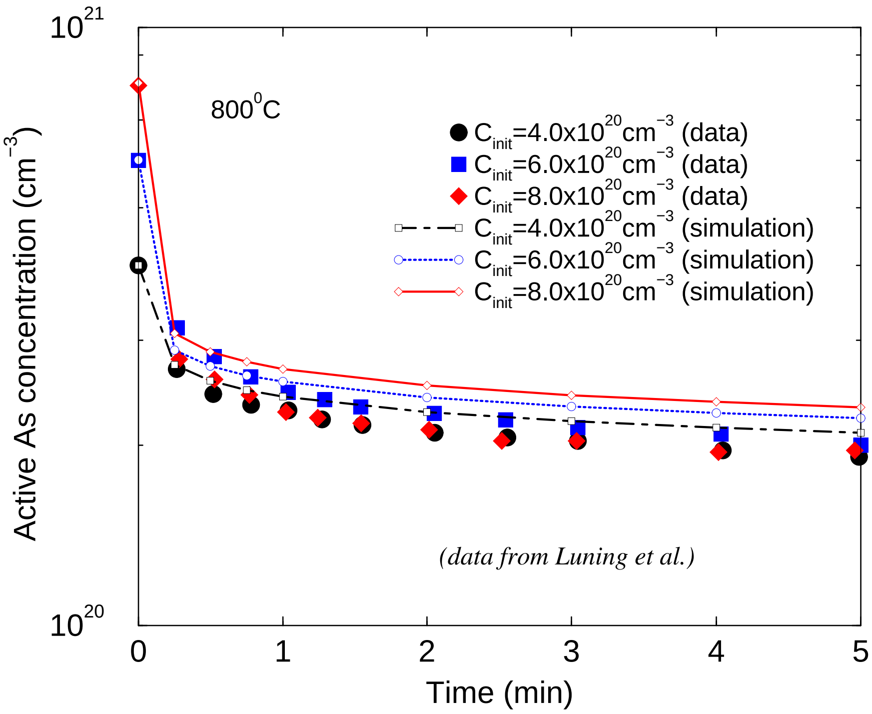

Figure 6.4: Comparison of simulation results to experimental observations of deactivation kinetics at 800°C for laser annealed As layers [72]. Note that initial deactivation is very rapid and different initial arsenic concentrations quickly reach similar activation levels. Initially the As layer was fully activated by laser melt.

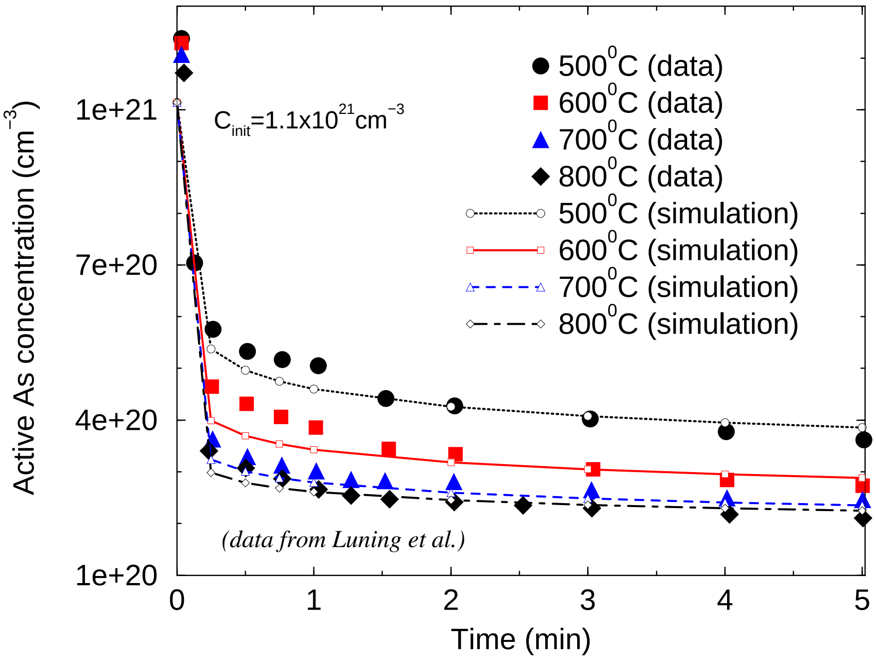

Figure 6.5: Deactivation kinetics for laser annealed As layers, with comparison of simulations to experimental data from Luning [72]. Even though equilibrium solubility is higher for higher T, initial deactivation is limited by kinetics, so the lower T anneals give higher active concentrations.

Eq. 6.15 does not change the final result noticeably since Eq. 6.16 represents the dominant mechanism of deactivation at low temperature and short times.

6.4 Conclusions

We utilized the combination of *ab-initio* calculations and continuum modeling to gain an understanding of arsenic activation/deactivation. The results highlighted the importance of ejection of silicon atoms from arsenic clusters. The barrier for Frenkel pair generation is reduced by the strong binding of vacancies to As clusters. We find it is possible to account for both the rapid initial deactivation of arsenic and the strong super-linear dependence of interstitial supersaturation on doping level, which accompanies deactivation.

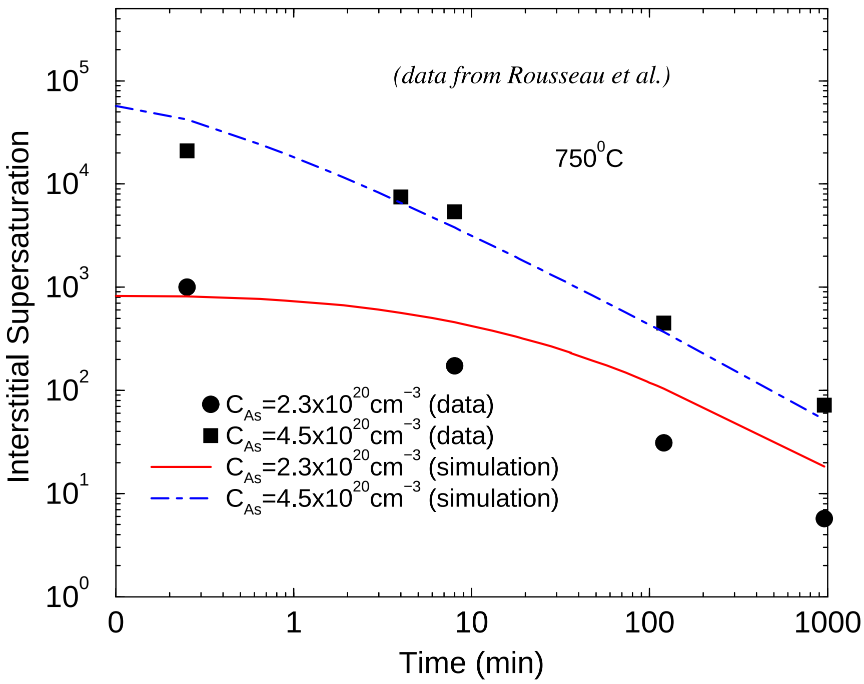

Figure 6.6: Comparison of simulation results to experimental observations of interstitial supersaturation versus time for different arsenic concentrations, measured via buried marker layer [90]. Note order of magnitude difference in supersaturation with factor of 2 change in initial As concentration.

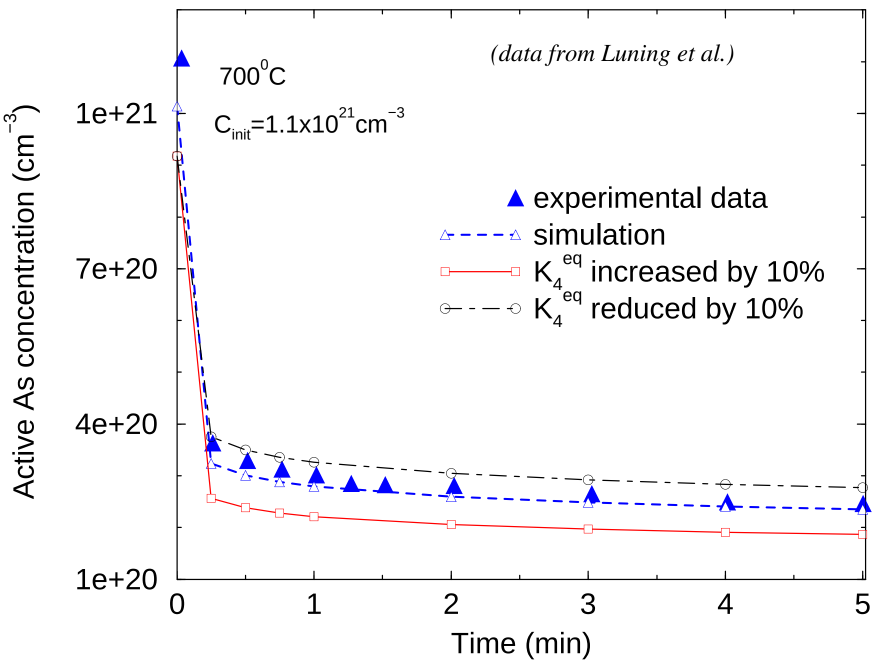

Figure 6.7: The illustration of the sensitivity of the model to the parameter change. We have changed the value of the equilibrium constant $K_{\mathrm{As_4Si}}$ by 10% to explore the sensitivity to the parameter changes. These changes lead to significant deviation in electrical activation level.

Chapter 7

MODELING OF ULTRA-SHALLOW JUNCTION FORMATION

In this chapter, the modeling of ultra-shallow arsenic junction formation is presented. We start by discussing long time diffusion of As at very high concentrations, for which neither initial damage nor TED nor interface segregation are significant. After the model for bulk arsenic diffusion at a very high concentration (the model is written in a form of a correction term to diffusion coefficient) is parameterized, we proceed to the modeling of shallow arsenic implant annealing. The essential features of a model are the initial point-defect distribution following regrowth, TED, ramp rate effects, and the high concentration diffusion correction. The model presented in this chapter takes into account these effects and produces results that are in a good agreement with chemical profiles (SIMS) as well as the electrical activation data.

7.1 Introduction

Modern device junctions are characterized by low resistivity and shallow depth. According to the International Technology Road-Map for Semiconductors [1], it is necessary to produce highly activated abrupt shallow junctions to continue device down-scaling. For instance, for 100nm technology expected in year 2005, the source/drain extensions should have sub-35nm junction depth, with the resistivity as low as 200Ω/sq. To form junctions with these specifications, ultra-low energies for ion implantation and high temperature RTP (rapid thermal processing) equipment is required to minimize dopant diffusion. In this chapter, we present a model capable of simulating ultra-shallow junction formation applicable to future generation devices.

7.1.1 Why Good Fit Produces Poor Results?

We begin by showing a comparison of a simple model to experimental data from Jain [54]. In Chapter 5, we have shown that for arsenic two solubility levels have been reported [77]:

- $C_{ppt} = 1.3 \times 10^{23} \exp(-0.42/kT)\,\mathrm{cm}^{-3}$, which is the chemical solid solubility of arsenic in silicon Above this limit As precipitates into SiAs monoclinic phase.

- $n_e = 2.2 \times 10^{22} \exp(-0.47/kT)\,\mathrm{cm}^{-3}$, which is the limiting value of electrically active arsenic concentration.

We use a five stream diffusion model [92] with a simple solid solubility model to account for the immobile portion of the profile, with the value of arsenic solid solubility (C_{ss}) being set to both values (C_{ppt} and n_e). Fig. 7.1 shows a comparison of the simulation to the SIMS data. Setting C_{ss} to C_{ppt} results in a high solubility level (about $3 \times 10^{21}\,\mathrm{cm}^{-3}$ at 1050°C) leading to complete dissolution of precipitates and as a consequence an over-estimation of diffusion. In the case of $C_{ss} = n_e$ the solubility is low (about $3 \times 10^{20}\,\mathrm{cm}^{-3}$ at 1050°C) so only a very small portion of the profile is available for diffusion which results in a significant under-estimation of diffusion depth. We were able to obtain a good match to the data with a simple solid solubility model by changing the C_{ss} value (denote as "solubility fit" on the plot) between C_{ppt} and n_e.

To calculate the resistivity of the arsenic layer, we use the electrical mobility model by Rousseau *et al.* [91] specifically derived for high concentration arsenic layers (the modeling of electrical properties are discussed in more detail in Section 7.4.2). The comparison of the simulation to the experimental results is presented in the second column of Table 7.1. The fit of the solubility level results in a lower resistivity even though the chemical profiles match well. This leads us to the conclusion that the apparent mobility suggested by chemical data (SIMS) does not correspond to the active fraction of arsenic and more careful analysis is required for accurate modeling of chemical and electrical properties of arsenic profiles.

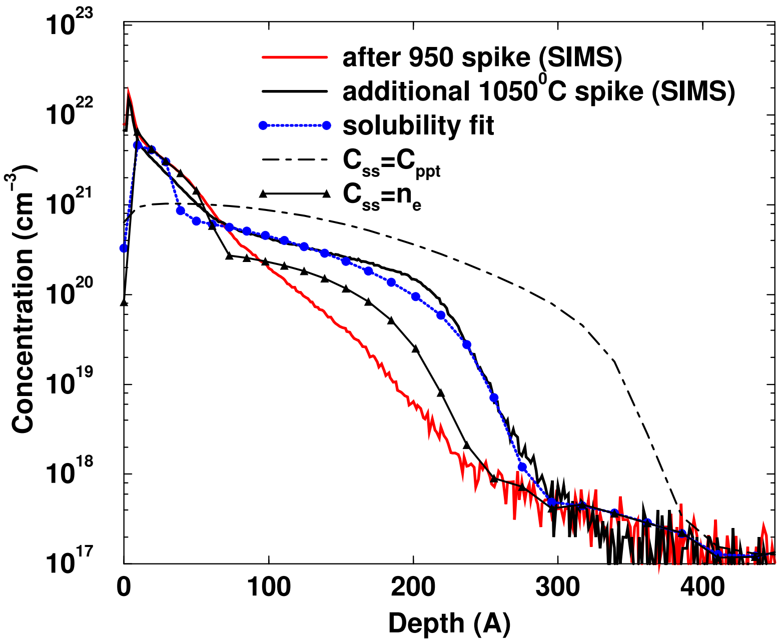

Figure 7.1: Comparison of a simple solid solubility model to the experimental data for 2×10^{15} cm^{-2} 5 keV As^{+} implant for 1050°C spike anneal following 950°C spike. Data from Jain [54].

Table 7.1: Sheet resistances of shallow arsenic junctions obtained by 5 keV and 2 keV As^+ implantation. Comparison of model to experiment. All parameters are in units of Ω/sq. Experimental data from Jain [54] presented in the first column. Result of our simulations are shown in the third column and will be discussed later in Section 7.4.2. Simulations were carried out to produce numbers in the second column to confirm the difference between the electrical solubility level and the apparent mobility (and presented in more details in Section 7.1.1). We used five-stream diffusion model with a simple solid solubility model. The solid solubility has been selected to fit shoulder of the arsenic profile (see Fig. 7.1). Despite a good match to the chemical experimental data, this method results in active arsenic concentration being higher than what our model predicts and significantly lower resistivities than observed in experiments.

	Experimental data [54]	Fit of C_{SS}	Our model
2×10^{15} cm^{-2} As^+ at 5 keV	316	232	298
1.6×10^{15} cm^{-2} As^+ at 2 keV	339	260	334

7.1.2 Outline

This chapter is organized in a “step-by-step” manner. After experimental data is presented and the problem with the conventional model is demonstrated, we correct the model and show the comparison to experiment. Then we select new data and focus on another problem with the modeling. In section 7.5, we review the essential effects included in the model and discuss other possible alternative explanations.

First, we would like to concentrate on the analysis of As diffusion at high concentrations annealed for a long time and after that switch to the modeling of short time diffusion of shallow As profiles. By doing this two stage analysis we expect to be able to separate the effects important at long time anneals (“stationary” behavior such as bulk diffusion coefficient at high concentration) from TED and deactivation effects.

7.2 Modeling of "Equilibrium" Diffusion of Arsenic at High Concentrations

7.2.1 Experiment Overview

For our simulation we have chosen data from Solmi *et al.* [77, 96]. These experiments were specifically targeted at the determination of As diffusivity at very high concentrations. In the experiments, arsenic was implanted at a dose of 1.5×10^{17} cm^{-2}. The implantation was performed in two steps in order to increase dopant concentration near the surface: first 1×10^{17} cm^{-2} As was implanted at 100 keV, followed by 5×10^{16} cm^{-2} at 50 keV. Samples were furnace annealed at 1050°C for different times between 15 min and 4 hours. Profiles were measured by Secondary Neutral Mass Spectroscopy (SNMS).

We find that the commonly used five stream diffusion model [92] together with a solid solubility model for arsenic aggregation is unable to match the experimental data (see Fig 7.2). We attribute the difficulty with fitting experimental profiles to the error in arsenic diffusion coefficient at high concentration as well as to the assumption regarding mobile fraction of the profile.

7.2.2 The Theory of High Concentration Diffusion

In order to model high concentration diffusion accurately, we first turn to an earlier experiment by Nylandsted Larsen *et al.* [69], who has clearly showed a sharp increase in arsenic diffusivity for donor concentrations exceeding 2×10^{20} cm^{-3}. Dunham and Wu [36] proposed a theoretical model based on results of Kinetic Lattice Monte-Carlo (KLMC) simulations to explain this behavior. They assumed a simple additive potential for As-V interaction up to the third nearest neighbor and showed that at very high doping levels a vacancy is likely to interact with more then one dopant at a time. These multiple interactions effectively reduce activation energy for pair diffusion, thereby increasing the dopant diffusivity. Dunham and Wu found that the correction to arsenic diffusivity via vacancies at high doping levels has a power dependence on active arsenic concentration, C_{As}, and may be written in the form:

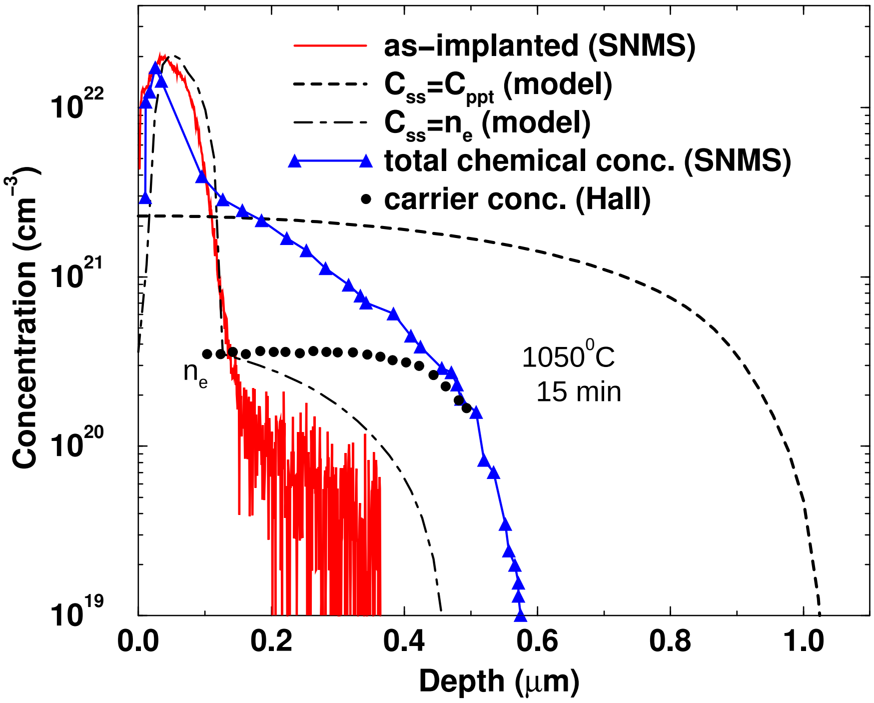

Figure 7.2: Comparison of a simple solid solubility model to the experimental data from Solmi *et al*. [96]. First, the solid solubility, $C_{ss} = C_{ppt}$ is set to the chemical solubility of arsenic in silicon (dashed line). The entire peak region dissolves and causes over-estimation of diffusion. In the second case, the solubility is set to the limit of electrical activation of arsenic in silicon, $C_{ss} = n_e$ (dot-dashed line). Most of the profile stays immobile and not enough arsenic is available for diffusion, resulting in the under-estimation of diffusion depth. Solid line with triangles represents experimentally measured by SNMS chemical profile after 1050°C anneal for 15 min, solid circles - electrically active portion, obtained by differential Hall measurements. We were unable to match experimental data by changing the C_{ss} parameter.

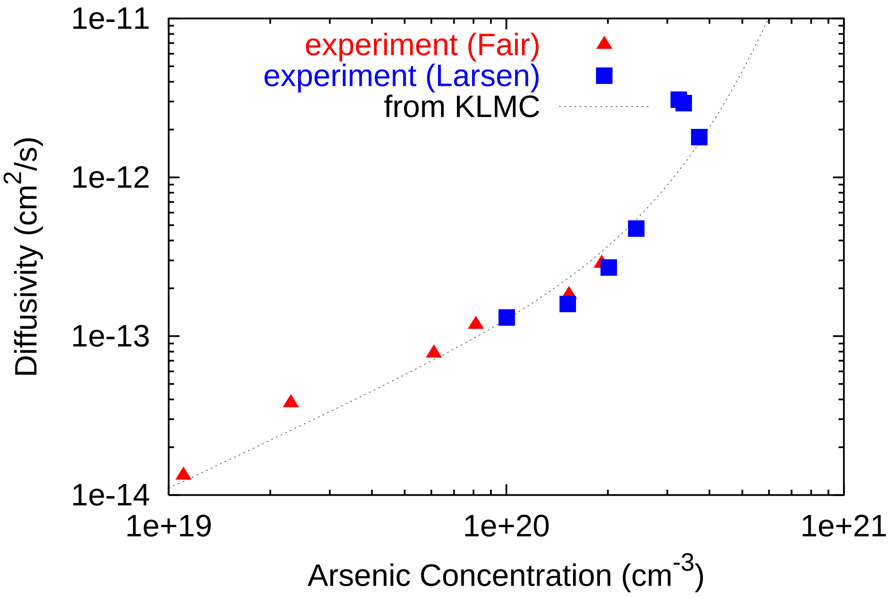

Figure 7.3: Arsenic diffusivity at a high doping level at 1050°C. Data from Larsen *et al.* [69] and Fair [40]. Note the sharp increase in arsenic diffusivity for donor concentrations exceeding 2×10^{20} cm^{-3}, which is accurately predicted by KLMC simulations by Dunham and Wu [36].

$$D_{\mathrm{As}}^{V} = \left(\frac{C_V}{C_V^*}\right)(1 - f_I)D_{\mathrm{As}}^{-}\left(\frac{n}{n_i}\right)\left[1 + \left(\frac{\mathrm{C_{As}}}{\mathrm{C_{ref}}}\right)^{\alpha}\right], \tag{7.1}$$

with $\alpha = 3\text{–}4$. As shown in Fig. 7.3, simulations accurately predict rapid increase in diffusivity above 2×10^{20} cm^{-3}.

More recent *ab-initio* calculations [109] confirm that the range of interaction between an AsV pair and another As extends up to at least the ninth nearest neighbor site (the third nearest neighbor site of one arsenic is the second nearest neighbor site of another As at site 9). The migration barrier is significantly lower in the case when another As occupies fifth, sixth or ninth nearest neighbor site resulting in enhanced diffusion at high arsenic concentrations. Fig. 7.4 is a schematic illustration of the barrier lowering in the presence of another As atom.

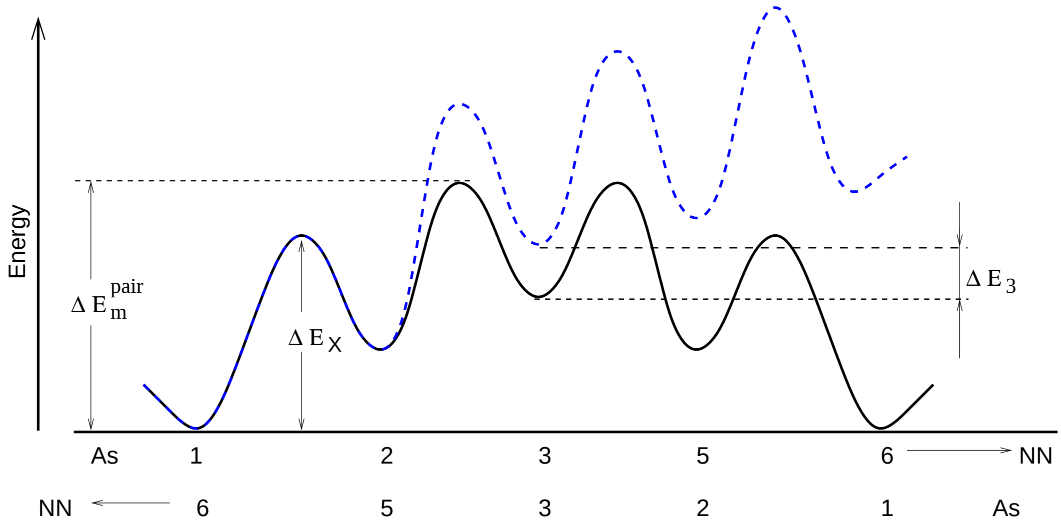

Figure 7.4: Illustration of diffusion barrier lowering in a presence of another As atom at the ninth nearest neighbor site. The energy diagram for As-V as a function of As-V separation with (solid line) and without (dashed line) another As atom at the sixth neighbor site. The forth and seventh neighbors are along a different path and therefore not shown.

7.2.3 Modeling of Long Time Arsenic Diffusion

To separate transient enhanced diffusion and the effect of initial conditions from the bulk arsenic diffusivity at high doping levels, we use the experimentally measured SNMS profile after 15 min as the initial condition for modeling of arsenic diffusion for longer times. Solmi *et al.* also reported the carrier concentration measured by differential Hall technique. We assume that carrier concentration profile corresponds to active arsenic while the rest of the profile represents inactive immobile clusters.

Fig. 7.5 shows a comparison of our simulation to experimental profiles from Solmi *et al.* In the simulations, parameters C_{ref} and α are considered as a free fitting parameters and the best fit is obtained with $C_{ref} = 1.6{\times}10^{20}$ cm^{-3}, and $\alpha = 4.0$. These values are close to the KLMC predictions by Dunham and Wu [36], who found that the onset of a sharp increase in diffusivity is at about 2×10^{20} cm^{-3} and at higher concentrations diffusivity depends on the 3rd to 4th power of (C_{As}/C_{ref}). Hence we are going to use this model with these parameters for simulation of shallow As implants annealing presented in the next sections.

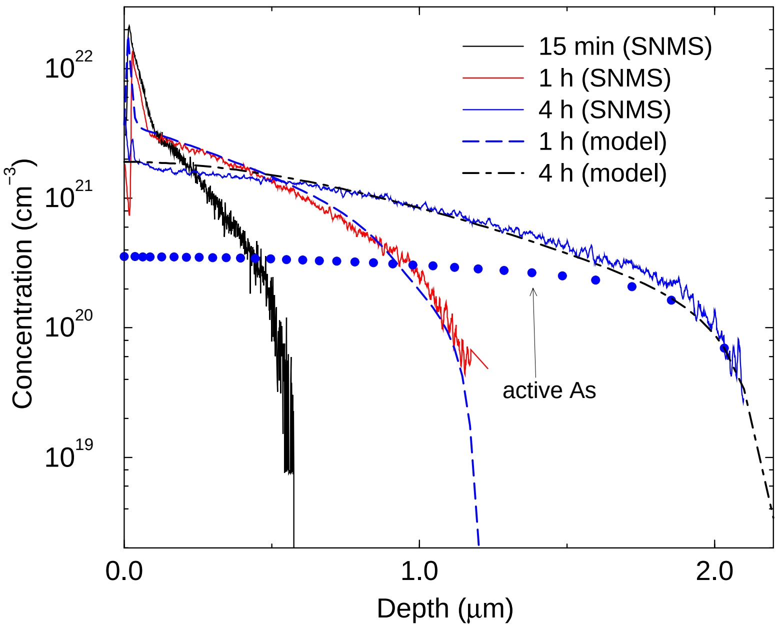

Figure 7.5: Comparison of simulation to annealing results from Solmi *et al.* [96]. SNMS profile after 15 min anneal is used as starting point of simulation. The best fit is obtained with $C_{ref} = 1.6 \times 10^{20}$ cm^{-3} and $\alpha = 4.0$.

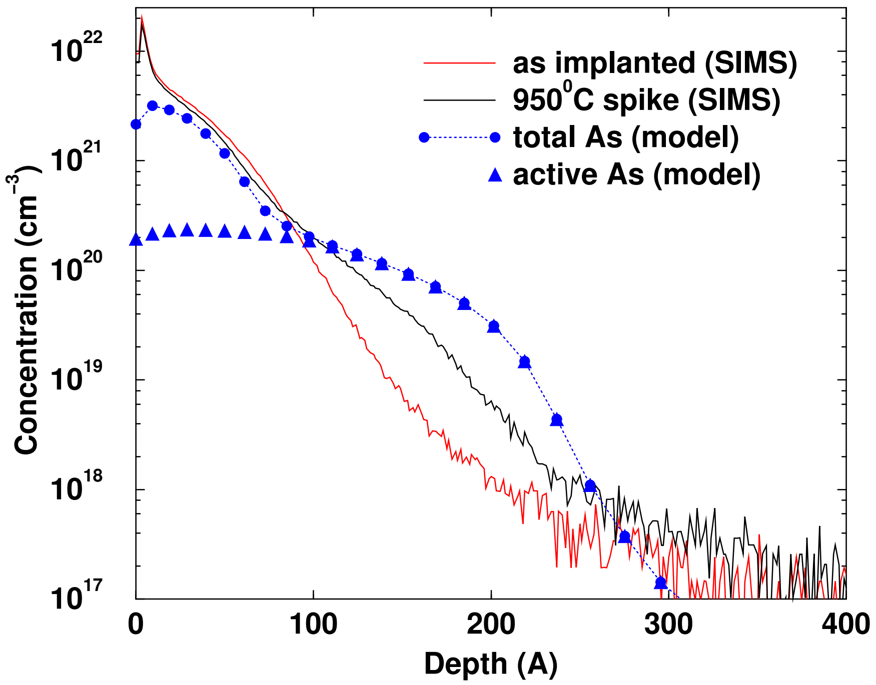

Figure 7.6: Simulation of 950°C spike anneal. Strong interstitial ejection due to arsenic deactivation enhances diffusion and leads to substantial over-estimation of diffusion.

7.3 Shallow As Implant Anneal

We compare our model to spike annealing results from Jain [54]. In these experiments, 2×10^{15} cm^{-2} As was implanted at 5 keV through 53 Å of silicon dioxide and 1.6×10^{15} cm^{-2} As was implanted at 2 keV through 20 Å of SiO_2. Both samples were annealed at 950°C and 1050°C via spike anneal with ramp-up rates of 100°C/sec. Shown in Figure 7.6 is comparison of a simulation using the high concentration diffusion model discussed in the previous section with the As deactivation model from Chapter 6 to SIMS profile from Jain [54]. We can see that model substantially overestimates diffusion due to strong interstitial ejection during As deactivation during the ramp-up.

Since the overall thermal budget is relatively low in the case of fast spike anneal, the diffusion capacity of vacancies from the surface is not sufficient to account for deactivation of arsenic peak. Clustering via silicon self-interstitial kick-out mechanism, which is described in Chapter 6, seems the only other reasonable deactivation option but produces one interstitial for every four deactivated arsenic atoms, thus creating a large interstitial population with dose comparable to that of implanted arsenic. These interstitials lead to enhanced diffusion and significant over-estimation of the profile depth in contrast with experimental observations. To solve this inconsistency we examine several possible explanations in the following section.

7.3.1 Arsenic-Interstitial Clusters

Jones and co-workers carried out several experiments [56, 18, 68] to determine the properties of arsenic-interstitial clusters and whether arsenic-interstitial clusters form under ion implantation conditions. Using TEM they show that the number of interstitials bounded to {311} defects decreases with increasing arsenic well concentration and that the ratio of interstitials "missing" from {311} defects to background arsenic concentration suggests As_2I clustering [18]. In another experiment Jones *et al.* [56] showed that for low energy implants (3-5 keV) TED is very similar and is independent of implant energy while no extended defects were observed in the EOR region as implant energy decreases from 5 keV to 3 keV. The authors speculate that this behavior may be explained by arsenic-interstitial cluster formation. Kim *et al.* studied arsenic TED in silicon with and without additional self-implantation [62]. The experimental results show the suppression of As diffusion with additional self-implantation during initial stage of annealing, in contrast to the prediction of conventional models. They suggest that results may be explained by the formation of As-I clusters during initial stages of annealing.

To determine the importance of arsenic-interstitial complexes for low energy As implant annealing modeling, we investigated the stability of these clusters via *ab-initio* calculations. *Ab-initio* calculations presented in this subsection were performed by M. Diebel of the University of Washington Physics Department. The total energy calculations for arsenic-interstitial cluster were carried out via density functional theory (DFT). The DFT calculations were done with the VASP [66, 67, 64, 65] code using the PW91 functional [86] and ultra-soft pseudo-potentials [106]. Plane waves up to a 300 eV energy cutoff were used

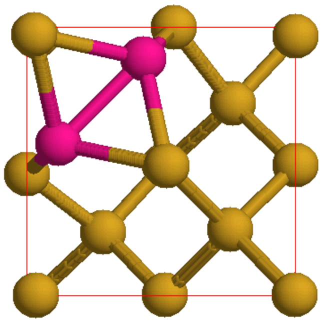

Figure 7.7: Atomic structure of As_2I split cluster. Dark circles represent As atoms.

to represent the wavefunction in the unit cell. The calculations were done with eight points in the k-point mesh. The computational cell consisted of 64 atoms.

To find the lowest energy configuration, we searched through a set of different structures containing up to 8 As atoms. The binding energy of AsI pair was found to be 0.3eV. The most stable structure identified was an As_2I split <110> cluster with binding energy 1.5eV with respect to neutral arsenic and neutral interstitial. Figure 7.7 shows the atomic structure of this cluster.

Including an As_2I cluster in the continuum simulation helps immobilize interstitials at low temperature but has a very small overall effect on the junction depth, because the As_2I structure is less energetically favorable then {311} defects. Our analysis shows that the binding energy of an As_2I cluster needs to be about 4eV to significantly reduce As diffusion and this is in clear contradiction with first principle calculations. Also, a higher binding energy would result in a noticeable fraction of arsenic being in a form of As_2I clusters and this contradicts the backscattering experiments by Grob *et al.* [48] who found that most of the arsenic remain substitutional after epitaxial regrowth and subsequent RTP treatment.

7.3.2 Grown-in Vacancies after Amorphous Region Recrystallization

We suggest another effect responsible for elimination of interstitial excess which provides a simple solution to the inconsistency between our model and experiments. The idea is based on indirect experimental observations. Krishnamoorthy *et al.* studied extended defects in high dose low energy As implanted silicon formed during TED and arsenic deactivation [68]. Authors found that with increasing arsenic peak concentration above 1×10^{21} cm^{-3}, the number of {311} defects and loops formed during As deactivation decreases. *Ab-initio* [87, 12] calculations have found that $\mathrm{As}_n\mathrm{V}$ clusters are energetically much more favorable than isolated vacancies. This suggests that high As concentrations may stabilize the incorporation of vacancies.

We assume that during SPE regrowth, a lattice site which has at least two arsenic nearest neighbors (NN), has a probability (η) of turning into a vacant site. Since the energy gain of combining two arsenic atoms with a vacancy almost compensate the formation energy of vacancy defect we expect the probability η to be close to 1. Based on the geometry of the Si lattice (12 2^{nd} NN) the concentration of $\mathrm{As_2V}$ complexes formed after SPE regrowth is given by:

$$C_{\mathrm{As_2V}} = \left[1 - \left(1 - \eta \frac{C_{\mathrm{As}}}{C_{\mathrm{Si}}}\right)^{12}\right] \frac{C_{\mathrm{As}}}{2} \tag{7.2}$$

PAS experiments [70] reported that substantial vacancy population has been found in laser annealed samples right after laser melt but before any deactivation anneal took place, thus supporting our assumption.

7.4 Simulation of Low Energy Implants Diffusion

7.4.1 Chemical Profile

To simulate low energy As implant diffusion, we use the five stream diffusion model described in Section 2.1.2 including rapid diffusion via vacancies at high doping levels discussed above. For arsenic diffusivity, we use parameters from Wittel [108]. To account for immobile electrically inactive arsenic, the model described in Chapter 6 is used. Bulk point defect diffusivity/equilibrium concentration products (e.g., $D_{\mathrm{I}}C_{\mathrm{I}}^*$) are from isotope self-diffusion experiments [104] with diffusivities taken from MD calculations [101, 55]. We used a moment-based {311}/loop model [44] to account for extended defect formation.

UT-MARLOWE [78] is used to obtain initial interstitial profile and estimate the depth of amorphous/crystalline interface. The initial concentration of As_2V clusters is calculated using Eq. 7.2. Shallow arsenic SIMS profiles might have an artificial pile-up near the surface [94] which results in integrated dose under the SIMS profile being larger than the actual implanted dose. Instead of SIMS we use UT-MARLOWE [78] simulated profiles (which closely match SIMS except in the interface transient region) as the initial arsenic distribution.

Simulations include linear ramp-up with a rate of 100°C/sec. After the wafer reaches designated temperature and RTP furnace is switched off, it is assumed that the wafer temperature drops solely by radiating heat to the furnace walls and therefore ramp-down rate decreases with decreasing temperature. The heat loss is proportional to T^4, hence temperature versus time may be written in a form [21]:

$$T(t) = T_f \left(\frac{1 - 3tR_{cool}}{T_f} \right)^{-0.33} \tag{7.3}$$

where T_f is the maximum attained temperature, R_{cool} is the cooling rate (°C/sec) at maximum temperature (T_f) and t is time after reaching T_f.

Figs. 7.9 - 7.11 show comparison to RTP anneals from Jain [54] for two different implant energies. The simulations give a good match to the observed arsenic junction depth.

7.4.2 Electrical Activation Data

We also compared our model to the electrical data from Jain [54]. We use the mobility model from Rousseau *et al.* [91] specifically fitted for high concentration arsenic layers. The electron mobility depends on both active arsenic concentration (scattering from ionized impurity) and inactive cluster concentration (scattering from neutral defects). The comparison of experimental data to resistivity calculated based on diffusion profiles from our model is presented in Table 7.1. Here we assume that As_2V, As_3V, and As_4V clusters are electrically neutral at room temperature and contribute only to the mobility due to inactive impurities, while free arsenic is active and electron concentration is equal to arsenic concentration.

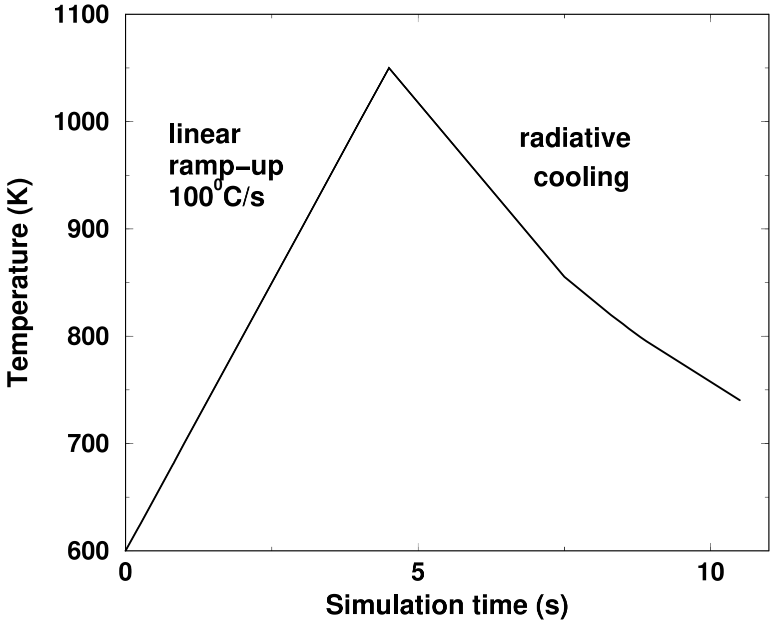

Figure 7.8: Temperature versus time used for simulation. Ramp-up is modeled as linear, while cool down is radiative.

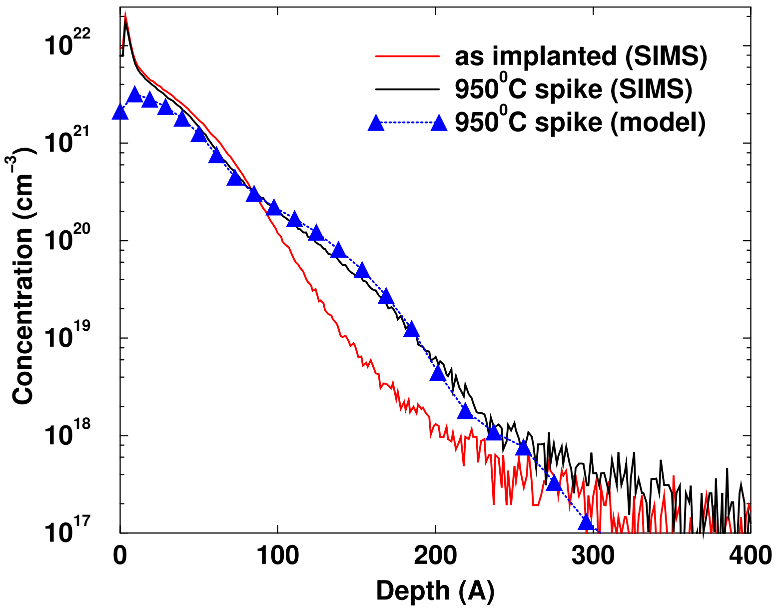

Figure 7.9: Comparison of simulation and experiment for 2×10^{15} cm^{-2} 5 keV As^{+} implant for 950°C spike anneal. Data from Jain [54].

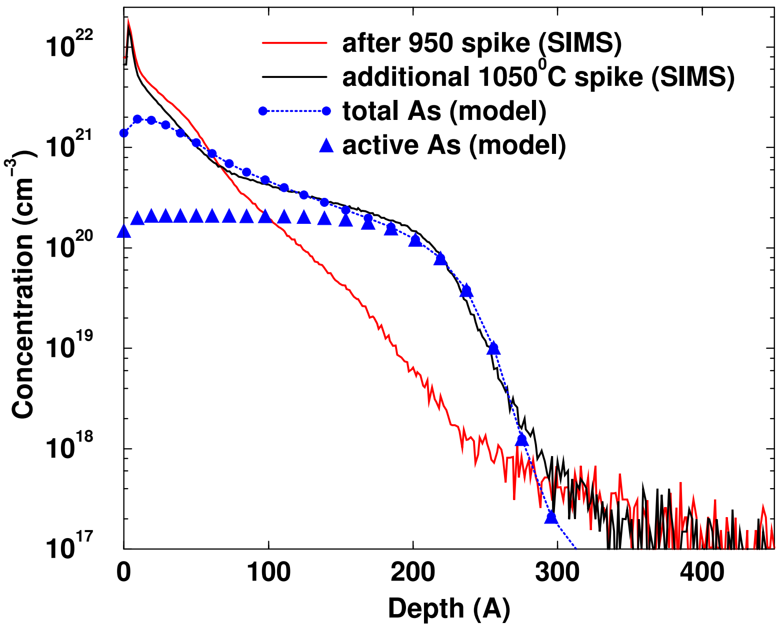

Figure 7.10: Comparison of simulation and experiment for 2×10^{15} cm^{-2} 5 keV As$^+$ implant for 1050°C spike anneal following 950°C spike (Fig. 7.9). Data from Jain [54].

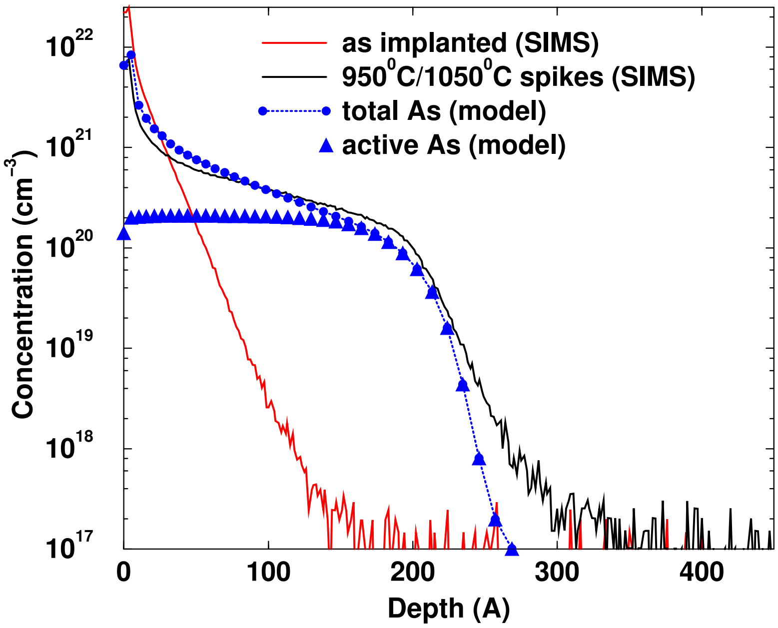

Figure 7.11: Comparison of simulation and experiment for 1.6×10^{15} cm^{-2} 2 keV As^{+} implant for 1050°C spike anneal after 950°C spike. Data from Jain [54].

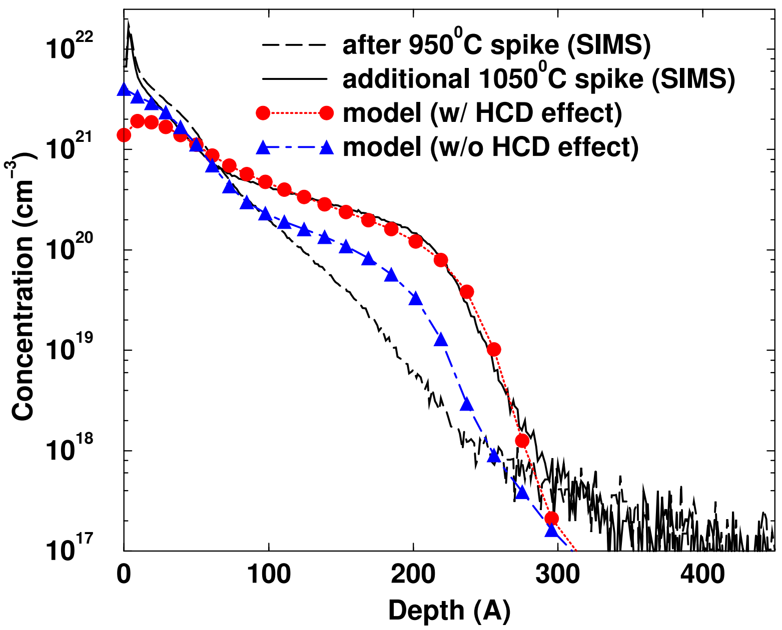

Figure 7.12: The illustration of importance of high concentration diffusion effect for shallow arsenic implant modeling. Comparison of simulation to experimental profile of 2×10^{15} cm^{-2} As implanted at 5 keV and annealed at 950°C and 1050°C. The dot-dashed curve (△) shows simulation results without the model for rapid diffusion via vacancies at high doping levels, which significantly underestimate profile depth as well as "plateau" concentration. Data from Jain [54]

7.5 Discussion

Here we would like to briefly outline the key elements of the model proposed in this chapter for simulation of low energy high dose As implants and discuss other possible phenomena which might be alternatives to the model proposed here.

- Grown-in Vacancies. Experiments show that during the post implant anneal As deactivates very rapidly but this deactivation does not significantly enhance diffusion. We assume that after SPE regrowth vacancies are grown-in as As_2V clusters according to Eq. 7.2. These vacancies provide sites for As deactivation and help eliminate interstitials ejected during deactivation and from EOR damage.

  As-I clusters formation is discussed in Section 7.3.1. Although formation of As_2I cluster is expected, both *ab-initio* calculations and experimental observations indicate that this structure does not play a primary role in As deactivation. The possible alternative or addition to proposed mechanism is the formation of small arsenic precipitates without vacancies or incorporating interstitials. In this case, arsenic peak would quickly deactivate via formation of small precipitates without interstitial ejection. The only experimentally observed arsenic precipitate in silicon is a monoclinic SiAs which is not a suitable candidate since its unit cell volume per atom is not smaller than the one of silicon diamond structure suggesting that no interstitials can be absorbed during monoclinic SiAs formation. At present there are no other experimentally identified Si/As aggregates. To date, search with *ab-initio* methods by our group and other groups has provided no candidate with sufficient binding energy.

- Rapid diffusion via vacancies at high doping levels. Experimental data analyzed in this chapter require higher As diffusivity in a peak region (for concentrations exceeding 2×10^{20} cm^{-3}) than the commonly accepted As diffusion coefficient [40, 73, 108] provides. The alternative to a high concentration addition to arsenic diffusivity proposed by Dunham and Wu [36] and represented by Eq. 7.1 may be a hypothesis that arsenic-vacancy clusters are mobile [87, 109]. This can help to account for the mobility of As above the level of electrical activation and may be used to simulate profile motion.

7.6 Summary

In this chapter, models needed for the simulation of shallow arsenic junction formation were presented. We reviewed enhanced vacancy mediated As diffusion at high doping levels, which account for the apparent mobility of clustered population. We also presented modified initial conditions, which require vacancy incorporation (interstitial sink) during epitaxial regrowth to match junction motion.

Chapter 8

CONCLUSIONS

This thesis has brought a better understanding of arsenic behavior at high concentrations. We presented physically-based models for arsenic electrical deactivation and diffusion, and successfully applied these models to a large set of experimental data. In this chapter, we review the major contributions of this work.

We have demonstrated that it is possible to model arsenic electrical deactivation and diffusion by considering the formation of immobile electrically inactive arsenic-vacancy clusters. An attractive potential between arsenic and vacancies exists due to the combination of strain compensation and valence. As a result, under most conditions, deactivation of arsenic occurs primarily via the formation of arsenic vacancy complexes. We concluded that equilibrium activation levels may be accurately modeled via As_2V, As_3V and As_4V cluster formation.

The barrier for Frenkel pair generation is greatly reduced by the strong binding of vacancies to the As clusters. *Ab-initio* results demonstrate that As_4V may be formed from an As_4Si complex by the ejection of a Si atom into the adjacent hexagonal interstitial site. The reverse reaction barrier is lower than the barrier for self-interstitial diffusion in silicon, and so the process can be considered diffusion limited. In heavily arsenic-doped material, As_4Si complexes are formed by random hopping via interstitial-mediated diffusion of arsenic. Our continuum model based on As_4V formation via interstitial ejection is able to describe both the very rapid initial deactivation of arsenic as well as the strongly superlinear dependence of interstitial supersaturation on doping level.

We applied the arsenic-vacancy clustering model to the simulation of ultra-shallow junctions formed by RTA after ultra-low energy ion implantation. Our analysis demonstrates that two effects are critical for the accurate prediction of As diffusion in silicon: rapid diffusion via vacancies at high arsenic doping levels, and vacancy incorporation during amorphous region recrystallization. The high concentration diffusion effect accounts for the apparent mobility of clustered population, and vacancy incorporation, which acts as an interstitial sink and effectively slows down diffusion, is essential for the simulation of the initial stages of annealing. The model provides very good agreement with both chemical profiles and electrical data.

An integral part of this work is the analysis of {311} defect formation, which accompanies deactivation and post-implant anneals. We have used MD simulations with empirical potentials to calculate the energy versus size and shape for interstitial aggregates, particularly {311} defects. Using the calculated energy versus size relationship, we compare the predicted {311} kinetics to experimental observations of {311} growth/dissolution. Our results indicate that the assumption about the transition between small self-interstitial clusters and {311}-type defects is important for the simulation of extended defects evolution.

A set of discrete clusters is used to model interstitial cluster evolution after ion implantation in Si. Two independent populations of self-interstitial clusters have been considered: {311} defects and compact clusters. The system is able to model time and temperature dependence of interstitial supersaturation as well as the size distribution during post-implant anneal. A procedure has been proposed to reduce this complex model into a simple two-moment model. The parameters for this two moment model are derived from the full rate equation model and are found to give a good match to data. This computationally efficient two-moment model has been applied to the calculation of "+N" factors.

8.0.1 Recommendations for the Future Work

Many questions regarding As in Si still remain to be answered. In this section, we would like to discuss what modeling efforts or experiments need to be done to futher enhance our knowledge of arsenic behavior in silicon.

One of the critical parameters used in our simulations is the energy level of a negatively charged interstitial, K_I^-. The commonly used value has been reported by Giles [45]. He used oxidation-enhanced diffusivity experiments under extrinsic conditions at 1000°C. It is a widely used assumption that the acceptor state (I^-) tracks the conduction band as the silicon band gap changes with temperature; however, no theoretical proof of this exists. Arsenic deactivation experiments modeled in this work were performed at 750°C and even a small error in the location of the defect level in the band gap might result in a large error in diffusion capacity at low temperature. The modeling efforts of our laboratory regarding negative interstitial level in silicon at low temperature (see Table A.1) contradict the value reported by Giles. A larger value of K_I^- increases the diffusion capacity of interstitials and therefore decreases the I-cluster dissolution time. The value of K_I^- can be verified experimentally: one may consider the measurement the diffusion enhancement of an interstitial type dopant (e.g. P, As, B) in an n-type well (e.g P, As) under the TED conditions. Since boron is known to form acceptor-donor pairs with both As and P, the study of TED of As in a P well (or P in an As well) should be appropriate to determine the value of K_I^-.

Arsenic shows a strong dose loss behavior. It segregates to the thin interface layer between Si and SiO_2, diffuses through the silicon dioxide and evaporates into the environment. If no protective oxide is used, the dose loss for the shallow implant may be very severe (e.g for $1 \times 10^{15}\,\mathrm{cm}^{-2}$ As^+ implanted at 1 keV into bare silicon and spike-annealed at 1050°C, loss is about 70% of the initial dose). Therefore modeling of the dose loss is an essential part of the arsenic diffusion simulation. The finite capacity model which was used in this work gives acceptable results but does not show the strong dose loss rebound observed in some experiments [59] and also is not suitable for the simulation of annealing of arsenic implanted into bare silicon. More work needs to be done to build an accurate physically-based dose loss model.

One of the key mechanisms proposed in this work is the formation of a vacancy-rich layer after SPE in the presence of high arsenic concentration. However it is hard to verify this conclusion experimentally. One of the reasons is that amorphizing implant introduces interstitial-type EOR damage, and during the anneal a significant interstitial supersaturation is present, making any attempt to measure vacancy supersaturation (e.g. Sb marker layer is sensitive to vacancy supersaturation) impractical. On the other hand, an alternative method is to use molecular dynamics simulations to study the regrowth of an amorphous layer and verify the presence of retained vacancies in the highly arsenic doped silicon substrate. At present no accurate interaction potential exists for arsenic in silicon. To ensure the accuracy of the potential, one needs to match the energies of several key structures (i.e. As-V pair, As_nV complexes), the diffusion barrier for As in Si, and the diffusion barrier for vacancies in the presence of arsenic. First-principle calculations can help to determine these key structures and corresponding energies.

Several elements are known to have a strong binding with a vacancy (N, F, Au). Fluorine and gold are also fast diffusers in silicon and therefore may be used at low temperatures. Gold has been successfully used for vacancy and void "labeling" in silicon, one gold atom decorates one vacancy in silicon. It might be possible to measure experimentally F or Au redistribution during a low temperature anneal after amorphous region regrowth to determine the presence of vacancy rich regions after the amorphous/crystalline regrowth.

BIBLIOGRAPHY

[1] "The international technology roadmap for semiconductors". International SEMATECH (1999).

[2] J. L. Allain, J. R. Regnard, A. Bourret, A. Parisini, A. Armigliato, G. Tourillon, and S. Pizzini. "Extended x-ray absorption fine-structure study of the local atomic structure in As heavily implanted silicon". *Phys. Rev. B* **46**(15), 9434 (1992).

[3] M.P. Allen and D.J. Tildesley. *Computer simulation of liquids*. Oxford University Press (1987).

[4] R. Angelucci, G. Celotti, D. Nobili, and S. Solmi. "Precipitation and diffusivity of arsenic in silicon". *J. Electrochem. Soc.* **132**(11), 2726 (1985).

[5] R. Angelucci, F. Cembali, P. Negrini, M. Servidori, and S. Solmi. "Temperature and time dependence of dopant enhanced diffusion in self ion implanted silicon". *J. Electrochem. Soc.* **134**(12), 3130 (1987).

[6] N. Arai and S. Takeda. "Self-interstitial clustering in crystalline silicon". *Phys. Rev. Lett.* **78**(22), 4265 (1997).

[7] A. Armigliato, D. Nobili, , and S. Solmi. "Electron microscopy of As supersaturated silicon". *J. Electrochem. Soc.* **133**(12), 2560 (1986).

[8] A. Armigliato and A. Parisini. "Electron microscopy characterization of monoclinic SiAs precipitates in heavily As^+ -implanted silicon". *J. Mater. Res.* **6**(8), 1701 (1991).

[9] G.P. Barbuscia, G. Chin, R.W. Dutton, T. Alvarez, and L. Arledge. "Modeling of polysilicon dopant diffusion for dhallow-junction bipolar technology". In **Interna-**

tional Electron Devices Meeting. Technical Digest. IEEE, New York, NY, USA, IEEE, 757–760 (1984).

[10] M. Z. Bazant and E. Kaxiras. "Modeling of covalent bonding in solids by inversion of cohesive energy curves". *Phys. Rev. Lett.* **77**(21), 4370 (1996).

[11] M. Z. Bazant, E. Kaxiras, and J. F. Justo. "Enviroment dependent interatomic potential for bulk silicon". *Phys. Rev. B* **56**(14), 8542 (1997).

[12] M. Berding and A. Sher. "Electronic quasichemical formalism: Application to arsenic deactivation in silicon". *Phys. Rev. B* **58**(7), 3853 (1998).

[13] M. Berding, A. Sher, M. van Schilfgaarde, P. M. Rousseau, and W.E. Spicer. "Deactivation in heavily arsenic-doped silicon". *Appl. Phys. Lett.* **72**(12), 1492 (1998).

[14] J.P. Biersack and W. Ecstein. "Sputtering studies with the Monte Carlo program TRIM.SP". *Appl. Phys. A* **34**, 73 (1984).

[15] A. Bongiorno, L. Comombo, F. Cargoni, C. Gatti, and M. Rosati. "Silicon self-interstitial clusters". In **Multiscale Modeling of Materials Mater. Res. Soc. Symp. Proc.**, Materials Research Soc., 413 (1999).

[16] H. Bracht, N.A. Stolwijk, and H. Mehrer. "Equilibrium concentrations of intrinsic point defects in silicon determined by zinc diffusion". In **Proc. Silicon Material Science and Technology**, 593 (1994).

[17] H. Bracht, N. A. Stolwijk, and H. Mehrer. "Properties of intrinsic point defects in silicon determined by zinc diffusion experiments under nonequilibrium conditions". *Phys. Rev. B* **52**(23), 16542 (1995).

[18] R. Brindos, P. Keys, K. Jones, and M. Law. "Effect of arsenic doping on {311} defect dissolution in silicon". *Appl. Phys. Lett.* **75**(2), 229 (1999).

[19] M. M. Bunea, P. Fastenko, and S. T. Dunham. "Atomistic simulations of damage evolution in silicon". In **Si Front-End Processing—Physics and Technology of Dopant-Defect Interactions (Mat. Res. Soc. Proc. 568, Pittsburgh, PA, 1999)**, Materials Research Soc., 135–140 (1999).

[20] M.-J. Caturla, T. Diaz de la Rubia, L. A. Marques, and G.H. Gilmer. "Ion beam processing of silicon at kev energies: a molecular dynamics study". *Phys. Rev. B* **54**(23), 16683 (1996).

[21] S. Chakravarthi. "Physics and modeling of ion implantation induced transient deactivation and diffusion processes in boron doped silicon". Ph.D. thesis, Boston University (2001).

[22] S. Chakravarthi and S.T. Dunham. "Point defect properties from metal diffusion experiments— what does the data really tell us?". In **Defects and Diffusion in Silicon Processing**, Materials Research Soc., 47 (1997).

[23] S. Chakravarthi and S. T. Dunham. "Modeling of vacancy cluster formation in ion implanted silicon". *J. Appl. Phys.* **89**(9), 4758 (2001).

[24] J. W. Christian. *The theory of transformations in metals and alloys*. Pergamon, Oxford (1975). 2nd ed.

[25] I. Clejan and S.T. Dunham. "A reduced moment based model for precipitaion kinetics and application to dopant deactivation in silicon". *J. Appl. Phys.* **78**(12), 7327 (1995).

[26] N.E.B. Cowern, K.T.F. Janssen, and H.F.F. Jos. "Transient diffusion of ion implanted B in Si: Dose, time and matrix dependence of atomic and electrical profiles". *J. Appl. Phys.* **68**(12), 6191 (1990).

[27] N.E.B. Cowern, G. Mannino, P.A. Stolk, F. Roozeboom, J.G.M. van Berkum, F. Cristiano, A. Claverie, and M. Jaraiz. "Energetics of self-interstitial clusters in Si". *Phys. Rev. Lett.* **82**(22), 4460 (1999).

[28] N.E.B. Cowern, G.F.A. van de Walle, P.C. Zalm, and D.W.E. Vandenhoudt. "Mechanisms of implant damage annealing and transient enhanced diffusion in Si". *Appl. Phys. Lett.* **65**(23), 2981 (1994).

[29] M. Derdour, D. Nobili, and S. Solmi. "High-temperature equilibrium carrier density of arsenic-doped silicon". *J. Electrochem. Soc.* **129**(8), 1826 (1991).

[30] O. Dokumaci. "Analysis and modeling of arsenic activation and deactivation in silicon". Ph.D. thesis, University of Florida (1997).

[31] O. Dokumaci, P. Rousseau, S. Luning, V. Krishnamoorthy, K. S. Jones, and M. E. Law. "Transmission electron microscopy analysis of heavily As-doped, laser, and thermally annealed layers in silicon". *J. Appl. Phys.* **78**(2), 828 (1995).

[32] S.T. Dunham. "Modeling of the kinetics of dopant precipitation in silicon". *J. Electrochem. Soc.* **142**, 2823 (1995).

[33] S.T. Dunham, I. Clejan, and A. H. Gencer. "Accurate and efficient modeling of nucleation and growth processes". *Mat. Sci. Eng. A* **238**, 152 (1997).

[34] S.T. Dunham, A.H. Gencer, and S. Chakravarthi. "Modeling of dopant diffusion in silicon". *IEICE Trans. Electron.* **E82C**(6), 800 (1999).

[35] S. T. Dunham, P. Fastenko, Z. Qin, and G. Henkelman. "Atomistic modeling of arsenic diffusion and activation". In **Proceedings of 2001 International Conference on Computational Nanoscience (ICCN 2001), (Computational Publications, Cambridge, MA)**, (2001).

[36] S. T. Dunham and C. D. Wu. "Atomistic models of vacancy-mediated dopant diffusion in silicon". *J. Appl. Phys.* **78**(4), 2362 (1995).

[37] D. J. Eaglesham, P. A. Stolk, H. J. Gossmann, and J.M. Poate. "Implantation and transient B diffusion in Si: The source of the interstitials". *Appl. Phys. Lett.* **65**(18), 2305 (1994).

[38] A. Erbil, W. Weber, G. S. Cargill III, and R. F. Boehme. "Lattice distortions for arsenic in single-crystal silicon". *Phys. Rev. B* **34**(2), 1392 (1986).

[39] P. Fahey, P. B. Griffin, and J. D. Plummer. "Point defects and dopant diffusion in silicon". *Rev. Mod. Phys.* **61**, 289 (1989).

[40] R. B. Fair. *Impurity Doping Processes in Silicon.* North-Holland, New York (1981). F. Y. Yang, ed. p.315.

[41] R. B. Fair and G. R. Weber. "Effects of complex formation on diffusion of arsenic in silicon". *J. Appl. Phys.* **44**(1), 273 (1973).

[42] A.H. Gencer. *DOPDEES User's Manual* , http://eng.bu.edu/ alp/dopdees/, (1996).

[43] A.H. Gencer and S.T. Dunham. "A predictive model for transient enhanced diffusion based on evolution of {311} defects". *J. Appl. Phys.* **81**(2), 631 (1997).

[44] A. H. Gencer. "Modeling and simulation of transient enhanced diffusion based on interactions of point and extended defects". Ph.D. thesis, Boston University (1999).

[45] M.D. Giles. "Defect-coupled diffusion at high concentrations". *IEEE transactions on computer-aided design* **8**(5), 460 (1989).

[46] J. Goetzlich. "Clustering kinetics of arsenic and phosphorous in laser annealed silicon". In **Ion Beam Processes in Advanced Electronic Material and Device Technology, Mater. Res. Soc, Symp. Proc., vol 45 (Materials Research Society, Pittsburgh, PA, 1985**, Materials Research Soc., 349 (1985).

[47] H.-J. Gossmann, T. E. Haynes, P. A. Stolk, D. C. Jacobson, G. H. Gilmer, J. M. Poate, H. S. Luftman, T. K. Mogi, and M. O. Thompson. "The interstitial fraction of diffusivity of common dopants in Si". *Appl. Phys. Lett.* **71**(26), 3862 (1997).

[48] J.J. Grob, S. Unamuno, A. Grob, M. Ajaka, A. Slaoui, and R. Stuck. "Activation and diffusion during rapid thermal annealing of arsenic and boron implanted silicon". *Nuc. Inst. and Meth. B* B**19-20**(8), 501 (1987).

[49] E. Guerrero, H. Potzl, R. Tielert, M. Grasserbauer, and G. Stingeder. "Generalized model for the clustering of As dopants in Si". *J. Electrochem. Soc.* **129**(8), 1826 (1982).

[50] G. Henkelman, B.P. Uberuaga, and H. Jónsson. "A climbing image nudged elastic band method for finding saddle points and minimum energy paths". *J. Chem. Phys.* **113**(22), 9901 (2000).

[51] A. Herrera-Gomez, P.M. Rousseau, G. Materlik, T. Kendelewicz, J.C. Woicik, P.B. Griffin, J. Plummer, and W.S. Spicer. "Evolution of crystallographic position of as impurities in heavily doped si crystals as their electrical activity changes". *Appl. Phys. Lett.* **68**(22), 3090 (1996).

[52] A. Herrera-Gomez, P.M. Rousseau, J.C. Woicik, T. Kendelewicz, J. Plummer, and W.S. Spicer. "Lattice compression of Si crystals and crystallographic position of As impurities measured with x-ray standing wave spectroscopy". *J. Appl. Phys.* **85**(3), 1429 (1999).

[53] J.L. Hoyt and J.F. Gibbons. "Rapid thermal annealing of As in Si". In **Rapid Thermal Processing. Mater. Res. Soc, Pittsburgh, PA, USA**, Materials Research Soc., 15 (1986).

[54] A. Jain. SIMS and resistivity data from Texas Instruments.

[55] M. Jaraiz, G. H. Gilmer, J. M. Poate, and T. D. de la Rubia. "Atomistic calculations of ion implantation in si: Point defect and transient enhanced diffusion phenomena". *Appl. Phys. Lett.* **68**(3), 409 (1996).

[56] K. S. Jones, D. Downey, H. Miller, J. Chow, J. Chen, M. Puga-Lambers, K. Moller, M. Wright, E. Heitman, J. Glassberg, M. Law, Robertson, and R. Brindos. "Transient enhanced diffusion in low energy arsenic implanted silicon". In **1998 International Conference on Ion Implantation Technology. Proceedings IEEE, Piscataway, NJ, USA**, IEEE, 841 (1998).

[57] H. Jónsson, G. Mills, and K.W. Jacobsen. *Classical and Quantum Dynamics in Condensed Phase Simulations*. World Scientific (1998). ed. B. J. Berne, G. Ciccotti, and D. F. Coker, page 385.

[58] J. F. Justo, M. Z. Bazant, E. Kaxiras, V. V. Bulatov, and S. Yip. "Interatomic potential for silicon defectsand disodered phases". *Phys. Rev. B* **58**(5), 2539 (1998).

[59] R. Kasnavi, P. Griffin, and J. Plummer. "Dynamics of arsenic dose loss at sio_2 interface during ted". In **Proc. SISPAD**, IEEE, 48 (1998).

[60] J. Kim, F. Kirchhoff, J.W. Wilkims, and F.S. Khan. "Stability of Si-interstitial defects: From point to extended defects". *Phys. Rev. Lett.* **84**(3), 503 (2000).

[61] J. Kim, J.W. Wilkims, F.S. Khan, , and A. Canning. "Extended Si {311} defects". *Phys. Rev. B* **55**(24), 16186 (1997).

[62] R. Kim, T. Aoki, Y. Furuta, H. Kobyashi, J. Xia, T. Saito, Y. Kamakura, and K. Taniguchi. "Transient enhanced diffusion of arsenic by self-implantation: The role of As-I clusters". In **presented at the 2000 MRS Spring Meeting, San Francisco, CA, April 2000**, Materials Research Soc., (2000).

[63] M. Kohyama and S. Takeda. "Atomic structure and energy of the {113} planar interstitial defects in Si". *Phys. Rev. B* **46**(19), 12305 (1992).

[64] G. Kresse and J. Furthmüller. "Efficiency of ab-initio total energy calculations for metals and semiconductors using a plane-wave basis set". *Comput. Mater. Sci.* **6**(1), 15 (1996).

[65] G. Kresse and J. Furthmüller. "Efficient iterative schemes for ab-initio total-energy calculations using a plane-wave basis set". *Phys. Rev. B* **54**(16), 11169 (1996).

[66] G. Kresse and J. Hafner. "Ab-initio molecular dynamics for liquid metals". *Phys. Rev. B* **47**(1), 558 (1993).

[67] G. Kresse and J. Hafner. "Ab-initio molecular-dynamics simulation of the liquid-metal-amorphous-semiconductor transition in germanium". *Phys. Rev. B* **49**(20), 14251 (1994).

[68] V. Krishnamoorthy, A. Moller, K.S. Jones, D. Venables, J. Jackson, and L. Rubin. "Transient enhanced diffusion and defect microstructure in high dose, low energy As+ implanted Si". *J. Appl. Phys.* **84**(11), 5997 (1998).

[69] A. Nylandsted Larsen, K. Killesbeck Larsen, P. E. Andersen, and B. G. Svennson. "Heavy doping effects in the diffusion of group IV and V impurities in silicon". *J. Appl. Phys.* **73**(2), 691 (1993).

[70] D.W. Lawther, U. Myler, P.J. Simpson, P.M. Rousseau, P.B. Griffin, W. T. Fang, and J. D. Plummer. "Vacancy generation resulting from electrical deactivation of arsenic". *Appl. Phys. Lett.* **67**(24), 3575 (1995).

[71] A. Lietoila, J. F. Gibbons, T. J. Magee, J. Peng, and J. D. Hong. "Solid solubility of As in Si as determined by ion implantation and CW laser annealing". *Appl. Phys. Lett.* **35**(7), 532 (1979).

[72] S. Luning. "Kinetics of high concentration arsenic deactivation". Ph.D. thesis, Stanford University (1996).

[73] B. J. Masters and J. M. Fairfield. "Arsenic isoconcentration diffusion studies in silicon". *J. Appl. Phys.* **40**(6), 2390 (1969).

[74] D. Mathiot and J. C. Pfister. "Influence of the nonequilibrium vacancies on the diffusion of phosphorus into silicon". *J. Appl. Phys.* **53**, 3035 (1982).

[75] D. Mathiot and J. C. Pfister. "Dopant diffusion in silicon: A consistent view involving nonequilibrium defects". *J. Appl. Phys.* **55**(10), 3518 (1984).

[76] D. Nobili, A. Carabelas, G. Celotti, and S. Solmi. "Precipitation as the phenomenon responsible for the electrically inactive arsenic in silicon". *J. Electrochem. Soc.* **130**(4), 922 (1983).

[77] D. Nobili, S. Solmi, A. Parisini, M. Derdour, A. Armigliato, and L. Moro. "Precipitation, aggregation, and diffusion in heavily arsenic-doped silicon". *Phys. Rev. B* **49**(4), 2477 (1994).

[78] B. Obradovic, G. Wang, C. Snell, G. Balamurugan, M.F. Morris, Y. Chen, and A.F. Tasch. *UT-Marlowe Version 4.1 User's Manual* (1998).

[79] R.W. Olesinky and G.J. Abaschian. "Arsenic-silicon". *Bull. Alloy Phase Diagrams* **6**, 254 (1985).

[80] M. Orlowski, R. Subrahmanyan, and G. Huffman. "The effect of low-thermal-budget anneals and furnace ramps on the electrical activation of arsenic". *J. Appl. Phys.* **71**(1), 164 (1992).

[81] C.J. Ortiz and D. Mathiot. "A new kinetic model for the nucleation and growth of self-interstitial". In **MRS 2001 Spring Conference Proceedings, to be published**, Materials Research Soc., (2001).

[82] G. L. Ouwerling. *Profile, The General Purpose Data Processor* (1999). Electrical Materials Laboratory, Delft University.

[83] P.A. Packan. "Physical modeling of transient diffusion effects in silicon due to surface oxidation and ion-implantation". Ph.D. thesis, Stanford University (1991).

[84] K. C. Pandey, A. Erbil, G.S. Cargill, R. F. Boehme, and D. Vanderbilt. "Annealing of heavily arsenic-doped silicon: electrical deactivation and new defect complex". *Phys. Rev. Lett.* **61**(11), 1282 (1988).

[85] A. Parisini, A. Bourret, A. Armigliato, M. Servidori, S. Solmi, R. Fabbri, J. R. Regnard, and J. L. Allain. "Electrical activity and structural evolution correlations in laser and thermally annealed As-implanted Si specimens". *J. Appl. Phys.* **67**(5), 2320 (1990).

[86] J.P. Perdew. *Electronic Structure of Solids*. Akademie Verlag, Berlin (1991). Editors P. Ziesche and H. Eschrig.

[87] M. Ramamoorthy and S. Pantelides. "Complex dynamical phenomena in heavily arsenic doped silicon". *Phys. Rev. Lett.* **75**(25), 4753 (1996).

[88] D.C. Rapaport. *The Art of Molecular Dynamics Simulation*. Cambridge University Press (1995).

[89] P. Rousseau. "Activation and deactivation of arsenic in silicon". Ph.D. thesis, Stanford University (1996).

[90] P.M. Rousseau, P.B. Griffin, W. T. Fang, and J. D. Plummer. "Arsenic deactivation enhanced diffusion: A time, temperature, and concentration study". *J. Appl. Phys.* **84**(7), 3593 (1998).

[91] P.M. Rousseau, P.B. Griffin, S. Luning, and J. D. Plummer. "A model for mobility degradation in highly doped arsenic layers". *IEEE Trans. Electron Devices* **43**(11), 2025 (1996).

[92] A. H. Gencer S. T. Dunham and S. Chakravarthi. "Modeling of dopant diffusion in silicon". *Trans. Electron.* **82**(6), 800 (1999).

[93] K. Saarinen, J. Nissila, H. Kauppinen, M. Hakala, M.J. Pulska, P. Hautojarvi, and C. Corbel. "Indication of vacancy-impurity complexes in highly n-type Si". *Phys. Rev. Lett.* **82**(9), 1883 (1999).

[94] B.W. Schueler and D.F. Reich. "Sims depth profiling: a review of capabilities and challenges". In **in Ultra Shallow Junctions Proc., Napa, CA, 2001**, 111–119 (2001).

[95] H. Shibayama, H. Masaki, H. Ishikawa, and H. Hashimoto. "Emitter dip effect by low temperature heat-treatment of arsenic-diffused layer". *J. Electrochem. Soc.* **123**(5), 742 (1976).

[96] S. Solmi and D. Nobili. "High concentration diffusivity and clustering of arsenic and phosphorus in silicon". *J. Appl. Phys.* **83**(5), 2484 (1998).

[97] S. Solmi, D. Nobili, and J. Shao. "Reverse annealing, clustering, and electron mobility in arsenic doped silicon". *J. Appl. Phys.* **87**(2), 658 (2000).

[98] F. H. Stillinger and T. A. Weber. "Computer simulation of local order in condensed phases of silicon". *Phys. Rev. B* **31**(8), 5262 (1985).

[99] R. Subrahmanyan, M. Orlowski, and A. R. Sitaram. "Confirmation of a vacancy role in the electrical activation and deactivation of arsenic using a point-defect injection experiment". In **Process Physics and Modeling in Semiconductor Technology, Electrocemical Society Proceedings**, Electrochemical Soc., 120 (1993).

[100] S. Takeda. "An atomic model of electron-irradiation-induced defects on (113) in Si". *Japanese J. Appl. Phys.* **30**(4), 369 (1991).

[101] M. Tang, L. Colombo, J. Zhu, and T. Diaz de la Rubia. "Intrinsic point defects in crystalline silicon: tight-binding molecular dynamics studies of self-diffusion, interstitial-vacancy recombination, and formation volumes". *Phys. Rev. B* **55**(21), 14279 (1997).

[102] M. Y. Tsai, F. F. Morehead, E. E. Baglin, and A. E. Michel. "Shallow junctions by high-dose as implants in Si: experiments and modeling". *J. Appl. Phys.* **51**(6), 3230 (1980).

[103] A. Ural, P.B. Griffin, and J.D. Plummer. "Fractional contributions of microscopic diffusion mechanisms for common dopants and self-diffusion in silicon". *J. Appl. Phys.* **85**(9), 6440 (1999).

[104] A. Ural, P.B. Griffin, and J.D. Plummer. "Self-diffusion in silicon: Similarity between the properties of native point ddefects". *Phys. Rev. Lett.* **83**(17), 3454 (1999).

[105] O. Vancauwenberghe, N. Herbots, and O. Hellman. "A quantitative model of point defect diffusivity and recombination in ion beam deposition and combined ion and molecular deposition". *J. Vac. Sci. Tech. B* **9**, 2027 (1991).

[106] D. Vanderbilt. "Soft self-consistent pseudopotentials in a generalized eigenvalue formalism". *Phys. Rev. B* **41**(11), 7892 (1990).

[107] T. Wadsten. "The crystal structure of SiAs". *Acta Chem. Scand.* **19**(5), 1232 (1965).

[108] F. Wittel. "Development and characterization of process simulation models for diffusion and co-diffusion of dopants in silicon". Ph.D. thesis, Boston University (1996).

[109] J. Xie and S.P. Chen. "Diffusion and clustering in heavily arsenic-doped silicon: discrepancies and explanation". *Phys. Rev. Lett.* **83**(9), 1795 (1999).

[110] J. Xie and S.P. Chen. "Generation of frenkel defects in heavily arsenic doped silicon: A first-principles study". *J. Appl. Phys.* **87**(9), 4160 (2000).

Appendix A

PARAMETERS FOR ARSENIC ACTIVATION/DEACTIVATION MODEL EQUATIONS

Parameters used in the simulations are listed in the Table A.1.

Table A.1: Parameters used in the simulation. The model is presented in Chapter 6.

Parameter	Exponential pre-factor	Activation Energy
$K_{\mathrm{As^{++}/Si}}$	$6/C_{\mathrm{Si}}$	0
$K_{\mathrm{As^{3+}/Si}}$	$4/(C_{\mathrm{Si}})^2$	0
$K_{\mathrm{As^{4+}/Si}}$	$1/(C_{\mathrm{Si}})^3$	0
$K_{\mathrm{As^{+}/V^{0}}}$	$1/C_{\mathrm{Si}}$	1.1
$K_{\mathrm{As_2V}}$	$1/C_{\mathrm{Si}}$	1.15
$K_{\mathrm{As_3V}}$	1	-0.66
$K_{\mathrm{As_4V}}$	$\exp(-16.57)$	1.06
$K_{\mathrm{K_I^-}}$	5.08819e-05	-0.83

VITA

EDUCATION:

- **University of Washington**, Seattle, WA

  PhD in Electrical Engineering, 2002

  Dissertation: Modeling and simulation of arsenic activation and diffusion in silicon.

- **Worcester Polytechnic Institute**, Worcester, MA

  MS in Electrical Engineering, October 1997

- **Moscow Engineering Physics Institute**, Moscow, Russia

  Diploma in Engineering/Physics, December 1995

  Thesis: UV-stimulated cleaning and modification of silicon surface in fluorine containing ambiance at room temperature, controlled by in-situ XPS analysis.

WORK EXPERIENCE:

- **University of Washington**, October 1999 - December 2001,

  Research Assistant for Prof. Scott Dunham in Electrical Engineering Department

- **Boston University**, March 1998 - September 1999,

  Research Assistant for Prof. Scott Dunham in Electrical and Computer Engineering Department.

- **IBM Corporation**, East Fishkill, NY, July 1999 - September 1999

  Summer intern, Division: TCAD, SRDC

- **Worcester Polytechnic Institute**, January 1996 - May 1997

  Research Assistant, Electromagnetic CAD Laboratory